Fermilab

FERMILAB-THESIS-1999-09

SEARCH FOR SUPERSYMMETRY USING LIKE-SIGN DILEPTON EVENTS AT CDF

A Dissertation

by

JAMES PAUL DONE

Submitted to the Office of Graduate Studies of
Texas A&M University
in partial fulfillment of the requirements for the degree of

DOCTOR OF PHILOSOPHY

August 1999

Major Subject: Physics

SEARCH FOR SUPERSYMMETRY

USING LIKE-SIGN DILEPTON EVENTS AT CDF

A Dissertation

by

JAMES PAUL DONE

Submitted to Texas A&M University
in partial fulfillment of the requirements
for the degree of

DOCTOR OF PHILOSOPHY

Approved as to style and content by:

Teruki Kamon
(Chair of Committee)

Robert C. Webb, Sr.
(Member)

James T. White
(Member)

Philip B. Yasskin
(Member)

Thomas W. Adair, III
(Head of Department)

August 1999

Major Subject: Physics

ABSTRACT

Search for Supersymmetry
Using Like-Sign Dilepton Events at CDF. (August 1999)
James Paul Done, B.S., Roosevelt University;
M.S., University of California, Davis
Chair of Advisory Committee: Dr. Teruki Kamon

Supersymmetric gluons (gluinos, $\tilde{g}$) and supersymmetric quarks (squarks, $\tilde{q}$) will be pair-produced in $p\overline{p}$ collisions at $\sqrt{s}$= 1.8 TeV at the Fermilab Tevatron if kinematically accessible. Gluinos and squarks can decay via charginos and neutralinos to final states containing two or more leptons. Since the gluino is a Majorana particle, a large fraction of like-sign dilepton events will be observed. This property effectively reduces the Standard Model processes which largely yield opposite-sign dilepton events. Thus, the strategy of this analysis is to search for an excess of events containing two isolated leptons with same-sign charge, missing energy, and jets. Based on 106 pb^{-1} of data, we observe zero events and have set a 95 % confidence level limit for the gluino mass.

To my mother and the memory of my father, a scientist and a baseball fan.

ACKNOWLEDGMENTS

I wish to acknowledge Teruki Kamon, Maxwell Chertok, and Stephan Lammel as co-authors in this analysis. I would also like to mention Ping Yeh for his expertise in UNIX and his knowledge of the data production process; I thank Jay Dittmann and Andrew Gordon for their knowledge of electron identification; I thank Greg Feild, Todd Huffman, Jonathan Lewis, Paul Ngan, Jim Olsen, Steven Pappas, Kevin Pitts, and George Michail (who passed away in 1996) for their assistance in muon identification and triggers; I thank Wendy Taylor for calculating the level 2 low E_{T} electron trigger efficiency; thanks to Nicki Bruner for determining the level 3 trigger efficiencies; I also thank Farhad Keyvan for his advice and PAW expertise. I thank Andrew Scott for determining the Drell-Yan cross-section using my SUSY Dilepton sample; I also take the time to acknowledge John Conway, Regina Demina, Henry Frisch, Mike Gold, Armin Kongeter, Kaori Maeshima, Simona Murgia, Carmine Pagliarone, Maria Spiropulu, David Stuart, Federica Strumia, Rocio Vilar, and Steven Worm who have given this analysis constructive criticism and support.

I thank Fermi National Accelerator Laboratory and the technical staffs of the participating institutions for their vital contributions. This work was supported by the U. S. Department of Energy and National Science Foundation; the Italian Istituto Nasionale di Fisica Nucleare; the Ministry of Education, Science and Culture of Japan; the Natural Sciences and Engineering Research Council of Canada; the National Science Council of the Republic of China; the A. P. Sloan Foundation; and the Swiss National Science Foundation. I was supported by the U. S. DOE under Contract No. DE-FG05-95ER40917.

TABLE OF CONTENTS

CHAPTER Page

CHAPTER Page

CHAPTER Page

LIST OF TABLES

TABLE Page

TABLE Page

TABLE Page

TABLE Page

TABLE Page

LIST OF FIGURES

FIGURE Page

FIGURE Page

FIGURE Page

FIGURE Page

FIGURE Page

FIGURE Page

CHAPTER I

INTRODUCTION

It has always been the goal of human beings to describe the Universe and its Creation using belief and/or the power of reason. The latter is the motivation of this dissertation. Using reason and experiment, the human consciousness has developed the Standard Model which defines the total understanding of the constituents of matter and the forces of nature.

The Universe is composed of matter and the forces that mediate their interactions. Matter consists of quarks and leptons, which are spin-1/2 particles obeying Fermi-Dirac statistics (fermions). The forces that control the interactions between fermions are carried by particles with integral spin obeying Bose-Einstein statistics (bosons). Empirical studies have shown that there are four types of forces in nature: strong nuclear, electromagnetic, weak nuclear, and gravity. The current theory is the so-called Standard Model (SM) of fundamental particles and interactions which unifies strong nuclear, electromagnetic, and weak nuclear forces.

Leptons are particles which are affected by electromagnetism, gravitation, and the weak nuclear force. Leptons carry electric charges, $\pm \mid e \mid$, and the three types of each are known: electron (e), muon (μ), and tau (τ). Neutral leptons are called neutrinos and have small or no rest mass. Experiments have shown that each lepton is assigned a conserved lepton number (L_e, L_μ, L_τ). Antileptons have opposite charge and lepton number to those leptons. Thanks to the symmetry associated with the weak nuclear force, left-handed charged leptons and neutrinos are organized in 3

The journal model is *Physical Review D*.

generations of doublets:

$$\begin{pmatrix} \nu_e \\ e \end{pmatrix}_L \begin{pmatrix} \nu_\mu \\ \mu \end{pmatrix}_L \begin{pmatrix} \nu_\tau \\ \tau \end{pmatrix}_L$$

The right-handed leptons are represented as singlets:

$$e_R,\ \mu_R,\ \tau_R$$

Quarks are classified under six *flavors* : up, down, charm, strange, top, and bottom. One group of quarks has electric charge $\frac{2}{3}e$ (up, charm, and top) and the other group has electric charge $-\frac{1}{3}e$ (down, strange, and bottom). Quarks have an additional quantum number called *color* of which there are three types: red (R), blue (B), and green (G). Again, the symmetry of the weak nuclear force organizes left-handed quarks (q_L) in 3 generations of doublets :

$$\begin{pmatrix} u \\ d \end{pmatrix}_L \begin{pmatrix} c \\ s \end{pmatrix}_L \begin{pmatrix} t \\ b \end{pmatrix}_L$$

whereas the right-handed quarks (q_R) are singlets :

$$u_R,\ d_R,\ c_R,\ s_R,\ t_R,\ b_R$$

A particle consisting of two quarks ($q\bar{q}$) is classified as a *meson*. A cluster of three quarks (qqq) creates a *baryon*. These quarks combine such that their configuration is colorless. The protons and neutrons that create the nuclei of all atoms are baryons. Since proton decay has not been observed, the number of baryons (B) in a particle interaction is conserved. Each quark is assigned a baryon number of $\frac{1}{3}$.

There are four forces which govern matter in the Universe : (1) gravitation, (2)

electromagnetism, (3) the strong nuclear force, and (4) the weak nuclear force. The forces that govern the interactions of matter are mediated by bosons (see Table I).

TABLE I. A description of bosons which mediate the four forces.

Name	Symbol	Force Mediated	Mass (GeV/c^2)
photon	γ	Electromagnetism	0
weak bosons	$W^{\pm}$, Z^0	Weak Nuclear Force	80, 91
gluon	g	Strong Nuclear Force	0
graviton	G	Gravitation	0

Gravitation is one of the oldest known forces. It affects particles over a wide range of distances. The Einstein field equations indicate that it is transmitted by a massless spin-2 bosons called the graviton. Although gravity is a strong force outside atomic distances, it goes unnoticed in the subatomic world due to much stronger forces that lie within.

It was known since the days of James Clerk Maxwell that electricity and magnetism were different facets of the same force, light or electromagnetism. In the earliest days of quantum theory, it was known that light is quantized in photons. The quantized theory of electromagnetism is called *quantum electrodynamics* (QED). QED states that any two charged particles interact via the interchange of a photon. Hence, the photon is the carrier of the electromagnetic force.

The weak nuclear force was not first seen until nuclear phenomena were studied. The weak nuclear force acts only in short distances — distances smaller or on the order of 1 fermi (10^{-15} m). In these distances, it is powerful enough to be responsible for nuclear interactions such as β-decay through the exchange of W-boson and neutrino scattering through the exchange of a Z-boson. It only affects particles whose helicity is left-handed.

The strong nuclear force is responsible for binding of nuclei and is only measured

within the nuclear realm. This force is, of course, much stronger than the other forces or you would not be reading this dissertation. The strong force is carried by a spin-1 boson called the gluon. The gluon carries a quantum number called color. Gluons come in eight colors ($\frac{R\bar{R}-B\bar{B}}{\sqrt{2}}$, $\frac{R\bar{R}+B\bar{B}-2G\bar{G}}{\sqrt{6}}$, $R\bar{G}$, $R\bar{B}$, $G\bar{R}$, $G\bar{B}$, $B\bar{R}$, and $B\bar{G}$) in order to mediate forces between each other and also the quarks. Hence, the quantum gauge field theory describing their interactions is called *quantum chromodynamics*.

Glashow, Weinberg, and Salam observed that it would be possible to unify two of these forces, namely electromagnetism and the weak nuclear force, to create the *electroweak* force. This unification can only occur due to *spontaneous symmetry breaking* and introduction of a yet unseen spin-0 gauge boson called the Higgs (H^0). This model is referred to as the SU(2)×U(1) model. Furthermore, it is possible to incorporate the strong nuclear force into this model which defines this gauge field theory called the Standard Model.

Even though the Standard Model has been successful in describing the state of particle physics to date, new theories attempt to explain its short-comings. This dissertation undertakes a search for evidence of Supersymmetry using like-sign dileptons in $p\bar{p}$ collisions at the center-of-mass energy, $\sqrt{s} = 1.8$ TeV, utilizing 106 pb^{-1} of data collected by the Collider Detector at Fermilab (CDF) in 1992-5. Theoretical concepts are introduced in Chapter II. The accelerator facility at Fermilab will be described in Chapter III. Details of the detector will be presented in Chapter IV. Chapter V will cover the dilepton data samples that will be analyzed. Results will be stated in Chapter VI. Conclusions will be stated in Chapter VII. The opportunity to write a dissertation of this magnitude could not be written without being part of a collaboration. The names of experimental collaborators are displayed in Appendix A.

CHAPTER II

THEORY

A. **Introduction**

Although the Standard Model has had tremendous success (*e.g.*, the prediction of the weak intermediate vector bosons and the discovery of the top quark), it leaves many important questions unanswered. It does not explain why are there three types of quarks and leptons of each charge. It does not explain a pattern to their masses. It does not explain why matter has mass. There is a desert between the electroweak scale and the Planck scale (the unification scale) in the Standard Model. An explanation for this gap in energy scales is yet to be found and it is called the *hierarchy problem*. Matter-antimatter asymmetry is not approached in Standard Model theories. Whether or not quarks and leptons have substructure is not discussed in the Standard Model. Gravitational interactions have not been incorporated into Standard Model theories. The Standard Model can not account for the invisible, dark matter which comprises much of the Universe. Furthermore, unification of the electromagnetic (α_1), weak nuclear (α_2), and strong nuclear (α_3) forces do not occur at any energy scale (see Fig. 1). Puzzles such as these also drive particle physicists to develop and study theories that go beyond the Standard Model. Moreover, new accelerators are built, so that higher-energy collisions can be observed to test these theories.

B. **Supersymmetry**

A very attractive extension of the Standard Model is Supersymmetry (SUSY), which describes a symmetry between fermions and bosons[1]. Having equal numbers of

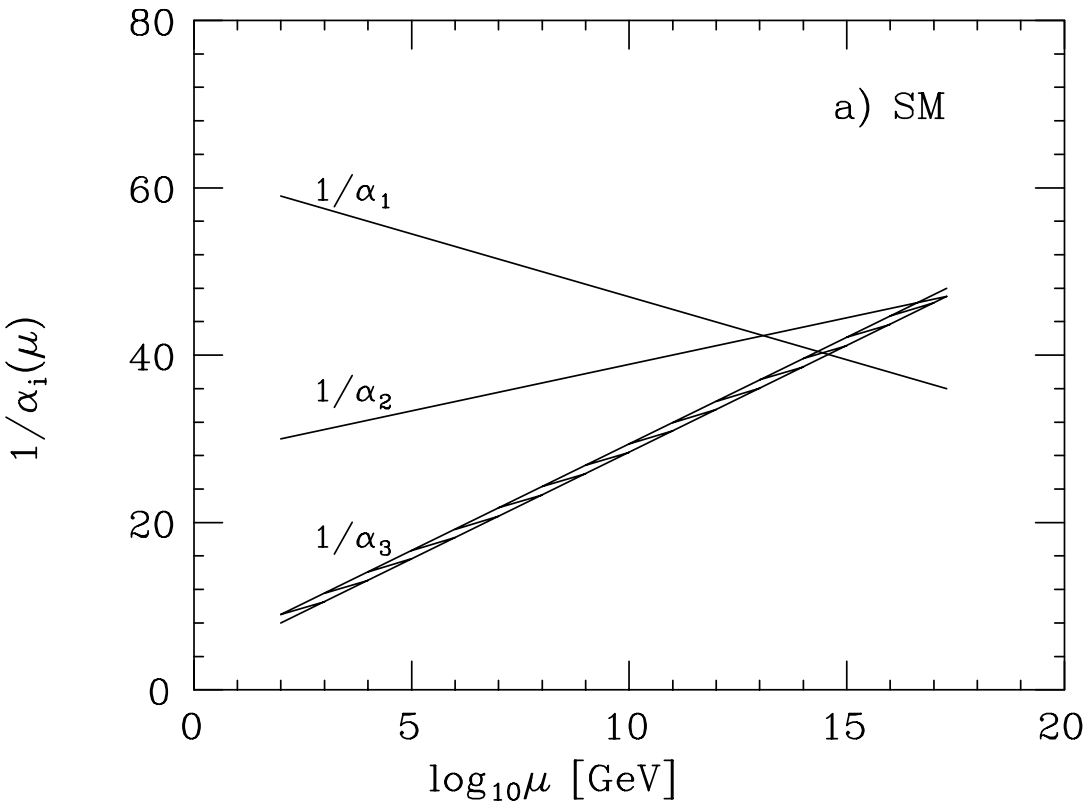

FIG. 1. The electromagnetic (α_1), weak nuclear (α_2), and strong nuclear (α_3) forces do not meet at any energy scale within the framework of the Standard Model. Taken from Ref. [4].

fermionic and bosonic degrees of freedom, SUSY theories assign each fermion a bosonic partner and vice versa. These new supersymmetric particles are called sparticles. Table II lists the particles and sparticles employing only two Higgs doublets in a minimalist version of Supersymmetry called the Minimal Supersymmetric Standard Model (MSSM)[2].

If SUSY were an exact symmetry, particles and their so-called superpartners would have equal masses. Thus, supersymmetry cannot be an exact symmetry of nature, and must be broken. The effective scale of supersymmetry braking is tied to the electroweak scale which is characterized by the Standard Model Higgs vacuum expectation value $v = 246$ GeV. Hence, searches for supersymmetry can be performed with today's accelerators.

Supersymmetry has many appealing qualities. Local supersymmetry provides in a natural way the unification of gravity with the strong and electroweak interactions ("supergravity")[3]. SUSY relates the Yukawa couplings and the self-couplings of the Higgs fields with the gauge couplings. In Grand Unified Theories (GUTs), SUSY solves the hierarchy problem. In SUSY, the running coupling constants are able to meet at a common value when scaled with energy (see Fig. 2)[4].

These purely theoretical motivations have been persuasive enough so that experimental physicists have started to look for signals of supersymmetry. At present, searching for SUSY particles is already an essential part of high energy physics and will play an even more important role in the experimental program of new accelerators.

However, present SUSY models suffer from a great number of free parameters. Furthermore, SUSY gives neither an explanation of the quark and lepton mass-spectrum nor of the origin of the three families.

TABLE II. Standard Model and MSSM particle spectrum.

Quarks				Squarks			
(spin-$\frac{1}{2}$)	$\begin{pmatrix} u \\ d \end{pmatrix}_L$	u_R d_R		(spin-0)	$\begin{pmatrix} \tilde{u} \\ \tilde{d} \end{pmatrix}_L$	$\tilde{u}_R$ $\tilde{d}_R$	
	$\begin{pmatrix} c \\ s \end{pmatrix}_L$	c_R s_R			$\begin{pmatrix} \tilde{c} \\ \tilde{s} \end{pmatrix}_L$	$\tilde{c}_R$ $\tilde{s}_R$	
	$\begin{pmatrix} t \\ b \end{pmatrix}_L$	t_R b_R			$\begin{pmatrix} \tilde{t} \\ \tilde{b} \end{pmatrix}_L$	$\tilde{t}_R$ $\tilde{b}_R$	$\longrightarrow$ $\tilde{t}_{1,2}$, $\tilde{b}_{1,2}$
Leptons				Sleptons			
(spin-$\frac{1}{2}$)	$\begin{pmatrix} e \\ \nu_e \end{pmatrix}_L$	e_R		(spin-0)	$\begin{pmatrix} \tilde{e} \\ \tilde{\nu}_e \end{pmatrix}_L$	$\tilde{e}_R$	
	$\begin{pmatrix} \mu \\ \nu_\mu \end{pmatrix}_L$	μ_R			$\begin{pmatrix} \tilde{\mu} \\ \tilde{\nu}_\mu \end{pmatrix}_L$	$\tilde{\mu}_R$	
	$\begin{pmatrix} \tau \\ \nu_\tau \end{pmatrix}_L$	τ_R			$\begin{pmatrix} \tilde{\tau} \\ \tilde{\nu}_\tau \end{pmatrix}_L$	$\tilde{\tau}_R$	$\longrightarrow$ $\tilde{\tau}_{1,2}$
Gauge bosons				Gauginos			
(spin-1)	g			(spin-$\frac{1}{2}$)	$\tilde{g}$		
	γ				$\tilde{\gamma}$		Neutralinos
	Z				$\widetilde{Z}$		$\{\tilde{\gamma}, \widetilde{Z}, \widetilde{H}^0_{1,2}\}$
	$W^\pm$				$\widetilde{W}^\pm$		$\longrightarrow \tilde{\chi}^0_{1,2,3,4}$
Higgs bosons				Higgsinos			Charginos
(spin-0)	h, H, A			(spin-$\frac{1}{2}$)	$\widetilde{H}^0_{1,2}$		$\{\widetilde{W}^\pm, \widetilde{H}^\pm\}$
	$H^\pm$				$\widetilde{H}^\pm$		$\longrightarrow \tilde{\chi}^\pm_{1,2}$

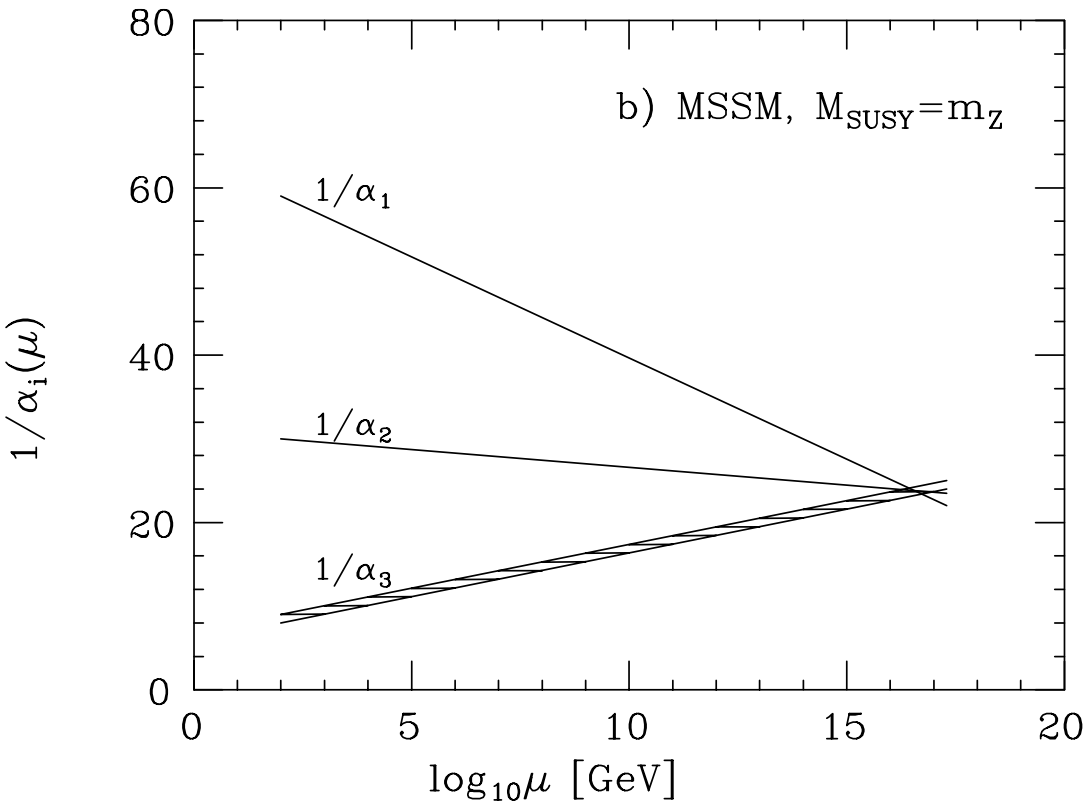

FIG. 2. The electromagnetic (α_1), weak nuclear (α_2), and strong nuclear (α_3) forces meet at a common energy scale with the assumption of the existence of Supersymmetry. Taken from Ref. [4].

1. Minimal Supersymmetric Standard Model

The MSSM[2] is the supersymmetric extension of the Standard Model with minimal particle content. In addition to the gauge bosons, gauge fermions (gauginos) are introduced. Quarks and leptons get spin-0 partners, so-called squarks and sleptons, one for each chirality state. Furthermore, two complex Higgs doublets with hypercharges $+1$ and -1 are assigned fermionic superpartners called higgsinos.

After electroweak symmetry breaking, the two Higgs doublets give mass to the $W^{\pm}$ and Z^0 bosons (and to up- and down-type (s)quarks). Thus, there are five physical Higgs bosons: two neutral scalars h^0 and H^0, one neutral pseudoscalar A^0, and two charged scalars H^+ and H^-. An important free parameter called $\tan\beta$ is defined as the ratio of the vacuum expectation values for the two Higgs doublets:

$$\tan\beta \;\; = \;\; v_u/v_d \tag{2.1}$$

where v_u (v_d) is the vacuum expectation value of the Higgs field which couples exclusively to up-type (down-type) quarks and leptons which are related to each other by:

$$v^2 \;\; = v_u^2 + v_d^2 \;\; = \tfrac{4M_W^2}{g^2} \tag{2.2}$$

where g is the dimensionless weak coupling and M_W is the mass of the W-boson. A_t and A_b are defined as the Higgs-squark-squark trilinear interaction for the top and bottom quark, respectively. $\tan\beta$ is bounded by unity from below and bounded from above by the ratio of the masses of the top and bottom quark. At the electroweak scale, gauginos mix with Higgsinos and receive additional mass contributions from the Higgs vacuum expectation values, v_u and v_d, due to a supersymmetric Higgsino mass mixing term, μ.

However, this one-to-one extension of the Standard Model is just a philosophical representation and does not give the physical states which must be derived as linear

combinations of the respective fields. The mass-eigenstates of the charged gauginos and higgsinos mix to form charginos ($\tilde{\chi}^{\pm}_{1,2}$); and the mass-eigenstates of the neutral gauginos and higgsinos combine to yield neutralinos ($\tilde{\chi}^{0}_{1,2,3,4}$). Thus, there are 2 charginos and 4 neutralinos (see Table II).

At high energies, GUTs are not necessarily held to the requirement of conserving lepton (L) or baryon number (B) separately. But since matter must either exist or annihilate with antimatter to create energy, a conservation number must still hold. This conservation is $B - L$ invariance. This principle gives GUTs the freedom to include proton decay if it is found to exist. In MSSM, $B - L$ invariance leads to a conservation of a multiplicative quantum number called R-parity, where $R = (-1)^{3(B-L)+2S}$ for a particle of spin S. The consequence of the conservation of R-parity is that supersymmetric particles are pair-produced and that the lightest supersymmetric particle (LSP) is stable. Grand unification requires that the LSP be colorless and neutral. Hence, the LSP is the lightest neutralino ($\tilde{\chi}^{0}_{1}$).

The existence of the superparticles below 1 TeV generally leads to large Flavor Changing Neutral Currents (FCNC), especially in K^0-$\bar{K}^0$ oscillations. To avoid this, one requires the squark masses in the 1^{st} and 2^{nd} generations to be highly degenerate. Non-universal models can be constructed, but they cannot deviate greatly from the universal ones in the FCNC channels [5]. Thus, four squark masses are approximately degenerate and the top-squarks (stops) and the bottom squarks (sbottoms) could be lighter (or heavier) than other squarks with the mass splittings due to left-right mixing [6] :

$$\left.\begin{aligned} \Delta M^2_{\tilde{b}} &= m_b(A_b - \mu \tan\beta) \\ \Delta M^2_{\tilde{t}} &= m_t(A_t - \tfrac{\mu}{\tan\beta}) \end{aligned}\right\} \tag{2.3}$$

2. Supergravity Inspired MSSM (SiMSSM)

Due to the fact that MSSM already has many parameters, a supergravity inspired MSSM model (SiMSSM) is used. Slepton and sneutrino masses are related to squark and gluino masses as inspired by supergravity models [7]:

$$\left.\begin{aligned} M^2_{\tilde{\ell}_L} &= M^2_{\tilde{q}} - 0.73 M^2_{\tilde{g}} - 0.27 M^2_Z \cos 2\beta \\ M^2_{\tilde{\ell}_R} &= M^2_{\tilde{q}} - 0.78 M^2_{\tilde{g}} - 0.23 M^2_Z \cos 2\beta \\ M^2_{\tilde{\nu}_L} &= M^2_{\tilde{q}} - 0.73 M^2_{\tilde{g}} + 0.5 M^2_Z \cos 2\beta \end{aligned}\right\} \tag{2.4}$$

where $M_{\tilde{g}}$ is the mass of the gluino, $M_{\tilde{q}}$ is the average mass of the squarks, M_Z is the mass of the Z-boson, and $\cos 2\beta$ is related to $\tan\beta$.

Here, masses of all generations of each type slepton ($\tilde{\ell_L}$, $\tilde{\ell_R}$, and $\tilde{\nu_L}$) are assumed to be degenerate. The equations, which are approximate compared to the minimal supergravity model (mSUGRA), require $M_{\tilde{q}} \gtrsim 0.9 M_{\tilde{g}}$. If the gluinos and squarks are rather close in mass, the sleptons can be considerably lighter than squarks. One big difference from the mSUGRA model is that the unification of Higgs masses is not assumed. Thus, μ (the Higgsino mixing parameter) is allowed to vary.

In this framework, stops are set slightly heavier than or equal to the other squarks by fixing $A_t = \mu/\tan\beta$, which suppresses the mixing between $\tilde{t}_{\rm L}$ and $\tilde{t}_{\rm R}$. Furthermore, mixing between $\tilde{b}_{\rm L}$ and $\tilde{b}_{\rm R}$ are suppressed by choosing $A_b = \mu\tan\beta$. In the search described in this analysis, top squarks ($\tilde{t}$) are excluded. In other words, the choice of A_t, A_b, and the exclusion of top squarks implies that the search is based on the assumption of five flavor degenerate squarks. To avoid a region in MSSM parameter space where there are significant chargino or neutralino branching ratios into Higgs particles, the mass of the pseudoscalar Higgs boson (A^0) is raised above the chargino and neutralino masses ($M_{A^0} = 500$ GeV/c^2).

C. Gluinos and Squarks

1. Production of Gluinos and Squarks

The Feynman diagrams displaying the production mechanisms are seen in Fig. 3. The cross-sections of $p\bar{p} \rightarrow \tilde{g}\tilde{g}$, $\tilde{g}\tilde{q}$, $\tilde{q}\tilde{q}$, and $\tilde{q}\bar{\tilde{q}}$ is determined at the next-to-leading order (NLO) (see Fig. 4)[8].

The renormalization and factorization scale, Q^2, presents the largest theoretical uncertainty in the calculation of the cross-section [8]. This uncertainty is $\simeq 50\%$ for the leading order (LO) cross-section. For the next-to-leading order (NLO) cross-section, this uncertainty drops to $\simeq 20\%$ (see Fig. 5).

2. Searches for Gluinos and Squarks

The "classic" missing transverse energy ($\not\!\!E_{\rm T}$) plus multijet channel involves searching for the direct and cascade decays of squarks and gluinos into quarks plus a lightest supersymmetric particle (LSP; $\tilde{\chi}_1^0$). This search had been pursued by UA1 [9], UA2 [10], and LEP [11] at CERN and by CDF [12, 13] and D0 [14].

Complementary to the classic $\not\!\!E_{\rm T}$+multijets analysis in the search for $\tilde{g}\tilde{g}$ production, a like-sign (LS) dilepton approach has been proposed to maximize the experimental sensitivity [15, 16, 17, 18]. Squarks and gluinos can decay to the lightest chargino ($\tilde{\chi}_1^{\pm}$) and next-to-lightest neutralino ($\tilde{\chi}_2^0$) as seen in Fig. 6. Figure 7 demonstrates the leptonic body decay modes for charginos (left) and neutralinos (right). These modes occur when the slepton mass is larger than the chargino and neutralino masses so the decays occur via virtual $W^{\pm}$s and Z^0s (top) or sleptons (bottom).

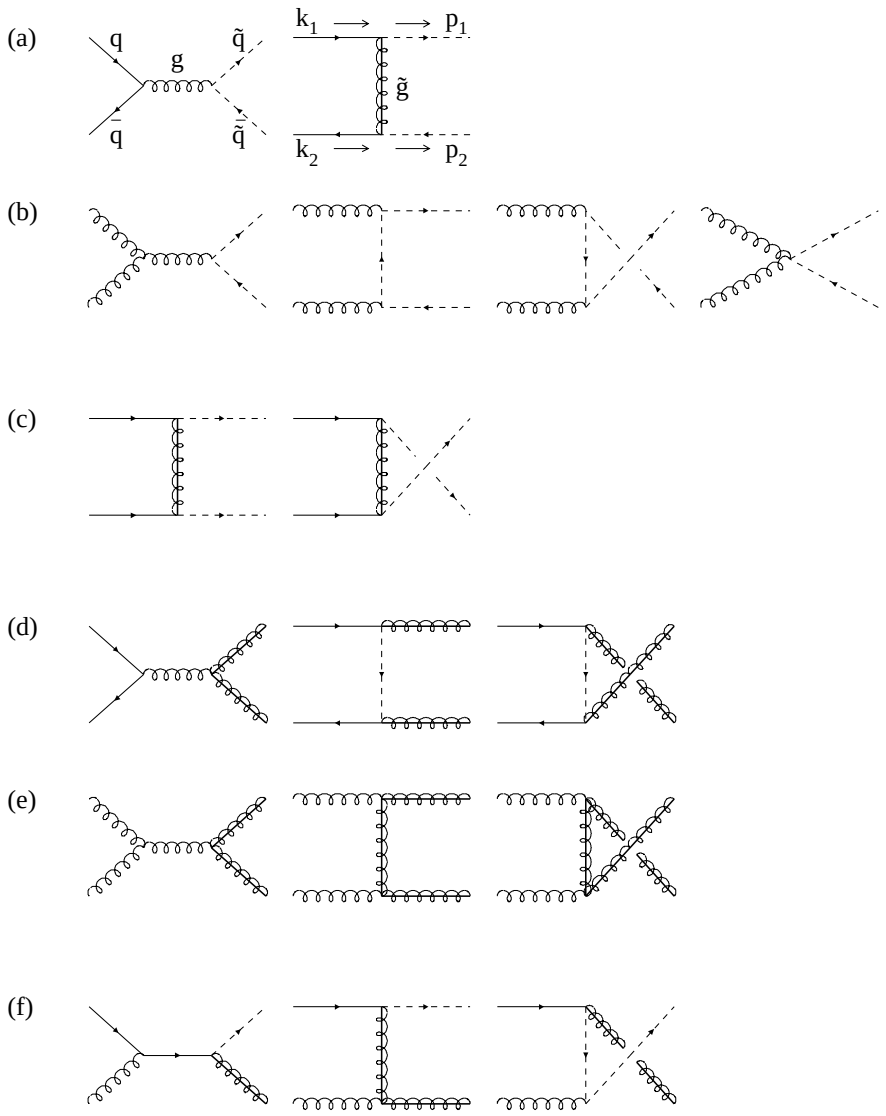

FIG. 3. Feynman diagrams for the production of squarks and gluinos in lowest order. The diagrams without and with crossed final-state lines [*e.g.*, in (b)] represent t- and u- channel diagrams, respectively. The diagrams in (c) and the last diagram in (d) are a result of the Majorana nature of gluinos. Note that some of the above diagrams contribute only for specific flavors and chiralities of the squarks. Taken from Ref. [8].

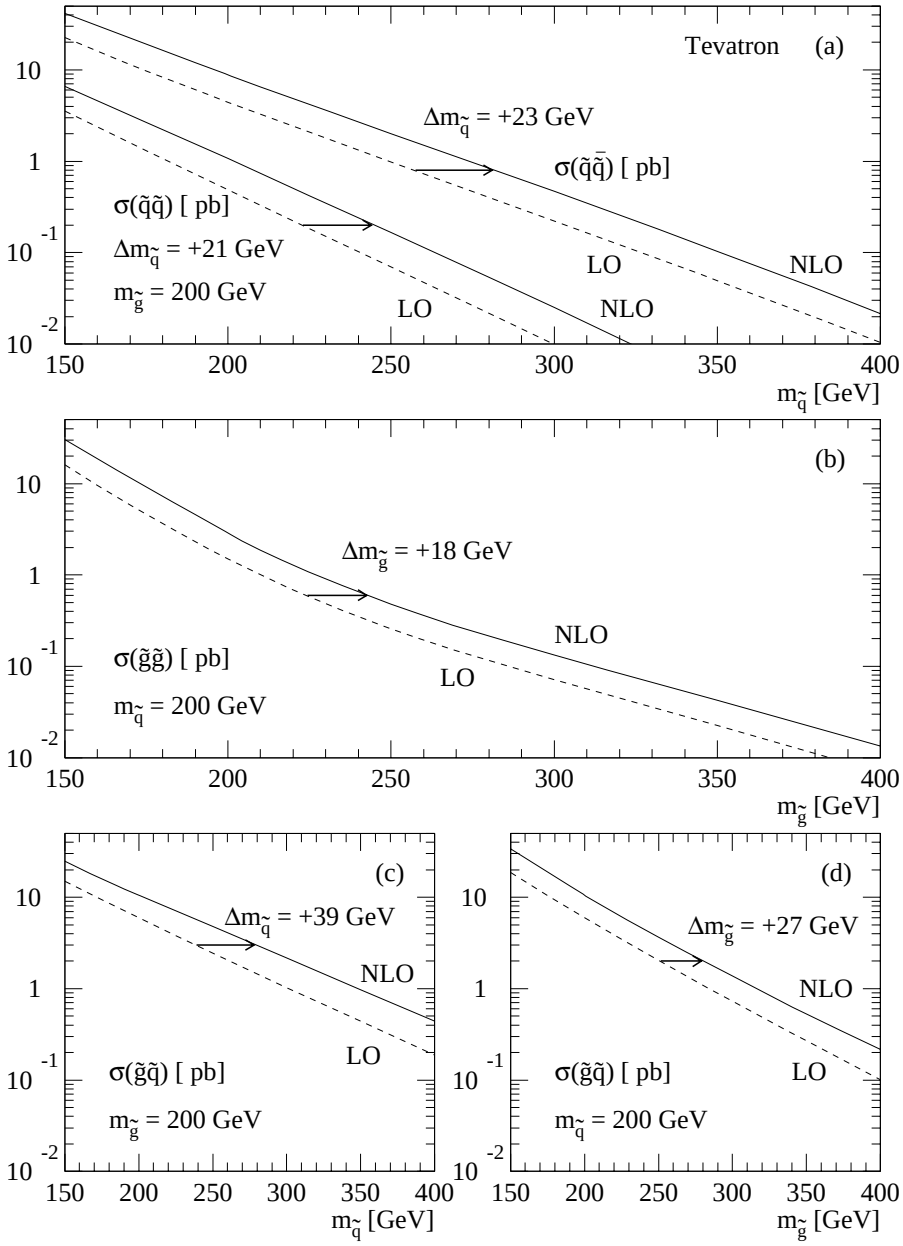

FIG. 4. The total cross-section for the $\tilde{g}\tilde{g}$, $\tilde{g}\tilde{q}$, $\tilde{q}\tilde{q}$, and $\tilde{q}\bar{\tilde{q}}$ at the Fermilab Tevatron ($\sqrt{s}$ =1.8 TeV). NLO (solid): GRV94 parton densities, with scale $Q^2 = m^2$; compared with LO (dashed): EHLQ parton densities, at the scale $Q^2 = s$. Taken from Ref. [8].

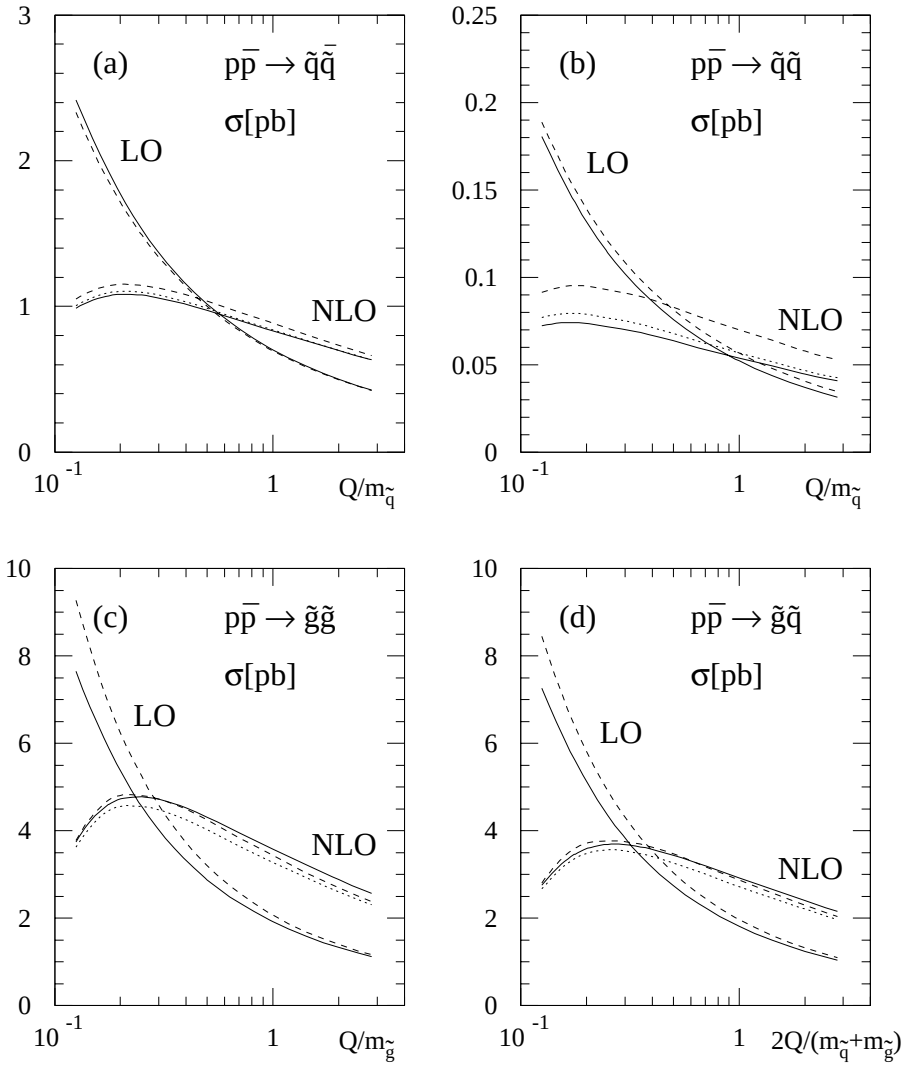

FIG. 5. The dependence on the Q scale for the LO and NLO cross-sections for (a) $\tilde{q}\bar{\tilde{q}}$, (b) $\tilde{q}\tilde{q}$, (c) $\tilde{g}\tilde{g}$, and (d) $\tilde{q}\tilde{g}$ production at the Fermilab Tevatron ($\sqrt{s}$ =1.8 TeV). Parton densities: GRV94 (solid), CTEQ3 (dashed), and MRS(A') (dotted) for $m_{\tilde{q}} = 280$ GeV/c^2 and $m_{\tilde{g}} = 200$ GeV/c^2. Taken from Ref. [8].

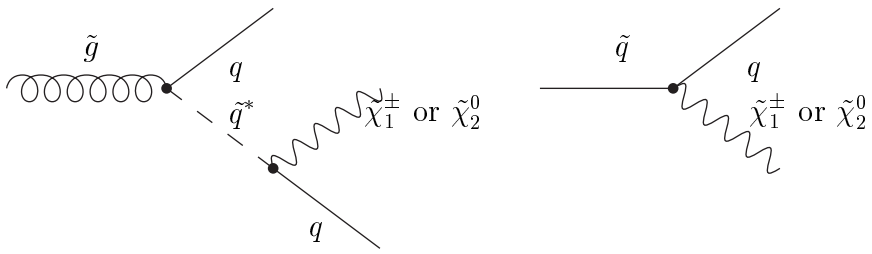

FIG. 6. Gluino/squark cascade decay.

The semileptonic cascade decays therefore are :

$$\left.\begin{array}{rcl}
\tilde{g}\tilde{g} & \to & (qq'\ell\nu_\ell\tilde{\chi}_1^0)(q\bar{q}\ell^+\ell^-\tilde{\chi}_1^0) \\
\tilde{g}\tilde{g} & \to & (q\bar{q}\ell^+\ell^-\tilde{\chi}_1^0)(q\bar{q}\ell^+\ell^-\tilde{\chi}_1^0) \\
\tilde{g}\tilde{g} & \to & (qq'\ell\nu_\ell\tilde{\chi}_1^0)(qq'\ell\nu_\ell\tilde{\chi}_1^0) \\
\tilde{g}\tilde{g} & \to & (q\bar{q}\ell^+\ell^-\tilde{\chi}_1^0) + X
\end{array}\right\} \tag{2.5}$$

$$\left.\begin{array}{rcl}
\tilde{g}\tilde{q} & \to & (qq'\ell\nu_\ell\tilde{\chi}_1^0)(q\ell^+\ell^-\tilde{\chi}_1^0) \\
\tilde{g}\tilde{q} & \to & (qq'\ell\nu_\ell\tilde{\chi}_1^0)(q'\ell\nu_\ell\tilde{\chi}_1^0) \\
\tilde{g}\tilde{q} & \to & (q\bar{q}\ell^-\ell^+\tilde{\chi}_1^0)(q\ell^+\ell^-\tilde{\chi}_1^0) \\
\tilde{g}\tilde{q} & \to & (q\bar{q}\ell^-\ell^+\tilde{\chi}_1^0)(q'\ell\nu_\ell\tilde{\chi}_1^0) \\
\tilde{g}\tilde{q} & \to & (q\bar{q}\ell^+\ell^-\tilde{\chi}_1^0) + X \\
\tilde{q}\tilde{g} & \to & (q\ell^+\ell^-\tilde{\chi}_1^0) + X
\end{array}\right\} \tag{2.6}$$

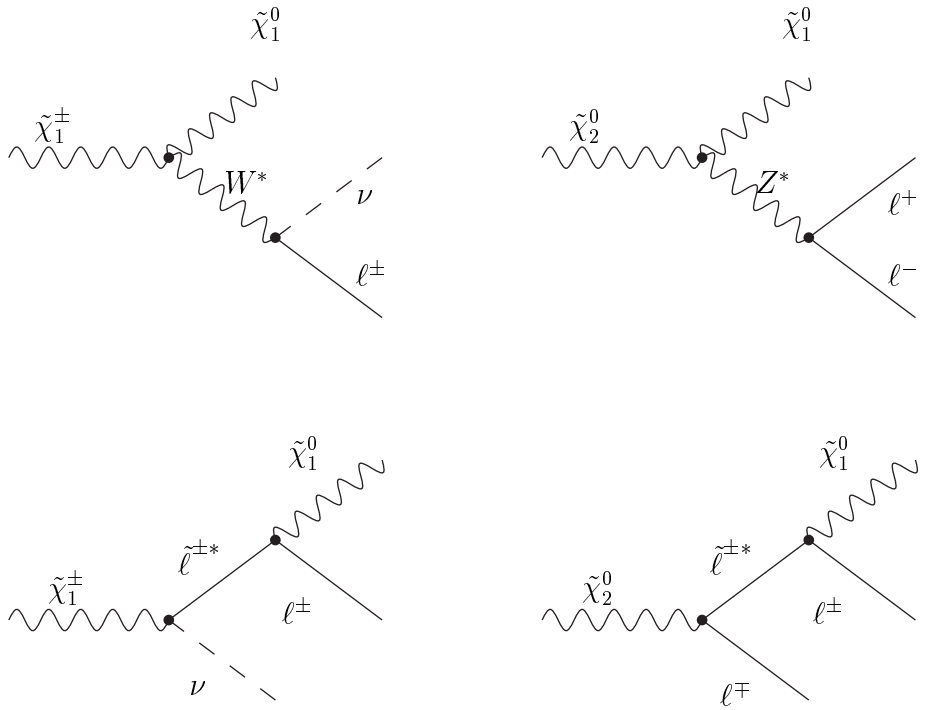

FIG. 7. Leptonic decay modes for charginos and neutralinos.

$$\left.\begin{aligned}
\tilde{q}\tilde{q} &\rightarrow (q'\ell\nu_\ell\tilde{\chi}_1^0)(q'\ell\nu_\ell\tilde{\chi}_1^0) \\
\tilde{q}\tilde{q} &\rightarrow (q\ell^+\ell^-\tilde{\chi}_1^0)(q\ell^+\ell^-\tilde{\chi}_1^0) \\
\tilde{q}\tilde{q} &\rightarrow (q'\ell\nu_\ell\tilde{\chi}_1^0)(q\ell^+\ell^-\tilde{\chi}_1^0) \\
\tilde{q}\tilde{q} &\rightarrow (q\ell^+\ell^-\tilde{\chi}_1^0) + X
\end{aligned}\right\} \tag{2.7}$$

The branching ratio to two or more leptons (e or μ) from decays of $\tilde{\chi}_1^\pm$ and $\tilde{\chi}_2^0$ as a function of gluino mass for $\tilde{g}\tilde{g}$, $\tilde{g}\tilde{q}$, $\tilde{q}\bar{\tilde{q}}$, and $\tilde{q}\tilde{q}$ can be seen for the cases where the squark and gluino mass are the same and where the squark is much heavier than the gluino in Fig. 8. These rates seen as appreciable for this search.

Equations 2.5-2.7 illustrate that there are at least two jets associated with the partons in the decay as well as significant $\not\!\!E_{\rm T}$ from the $\tilde{\chi}_1^0$ escaping the detector. Hence, $\tilde{g}\tilde{g}$, $\tilde{g}\tilde{q}$, and $\tilde{q}\tilde{q}$ pairs can yield dileptons, two or more jets, and missing energy. Since the gluino is a Majorana particle (*i.e.*, it is its own anti-particle), leptons of either charge may be expected in the decay chain. The majority of Standard Model background processes contains opposite-sign dileptons; and a sizable fraction of dileptons from supersymmetric processes display a like-sign signature. Hence, the like-sign requirement greatly reduces the background while retaining a sizable fraction of signal.

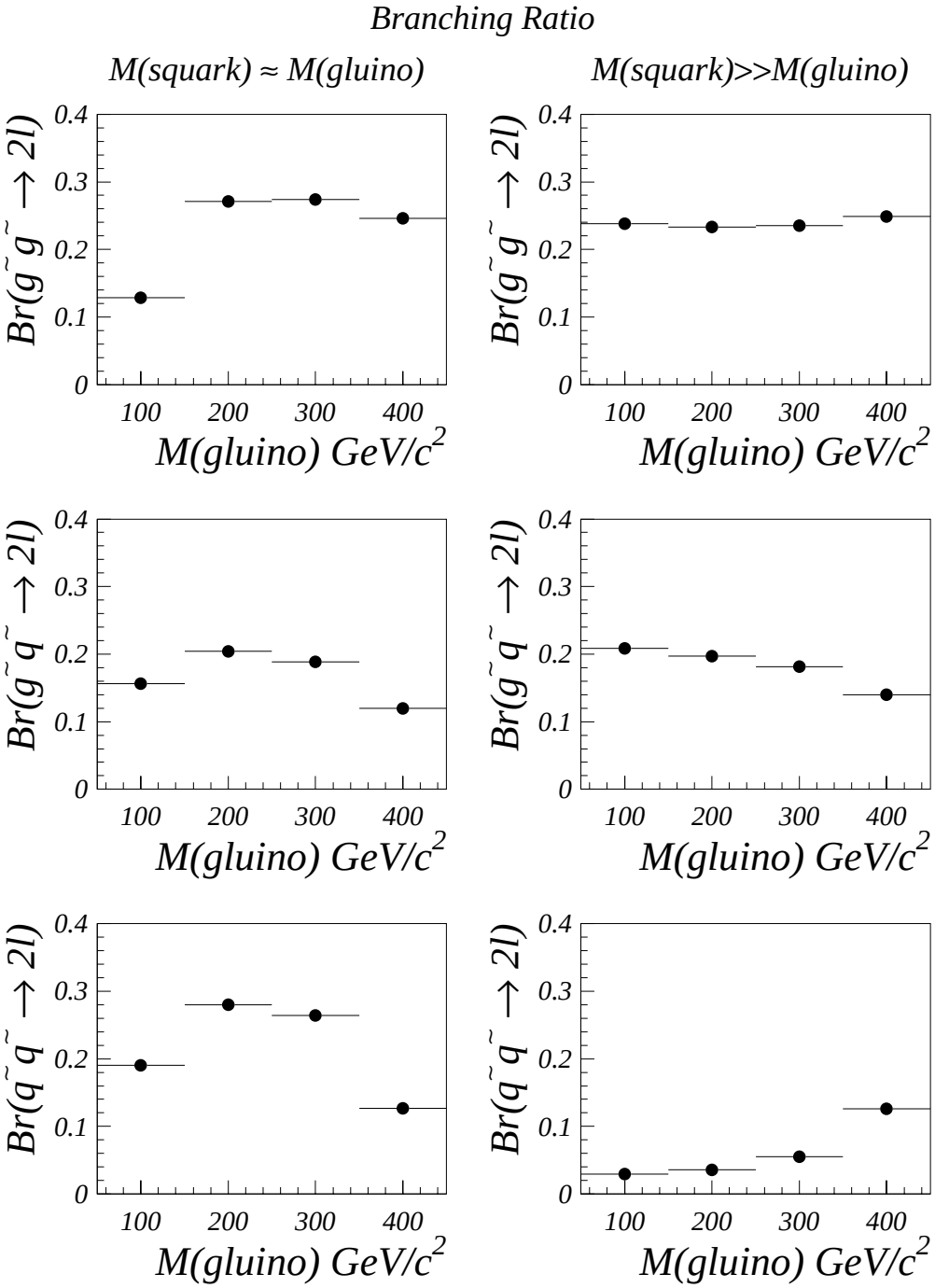

FIG. 8. Branching ratio of $\tilde{g}\tilde{g}$, $\tilde{g}\tilde{q}$, $\tilde{q}\bar{\tilde{q}}$, and $\tilde{q}\tilde{q}$ to dileptons (ee, $e\mu$, and $\mu\mu$) as a function of gluino mass for two squark mass scales.

CHAPTER III

THE FERMILAB ACCELERATOR

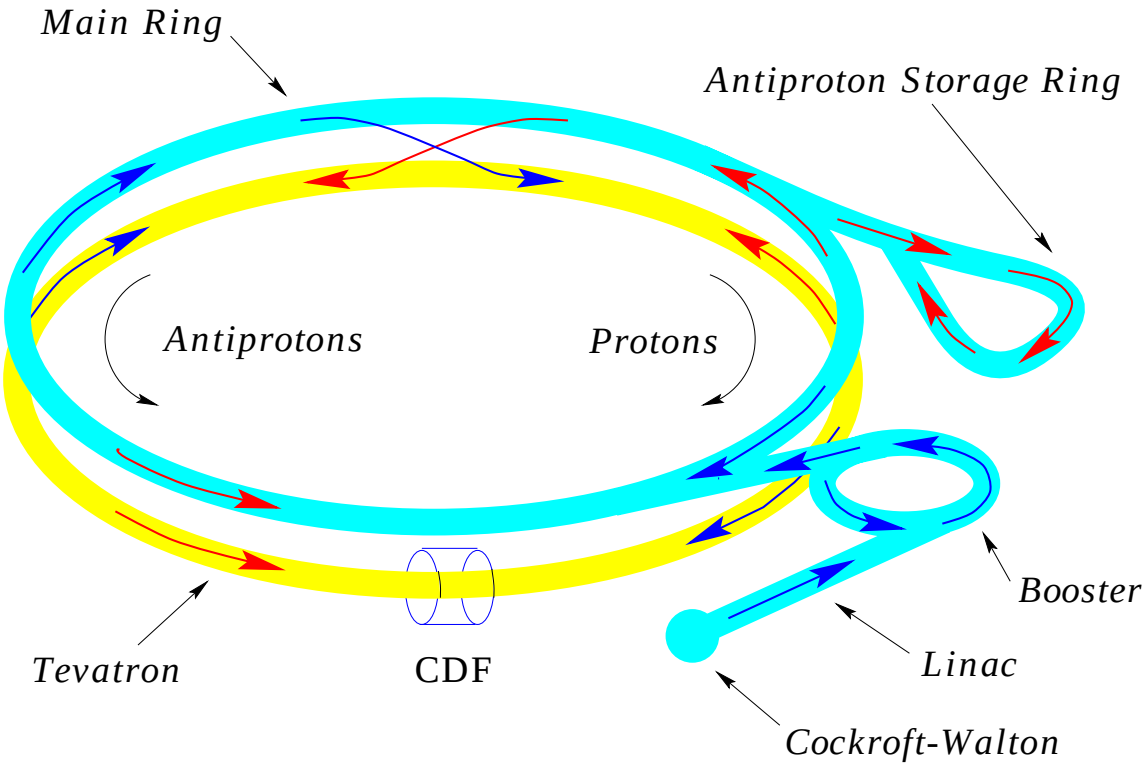

FIG. 9. The Fermilab Accelerator showing the stages of acceleration.

A. **Introduction**

The colliding beam machine (Tevatron) at Fermilab was proposed 23 years ago, and it was completed in 1985 [19]. Such a proposal to build a proton-antiproton collider was the idea that helped CERN to first discover the W and Z bosons [20]. The Tevatron was at the right energy and luminosity that allowed CDF and D0 discover the top quark [21, 22].

Figure 9 shows the paths taken by protons and antiprotons in Fermilab's five accelerators. The beam of particles begin as negative hydrogen ions at the right in

the Cockcroft-Walton accelerator. They continue down the short, straight section, the Linac. As the beam of negative hydrogen ions enters the third accelerator, the circular Booster, both electrons are stripped off leaving a proton beam. The protons are injected into the upper ring, the Main Ring and then down into the lower ring, the Tevatron. In fixed target mode, the proton beam is extracted and sent down the Fixed Target beamline to the experimental areas.

When the accelerator is run in colliding beam mode, antiprotons are collected behind the Booster in the Antiproton Storage Rings. The antiprotons are injected into the Main Ring traveling in an opposite direction from the protons. The protons and antiprotons, each 100,000 times smaller than an atom, collide at a combined energy of nearly two trillion electron volts (1.8 TeV) inside two massive detectors named CDF and D0.

B. **Cockcroft-Walton Pre-accelerator**

The Cockcroft-Walton provides the first stage of acceleration. Gaseous hydrogen is extracted from a bottle and injected into the ion source. Electrons are then added to hydrogen atoms. The resulting negative ions, each consisting of two electrons and one proton, are attracted to a positive voltage and accelerated to an energy of 750,000 electron volts (750 keV).

C. **Linac**

After leaving the Cockcroft-Walton, negative hydrogen ions enter a linear accelerator called the Linac, which is approximately 150 m long. The original Linac consisted of nine vacuum tanks filled with small tubes, called drift tubes, spaced further and further apart. Now only the first five tanks remain and the last four have been

replaced. An electric field is applied to the tubes repeatedly reversing in direction. The particles travel through the drift tubes, hiding in them when the electric field is in a direction that would slow them down and emerging into the gaps between the drift tubes when the field is in the direction to speed them up. A recent upgrade replaced the last four tanks with a more efficient side-coupled Linac which uses the same principle of oscillating electric fields to accelerate the negative hydrogen ions to 400 million electron volts (400 MeV). Before entering the third stage, the Booster, the ions pass through a carbon foil which removes the electrons, leaving only the protons.

D. **Booster**

Located 6 m below ground, the Booster is a rapid cycling synchrotron 150 m in diameter. A synchrotron is a circular accelerator that uses magnets to bend electrically charged particles in a circular path so that they experience the repeated action of accelerating electric fields during each revolution. The protons travel around the Booster about 20,000 times and their energy is raised to eight billion electron volts (8 GeV). The Booster normally cycles twelve times in rapid succession, loading twelve pulses, or bunches of protons, into the Main Ring, the next stage of the acceleration process.

E. **Main Ring**

The Main Ring is another proton synchrotron which is 6 km in circumference. A tunnel 3 m in diameter, buried 6 m underground, houses 1,000 conventional, copper-coiled magnets which continually bend and focus the protons. Under current operating modes, the Main Ring accelerates protons to 150 billion electron volts (150 GeV).

F. **Tevatron**

The same tunnel that houses the Main Ring also contains the 1,000 superconducting magnets which comprise the proton synchrotron known as the Tevatron because of its ability to accelerate protons to nearly one trillion electron volts (900 GeV). The superconducting magnets form a ring directly below the the Main Ring magnets and operate in the temperature range of liquid helium (3 K). Superconducting magnets produce a larger magnetic field at a lower operating cost than conventional magnets.

G. **Antiproton Storage Rings**

Some of the experiments at Fermilab are performed by colliding a beam of protons with a beam of antiprotons. Each antiproton has the same mass as the proton but has the opposite electric charge. To produce the antiprotons, protons are first accelerated to an energy of 120 billion electron volts (120 GeV) in the Main Ring, extracted, transported to a target area, and focused on the target. The collisions in the target produce a wide range of secondary particles including many antiprotons. These are selected and transported to the Debuncher ring in bunches. These bunches are reduced in size by a process known as stochastic cooling. They are then transferred to the Accumulator ring for storage. Finally, when a sufficient number has been produced, the antiprotons are re-injected into the Main Ring and passed down into the Tevatron where they are accelerated simultaneously with a counter-rotating beam of protons to an energy of 900 GeV.

H. **The Detectors**

Beams of protons and antiprotons collide at nearly the speed of light in Fermilab's Tevatron particle accelerator. Two hundred and fifty thousand times a second,

proton-antiproton collisions burst into showers of secondary particles. The collisions take place inside each of two huge collider detectors on the accelerator ring. The detectors' job it is to observe as many collisions as possible, to recognize and record the particles that come flying out, and to preserve the information for later study.

By analyzing the stored data from the detectors, physicists are able to make discoveries about the fundamental nature of matter and energy. Physicists at Fermilab have been studying data from CDF and D0, the Laboratory's two collider detectors, and have found evidence of collisions that have produced the top quark, a previously undiscovered fundamental particle predicted by current scientific theory.

I. **Luminosity**

At a particle collider, the rate $\frac{dN}{dt}$ at which events of a given type occur is determined by the *luminosity* of the machine, $\mathcal{L}$, multiplied by the cross-section for the relevant scattering process, σ:

$$\frac{dN}{dt} = \mathcal{L}\sigma. \tag{3.1}$$

The machine luminosity is controlled by the parameters of the collider[23] :

$$\mathcal{L} = \frac{N_p N_{\bar{p}} B f_0}{4\pi\sigma_x\sigma_y} \tag{3.2}$$

where f_0 is the revolution frequency (50 kHz), B is the number of bunches (6), N_p is the number of protons/bunch ($\simeq 2 \times 10^{11}$), $N_{\bar{p}}$ is the number of antiprotons/bunch ($\simeq 6 \times 10^{10}$), and σ_x and σ_y characterize the Gaussian transverse beam profile in x and y ($\simeq 3 \times 10^{-3}$ cm). Hence, a typical number for luminosity during Run I is $\mathcal{L} \simeq 3 \times 10^{31}$ cm^{-2} s^{-1}.

The collider run at Fermilab which spanned the period from 1992-5 is denoted as Run I. By choice of convention, the first $\simeq 20$ pb^{-1} (1992-3) of Run I is referred to

as Run IA and the following 90 pb^{-1} (1994-5) of the collider run is designated as Run IB. This collider run has yielded much data for both the CDF and D0 collaborations.

CHAPTER IV

THE CDF DETECTOR

A. **Introduction**

CDF is a 5000 t magnetic spectrometer containing tracking detectors, calorimeters, muon chambers, as well as an electronic triggering system to record selected events [24]. CDF uses a right-handed coordinate system where the z-axis is along the proton direction, the y-axis is up and the x-axis is radially outward. The origin of this coordinate system lies at the center of the detector. A display of the detector showing its many components is presented in Fig. 10 segmented in *pseudorapidity*, η, which is defined by $\eta \equiv -ln\tan(\theta/2)$ and where θ is the polar angle measured relative to the incoming proton beam direction. Pseudorapidity is the relativistic limit of rapidity, y :

$$y \equiv \frac{1}{2} ln \left(\frac{E + p_z}{E - p_z} \right) \tag{4.1}$$

$$y = \frac{1}{2} ln \left(\frac{\cos^2(\theta/2) + m^2/4p^2 + ...}{\sin^2(\theta/2) + m^2/4p^2 + ...} \right) \tag{4.2}$$

$$y \simeq -ln\tan(\theta/2) \tag{4.3}$$

where E is the energy of the particle, p_z is the momentum of the particle along the z-axis, θ is the polar angle, p is the total momentum of the particle, and m is the mass of the particle. Since y is Lorentz invariant, the detector is segmented in pseudorapidity rather than polar angle in a detector at a hadron collider.

FIG. 10. A quadrant of the CDF detector displaying the segmentation of all components in pseudorapidity.

B. The Tracking Chambers

The tracking detectors lie inside a 1.4 T solenoidal magnetic field. The tracking chambers consist of (1) the silicon vertex (SVX) chamber, (2) the vertex time projection (VTX) chamber, and (3) the central tracking chamber (CTC).

1. Silicon Vertex Chamber

The silicon vertex detector (SVX), positioned immediately outside the beam pipe and inside the CTC, provides precise charged particle reconstruction and allows identifi-

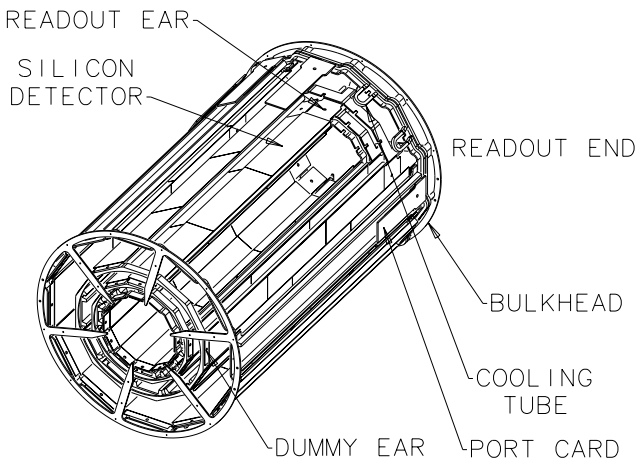

FIG. 11. A barrel of the SVX displaying 4 layers [27].

cation of secondary vertices from b-quark decays [27]. Figure 11 displays a barrel of the SVX and shows the four layers of silicon detectors which measure the r-ϕ position of tracks in the pseudorapidity range $\mid \eta \mid \leq 1$. A typical minimum ionizing particle creates about 20,000 electron-hole pairs in a single silicon layer generating a $r - \phi$ track as it passes through the 4-layer SVX.

2. **Vertex Time Projection Chamber**

Surrounding the SVX is the vertex time projection chamber (VTX) [26]. It is a drift chamber which is divided into octants. The gas composition is a 50%/50% Argon/Ethane which is bubbled through isopropyl alcohol at 7^o C. Each of the 8 modules is divided in z into two drift regions about 5 cm long and 8 octants in ϕ. Charged particles ionize the gas inside a VTPC cell and these ions drift towards the center of the modules where they are detected. This tracking system yields a 1 mm event vertex resolution. There are several combinations of track segments that yield primary vertex candidates. These are classified and stored in the VTVZ bank

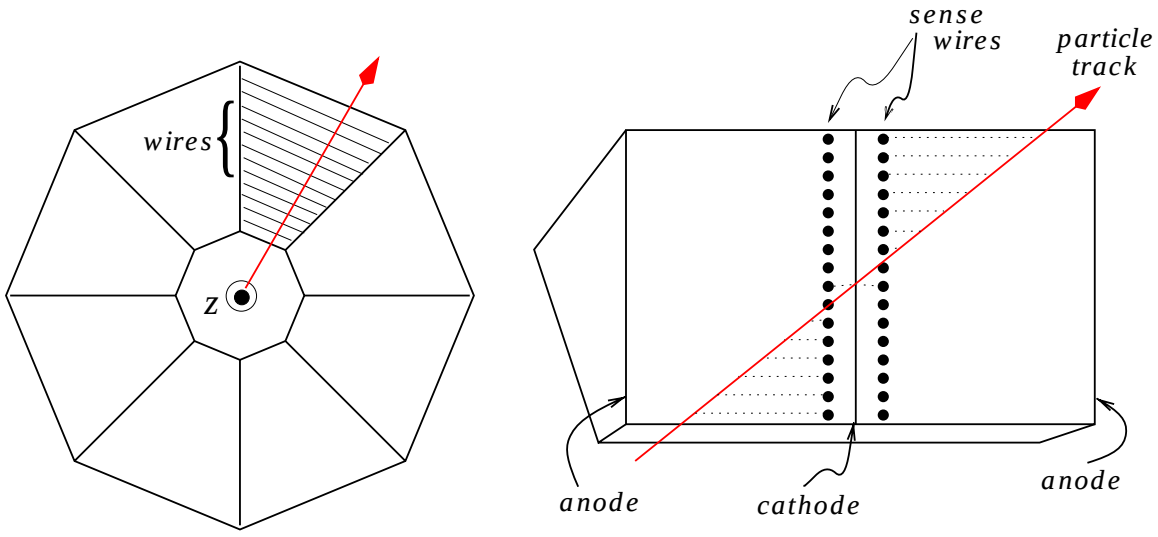

FIG. 12. The VTX. Left, a cross-sectional view of the VTX octants; right, a side view of one of the octants demonstrating the measurement of the vertex of the track [26].

upon data processing. Those vertex candidates with classification 12 or above are considered golden candidates for the vertex of the primary interaction. Figure 12 displays and demonstrates the measurement of the track vertex.

3. The Central Tracking Chamber

The central tracking chamber (CTC) is a 1.3 m radius 3.2 m long cylindrical drift chamber which measures the momenta of charged particles within a pseudorapidity range $\mid \eta \mid \leq 1.1$ [25]. In this region, the momentum resolution, $\frac{\delta p_T}{p_T^2}$ is less than 0.002 $(\mathrm{GeV}/c)^{-1}$. The chamber contains 84 layers of sense wires grouped into 9 "superlayers". Five of the superlayers consist of 12 axial sense wires; four stereo superlayers consist of 6 sense wires tilted by $\pm$ 3° relative to the beam direction. Figure 13 shows an endplate of the CTC displaying the 45° tilt of the superlayers to the radial direction to correct for the Lorentz angle of the electron drift in the 1.4 T magnetic field.

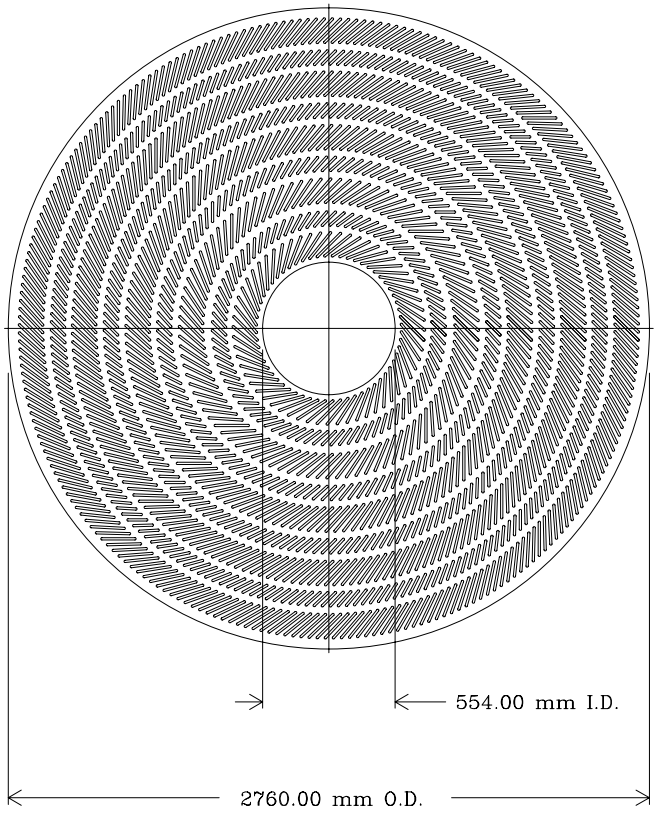

FIG. 13. An endplate of the central tracking chamber (CTC) showing the arrangement of the blocks which hold the 84 layers of sense wires [25].

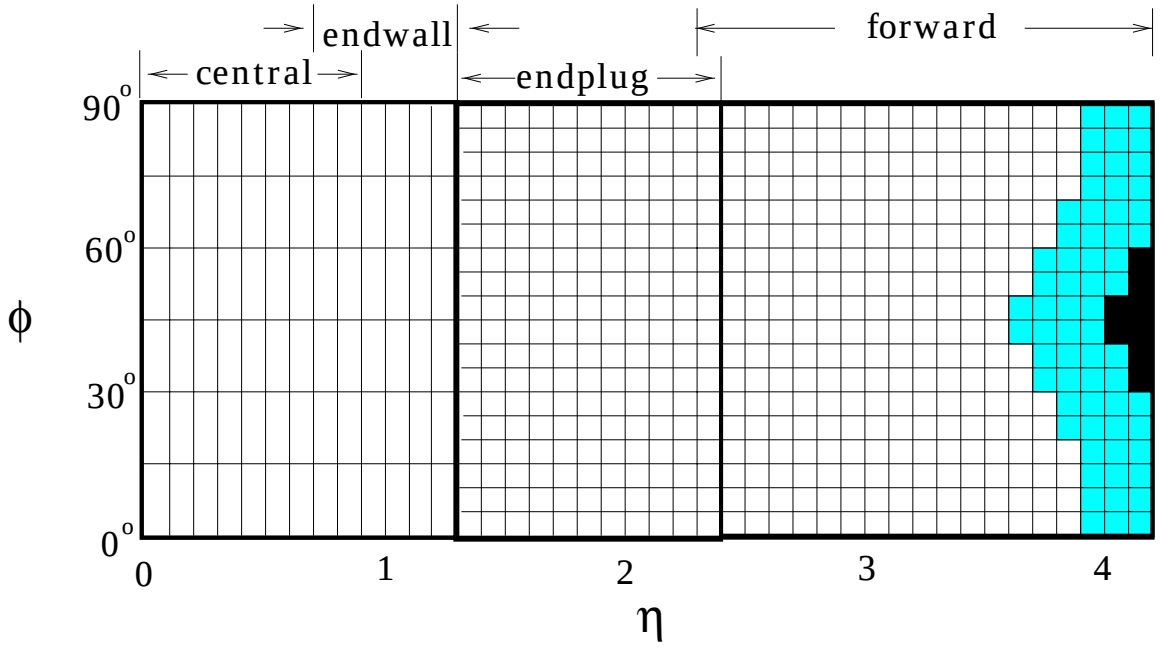

FIG. 14. The $\Delta\eta \times \Delta\phi$ segmentation of the CDF calorimetry.

C. **Calorimetry**

Since it is necessary to reconstruct the total energy for each event, a near 4π coverage of the detector is provided by the calorimetry. Electromagnetic and hadronic calorimeters, arranged in a projective tower geometry, surround the tracking volume and are used to identify jets, localized clusters of energy, within the range $\mid \eta \mid \leq 4.2$. The central calorimetry covers the pseudorapidity range $\mid \eta \mid \leq 1.1$. The plug and forward calorimetry (electromagnetic and hadronic) provides coverage in the pseudorapidity range $1.1 \leq \mid \eta \mid \leq 2.4$ and $2.4 \leq \mid \eta \mid \leq 4.2$, respectively, making CDF a nearly perfect detector. Figure 14 displays the $\Delta\eta \times \Delta\phi$ segmentation of the calorimetry.

The calorimeters at CDF measure energy of various kinds of particles using a method called *sampling*. This technique is a statistical one with the energy (E) being shared between the absorber and an actual sampling medium. For such a calorimeter, the energy (E) is proportional to the energy deposited in the sampling medium. The

TABLE III. Summary of the properties of the various CDF calorimeter systems.

System	η Coverage	Energy Resolution	Thickness
Central EM	$\lvert\eta\rvert < 1.1$	$13.7\%/\sqrt{E_{\mathrm{T}}} \oplus 2\%$	18 X_0
Plug EM	$1.1 < \lvert\eta\rvert < 2.4$	$22\%/\sqrt{E_{\mathrm{T}}} \oplus 2\%$	18-21 X_0
Forward EM	$2.2 < \lvert\eta\rvert < 4.2$	$25\%/\sqrt{E_{\mathrm{T}}} \oplus 2\%$	25 X_0
Central HAD	$\lvert\eta\rvert < 0.9$	$50\%/\sqrt{E_{\mathrm{T}}} \oplus 3\%$	4.5 λ_0
Endwall HAD	$0.7 < \lvert\eta\rvert < 1.3$	$75\%/\sqrt{E_{\mathrm{T}}} \oplus 4\%$	4.5 λ_0
Plug HAD	$1.3 < \lvert\eta\rvert < 2.4$	$106\%/\sqrt{E_{\mathrm{T}}} \oplus 4\%$	5.7 λ_0
Forward HAD	$2.4 < \lvert\eta\rvert < 4.2$	$106\%/\sqrt{E_{\mathrm{T}}} \oplus 4\%$	7.7 λ_0

experimental resolution σ is proportional to $\sqrt{E}$. The fractional energy resolution can then be expressed as :

$$\frac{\sigma(E)}{E} \propto \frac{1}{\sqrt{E}} \tag{4.4}$$

Thus, the fractional energy resolution improves as the energy deposition in the calorimeter is increased. Table III displays properties of several of CDF's calorimeter elements (The symbol $\oplus$ means that the constant term is added in quadrature to the resolution; λ_0 represents nuclear absorption lengths and X_0 radiation lengths.).

1. **Central Calorimetry**

The central calorimetry surrounds the CTC. It consists of two main components : the central electromagnetic calorimeter (CEM) and the central hadronic calorimeter (CHA). The CEM is designed to measure transverse electromagnetic energy such as photons and electrons. The CHA is responsible for observing the much more

penetrating objects which interact hadronically.

The central electromagnetic calorimeter (CEM) was developed in order to combine the good resolution of scintillator with the fine segmentation of one or more gas layers [28]. It is divided into 24 wedges of 15° in ϕ and is segmented into towers of $\Delta\eta$ of 0.1 totaling 480 towers on each side of the CEM. A CEM wedge consists of 31 5 mm SCSN-38 polystyrene layers alternating with 30 layers of 3.2 mm Pb totaling 18 radiation lengths as is displayed in Fig. 15. Six radiation lengths into the CEM is the central electromagnetic shower (CES) chamber, a set of proportional strip and wire chambers. This location is approximately at the point where the electromagnetic shower deposits its maximum energy. The CES provides both z and $r-\phi$ information about the shower and has resolution of ± 2 mm in each view as shown in Fig. 16. The central pre-radiator (CPR) is another set of proportional chambers between the CEM and the CTC that samples early development of the electromagnetic showers caused by the material of the solenoid coil.

The central hadronic calorimeter (CHA) consists of 48 steel-scintillator central modules with 2.5 cm sampling and 48 steel-scintillator endwall modules with 5 cm sampling [29]. Each calorimeter module is divided into projective towers, each covering approximately 0.1 unit in pseudorapidity and 15° in azimuthal angle, matching those of the electromagnetic calorimeter in front of it. It consists of about 4.7 interaction lengths. The CHA measures energy in the region $\mid \eta \mid \leq 0.7$.

The endwall hadronic calorimeter (WHA) is similar in design to the CHA. It consists of 15 layers of 5.1 cm steel absorber alternating with plastic scintillator which totals to 4.5 interaction lengths. It covers the region $0.7 \leq \eta \leq 1.3$. For the remainder of this text, WHA will be included in discussions of the CHA.

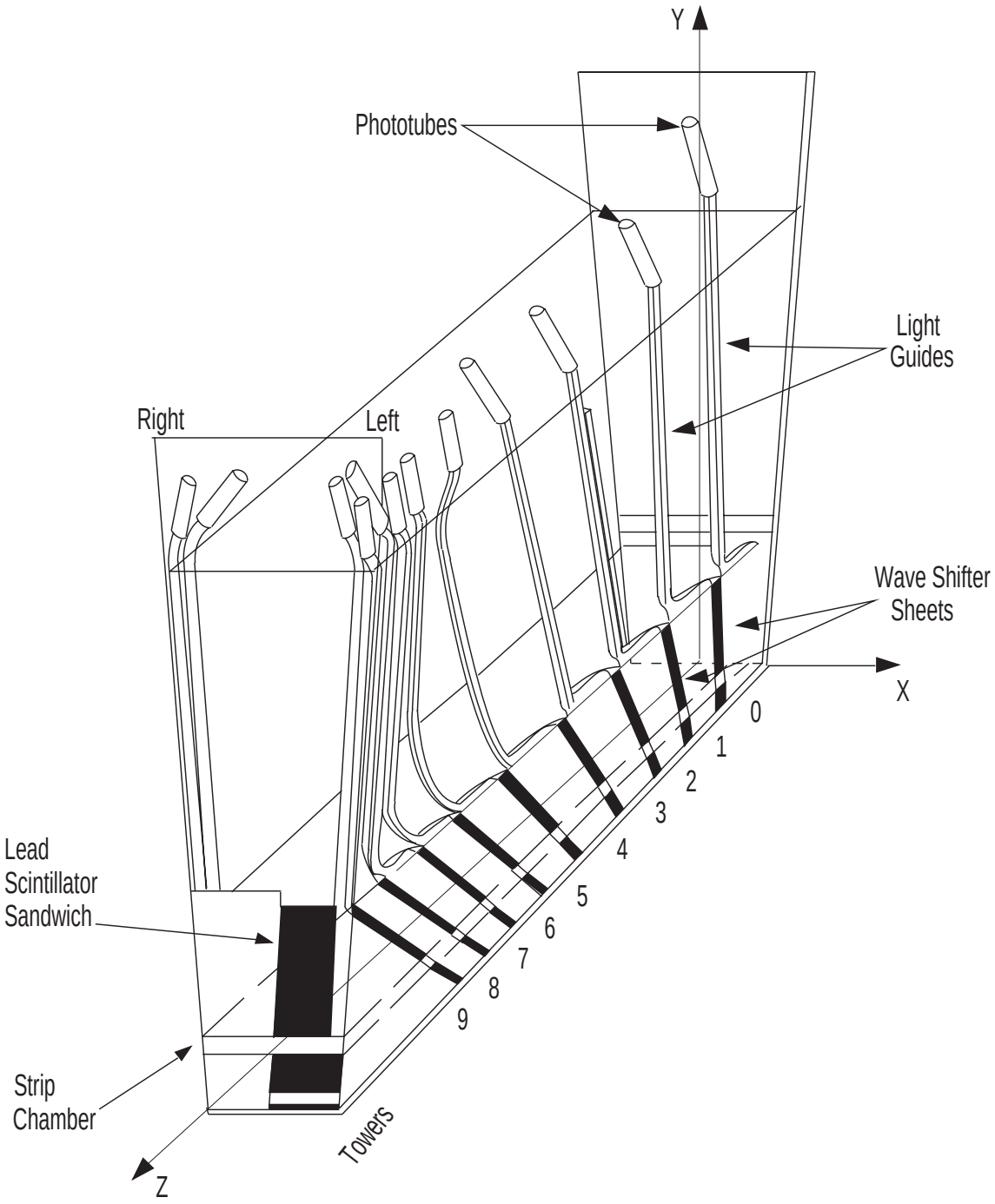

FIG. 15. A wedge of the central electromagnetic calorimeter [28].

FIG. 16. A section of the central electromagnetic shower chamber [28].

2. Plug and Forward Calorimetry

The central calorimeters use scintillator for good energy resolution and adequate radiation hardness. In the high $|\eta|$ regions of the detector, resolution becomes less critical and radiation exposure becomes a greater issue. In addition, finer transverse segmentation is needed in order to achieve the same position resolution seen in the central calorimeter. At the time of design and construction, this segmentation was difficult to achieve using a scintillator based calorimeter. As a result, all calorimeters in the region $1.1 \leq \eta \leq 4.2$ use gas (50/50 Argon/Ethane with a small percentage of alcohol) as an active medium.

The plug electromagnetic calorimeter (PEM) is a multi-wire gas (argon-ethane) proportional system, segmented into 72 5° ϕ wedges [30]. There are 34 tube arrays interleaved with 2.7 mm thick steel absorber. The PEM is about 19 radiation lengths thick and is segmented into towers of $(\Delta\eta = 0.1) \times (\Delta\phi = 5°)$. Just as in the CEM, the PEM has a detector placed at shower maximum. In the PEM it is a proportional system with finer granularity than the rest of the detector. A quadrant of the PEM is shown in Fig. 17.

The plug hadronic calorimeter (PHA) has 21 layers of 5.1 cm thick steel alternating with gas proportional tubes [31]. The PHA is about 6 absorption lengths. Each chamber has 72 cathode pads, arranged to project to the interaction region. The

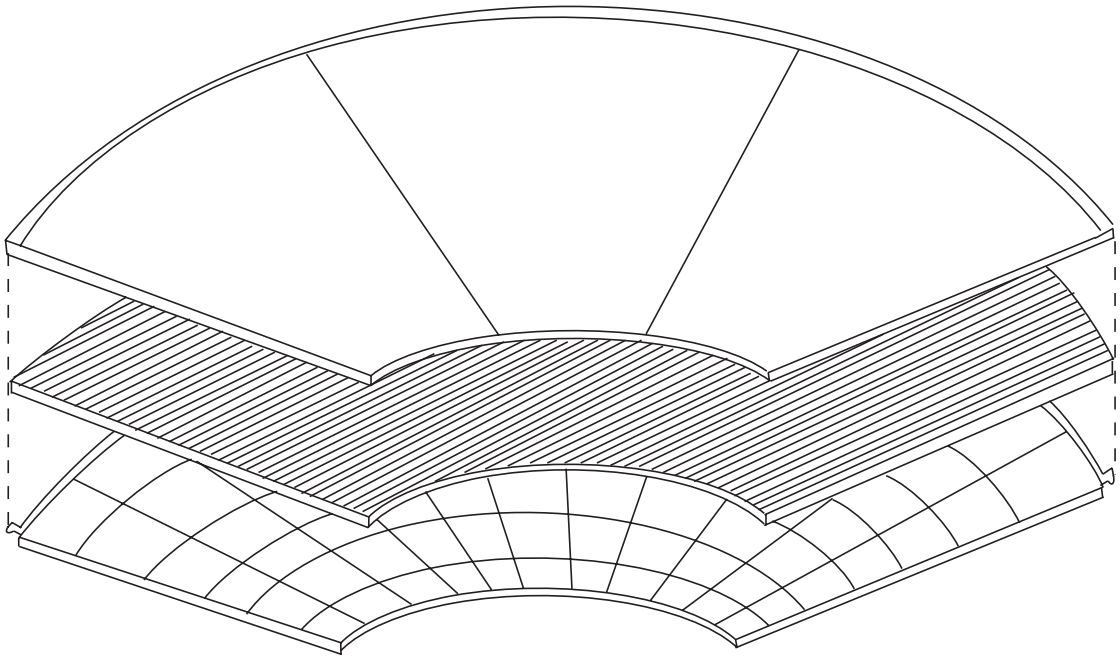

FIG. 17. A quadrant of the plug electromagnetic calorimeter [30].

50 μm gold plated tungsten anode wires are centered in resistive plastic tubes. The PHA is divided into 12 stacks of 30° in azimuthal angle. All anode wires in a single chamber are ganged and read out, giving longitudinal information from each plane in each stack.

The forward electromagnetic calorimeter (FEM) identifies electrons and photons in the region $2.2 \leq \eta \leq 4.2$ [32]. The FEM is 6.5 m from the interaction point and consists of 30 layers of lead alternating with gas sampling chambers. Each lead sheet is 0.8 X_0. The projective geometry is extended from the plug region in a grid of $\Delta\eta = 0.1 \times \Delta\phi = 5°$. The pads are ganged at constant η into two 15 layer regions. In each chamber, 124 anode wires are arranged vertically and are ganged together in five sectors for readout. The signals from the wires are useful for diagnostics and also provide a longitudinal shower profile. Each wire is strung inside a tube made from a repeated array of extruded aluminum T-shaped channels mounted on the cathode pad panel as shown in Fig. 18. The wires are 50 μm in diameter and are nickel flashed for a reliable solder connection. The cathode pad array is made from an etched layer of copper.

The forward hadronic calorimeter (FHA) was built to provide coverage in the range $2.2 \leq \eta \leq 4.2$ [33]. The chamber is nearly identical to that of the FEM. There are 27 layers of 5 cm steel interleaved with the chambers in each of the eight quadrants. In each chamber, the anode wires are segmented into six regions for readout. Cathode pad signals are summed in towers of η and ϕ. The FHA has been serviced and maintained during the course of Run I by the Texas A&M University group working on CDF [34]. Figure 19 shows a segmented quadrant of the FHA.

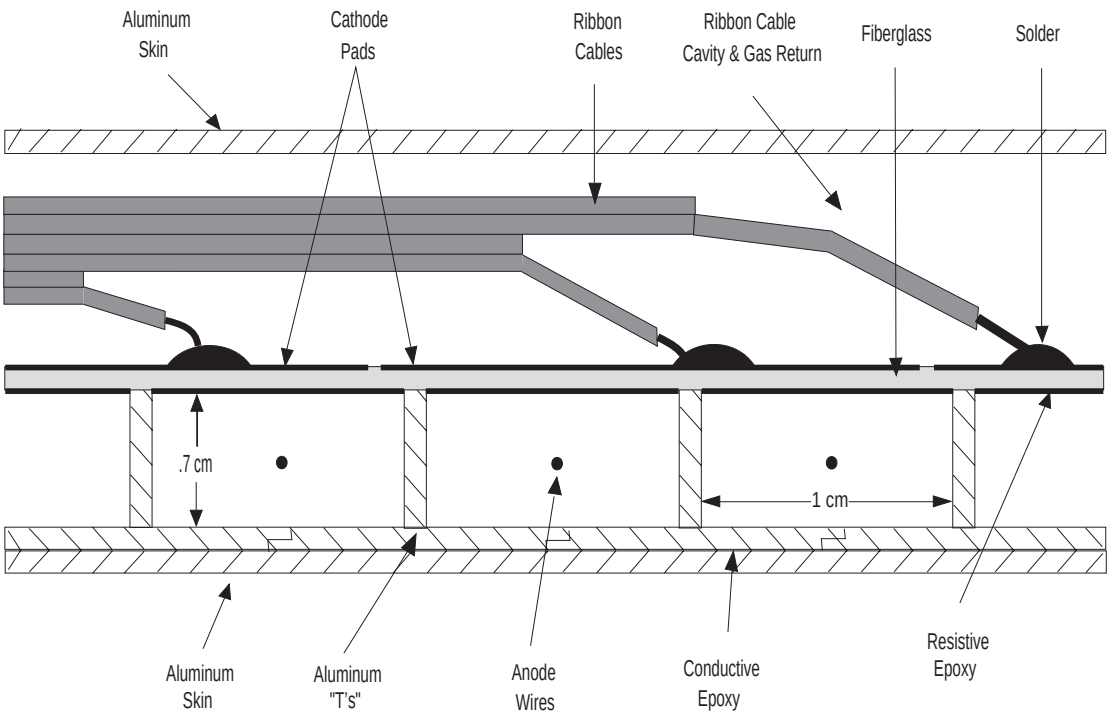

FIG. 18. Cross-section of the forward electromagnetic calorimeter chamber [32].

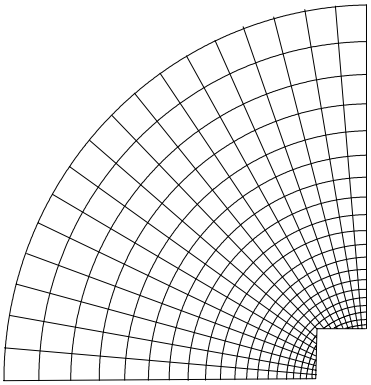

FIG. 19. A quadrant of the forward hadron calorimeter [33].

D. Muon Chambers

The central muon chambers (CMU and CMP) and the central muon extension (CMX) are used to identify muons. Since muons are only weakly and electromagnetically interacting, these detectors lie outside much of the calorimetry. Muons can therefore be identified as a penetrating minimum ionizing particles which escape the central volume of the detector leaving only a charged track in the tracking chambers. These detectors are drift chambers and are further described below. The coverage of the muon chambers in $\eta - \phi$ space is shown in Fig. 20.

1. Central Muon Chambers

The central muon chambers (CMU) are directly outside the CHA, using the calorimeters as a hadron absorber (approximately 5 interaction lengths) [35]. The CMU consists of 24 15^{o} wedges with each wedge consisting of 6 towers. Each tower radially consists of 4 layers of drift chambers and covers the region $|\eta| < 0.6$. A muon must have $p_{\mathrm{T}} \geq 1.4$ GeV/c to reach the CMU. Outside the CMU is an additional 0.6 m of steel (approximately 8 interaction lengths) and then 4 more layers of drift chambers known as the central muon upgrade (CMP). Approximately 84% of the detector is covered by the CMU, 63% by the CMP and 53% by both. The CMP, behind additional absorber, is very useful in reducing fake muons which are actually punch-though from energetic jets. Figure 21 displays a cell of the CMU cell.

2. Central Muon Extension

The central muon extension (CMX) covers the region $0.6 < |\eta| < 1.0$ and is a set of four free-standing conical arches. Each arch contains drift chambers for muon detection sandwiched between scintillators for triggering. Approximately 71% of the

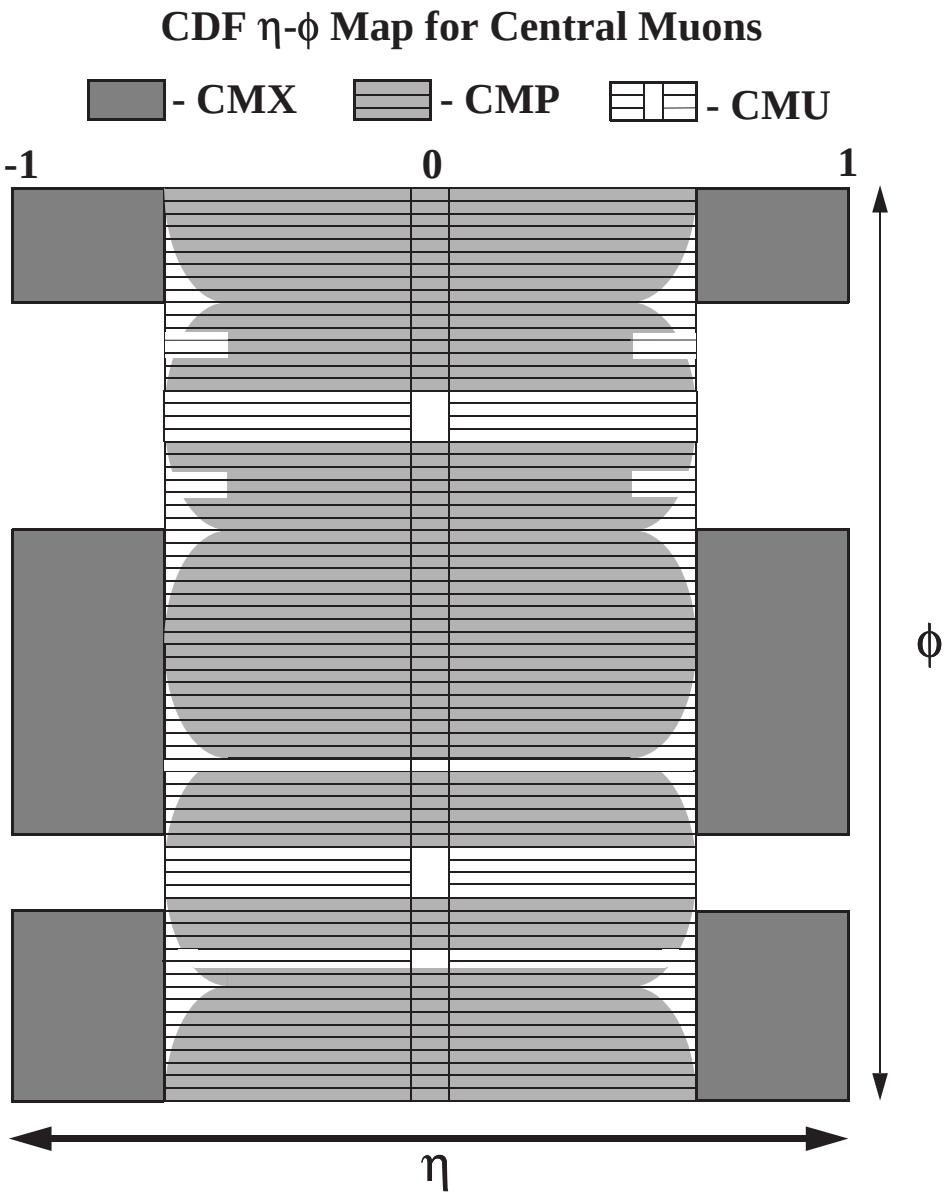

FIG. 20. The $\eta - \phi$ coverage of the CMU, CMP, and CMX.

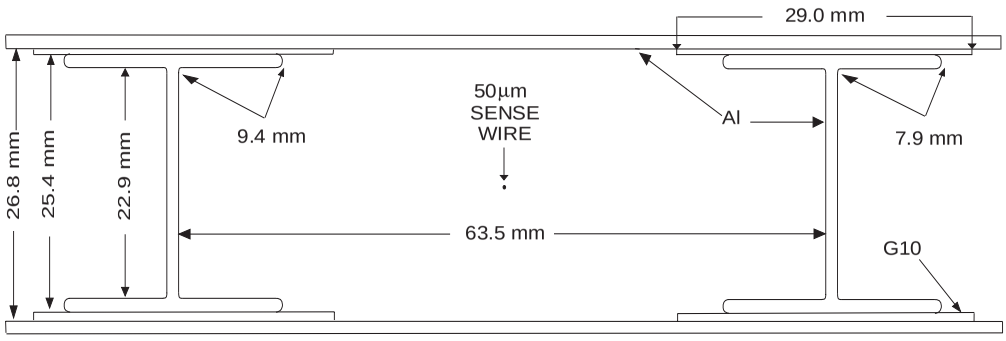

FIG. 21. A cell of the Central Muon chamber [35].

solid angle between $0.6 < |\eta| < 1.0$ is covered by the CMX. It is behind approximately 5 interaction lengths. The CMX has a 30° gap at the top of the detector (for the Main Ring and the solenoid refrigerator) and a 90° gap at the bottom where it intersects the floor.

E. **Luminosity Counters**

There is a plane of scintillation counters on the front face of the FEM. These scintillators, called the beam-beam counters (BBC), provide a "minimum-bias" trigger for the detector, and are also used as the primary luminosity monitor.

The luminosity is measured via :

$$\mathcal{L} = \frac{\frac{dN_{hits}}{dt}}{\sigma_{BBC}}. \tag{4.5}$$

where the cross-section, σ_{BBC}, is the $p\bar{p}$ total cross-section ($\simeq$ 50 mb at a center-of-mass energy of 1.8 TeV) and N_{hits} is the number of hits that are seen in coincidence

TABLE IV. Inclusive electron triggers.

Level	Run IA	Run IB
1	L1_CALORIMETER*	L1_CALORIMETER*
2	CEM_9_SEED_SH_7_CFT_9_2*	CEM_16_CFT_12*
		CEM_8_CFT_7_5_XCES*
3	ELE1_CEM_8_6*	ELEB_CEM_8_6*
	ELE1_CEM_9*	
	ELE1_CEM_15_10*	ELEB_CEM_18*

with the BBCs. Hence, one measures the amount of data recorded at CDF in inverse cross-section. Due to the uncertainty on the normalization of the BBCs, there is a 4.1% error on the measurement of the luminosity [36].

F. **Triggers**

The Run I Tevatron produced about 5 trillion collisions at a rate of 1 MHz. This rate must be reduced to about 5 Hz so that it can be recorded to tape. Hence, a three tiered system was designed to reduce this rate yet to allow us to record the events that are interesting to examine. The three tiers in the CDF trigger system are : level 1, level 2, and level 3. The level 1 and 2 trigger systems are discussed in detail in Ref. [37]. The level 3 trigger system is described in Ref. [38]. The inclusive electron and muon triggers relevant to this analysis are described in Tables IV and V, respectively.

1. **Level 1**

The level 1 trigger is a dedicated electronics which checks for deposited energy in calorimeter towers or muon chamber hits at or above some threshold to determine whether or not to save the event. The level 1 decision whether or not to accept this

TABLE V. Inclusive muon triggers.

Level	Run IA	Run IB
1	CMU_CMP_6PT0*	CMU_CMP_6PT0*
2	CMU_CMP_CFT_9_2*	CMUP_CFT_12_5DEG*
		CMUP_CFT_7_5_5DEG*
3	MUO1_CMU_CMP_7*	MUOB_CMU_CMP_8*
		MUOB_CMU_CMP_15*

event is made within 3.5 μs, the time between successive interactions, and is hence deadtimeless. The output rate is reduced to 1 kHz after this stage.

The level 1 electron trigger for Run I (L1_CALORIMETER*) is based on the energy deposition in $\Delta\eta \times \Delta\phi = 0.2 \times 15^{\circ}$ trigger towers. Electrons are identified as electromagnetic energy deposited in a calorimeter tower above 8 GeV threshold. The efficiency of the Run I level 1 trigger was determined to be 99.2 ± 0.1 % for electrons with transverse energy above 11 GeV [39].

The level 1 muon trigger for Run I (CMU_CMP_6PT0*) looked at two hits in each trigger tower [40]. A trigger tower comprised the four drift cells aligned along the radial direction subtending an angle of 4.2° in the central region of the detector. A p_{T} measurement was achieved by exploiting the fact that low momentum tracks emerge from the magnetic field at an angle with respect to the radial directions thereby producing hits on the radially aligned wires in the drift cells. A 6 GeV threshold was required for the Run I level 1 muon trigger. The efficiency of the high p_{T} trigger at the plateau is measured to be $93.1 \pm 1.1 \pm 1.0\%$, independent of the positive and negative charges [41].

2. **Level 2**

The level 2 trigger is also hardware. It is much more sophisticated than the level 1 trigger; and it manifests its sophistication by combining objects such as tracks, energy clusters, muon chamber hits, etc. in order to construct electrons, muons, etc. The level 2 trigger reduces the output rate to 12 Hz. If this rate is too high, the level 2 triggers are designed such that they can be prescaled.

At level 2, the online track finding for electrons and muons is performed by the central fast tracker (CFT) [42]. The CFT is a hardware track processor which uses fast timing information from the CTC as input. The CFT measures the curvature (p_{T}^{-1}) of tracks in the CTC. Hence, the momentum resolution of the CFT is determined to be $\frac{\delta p_{\mathrm{T}}}{p_{\mathrm{T}}^2} \simeq 0.035$. Eight sets of patterns ("bin") of curvature for tracks in CTC are provided by the CFT, which are used by the electron or muon trigger systems to select the track associated with an energy cluster in the central electromagnetic calorimeter or a track segment ("stub") in the central muon chambers. Each pattern is approximately 90% efficient for a track of the nominal p_{T}. The nominal values for Run IA and Run IB are summarized in Table VI.

TABLE VI. Summary of the CFT binning and its corresponding nominal value of track p_{T} (GeV/c) at at 90% efficiency.

Run	bin 0	bin 1	bin 2	bin 3	bin 4	bin 5	bin 6	bin 7
IA	3.0	3.7	4.8	6.0	9.2	13.0	16.7	25.0
IB	2.2	2.7	3.4	4.7	7.5	12.0	18.0	27.0

Run I used three different inclusive electron triggers. One electron trigger was used in Run IA. Two separate inclusive electron triggers (one with a low E_{T} threshold and another with a high E_{T} threshold) were used in Run IB.

The Run IA level 2 trigger required the presence of an electromagnetic energy cluster found in the CEM of at least 9 GeV with at least 9 GeV in the seed tower.

Neighboring towers above a 7 GeV threshold were included in the cluster. A requirement of a CFT track above a 9.2 GeV/c (CFT bin 4) threshold pointing to the same CEM wedge is also made. The hadronic energy in the cluster in the cluster was required to be less than 12.5% of the electromagnetic energy. The efficiency of the Run IA level 2 electron trigger is $(92.4 \pm 1.7\ ^{+3.0}_{-4.7})\%$ for electrons with transverse energy above 11 GeV [43].

The Run IB level 2 low E_{T} electron trigger prescribed an electromagnetic energy cluster in the CEM above an 8 GeV threshold in the seed tower. Electromagnetic energy deposited in neighboring towers in the CEM above 7 GeV threshold were also included in the cluster. A CFT track with a transverse momentum of at least 7.5 GeV/c (CFT bin 4) is required to point to the same CEM wedge. A match between the CFT track and the CES cluster position is made within $\pm$ 2.5 cm. The XCES trigger reduced the level 2 trigger rate by a factor of two while being 90% efficient for real electrons allowing the reduction in the E_{T} threshold from 9 GeV to 8 GeV. Again the hadronic energy in the cluster is demanded to be less than 12.5% of the electromagnetic energy. The level 2 low E_{T} electron trigger was dynamically prescaled as a function of instantaneous luminosity. The Run IB average prescale for this trigger was a factor of 1.2 [46]. The efficiency of the Run IB level 2 low E_{T} electron trigger including the isolation requirement for the trigger is $(91.4 \pm 1.1)\% \times (99.2 \pm 0.8)\%$ for electrons with transverse energy above 11 GeV [44].

The Run IB level 2 high E_{T} electron trigger prescribed an electromagnetic energy cluster in the CEM above a 12 GeV threshold in the seed tower. Electromagnetic energy deposited in neighboring towers in the CEM above 12 GeV threshold were also included in the cluster. A CFT track with a transverse momentum of at least 12 GeV/c (CFT bin 5) is required to point to the same CEM wedge. Again the hadronic energy in the cluster is demanded to be less than 12.5% of the electromagnetic energy.

The efficiency of the Run IB level 2 high E_{T} electron trigger is displayed in Fig. 22.

Run I used three different inclusive muon triggers. One muon trigger was used in Run IA. Two separate inclusive muon triggers (one with a low p_{T} threshold and another with a high p_{T} threshold) were used in Run IB. The CMU consists of 24 wedges with 6 muon towers per wedge. Each two consecutive muon chambers in the CMU are logically connected to become CMU trigger towers; each CMU trigger tower covers 5 degrees in azimuth. The muon chamber information, matching map, and tracking information are stored in the track list board (TRL) which is retrieved in software via TRLMAP. The level 2 high p_{T} triggers require the level 1 high p_{T} muon trigger and at least one cluster in the CMP chamber associated with a CFT bin 5 track. It also requires that the extrapolated position of the CFT track to the CMU muon detector be within the CMU muon module ("muon trigger tower"; 4.2° in φ and ± 0.6 in η) that has the muon stub ("5-degree matching"). This is also an allowance for multiple scattering, so that the CFT track is accepted if its extrapolated position would be within two muon chambers. The matching is performed by a map on the track list board (TRL) after a looser match from the CTCX extrapolation map. The level 2 high p_{T} triggers did not need to be dynamically prescaled. The low p_{T} muon trigger is similar to the high p_{T}, but requires a CFT bin 4 track. The Run IB low p_{T} muon trigger was dynamically prescaled by a factor of 1.8 [47].

The Run IA muon trigger efficiency (CMU_CMP_CFT_9_2*) is $92.9 \pm 1.5\%$ relative to the level 1 muon trigger for muons with transverse momentum above 11 GeV/c [49]. The Run IB muon trigger efficiencies are determined as functions of inverse momentum (curvature) relative to the CFT bin 0 trigger in Fig. 23. The CFT bin 0 efficiency was determined to be $0.9481 \pm 0.0017 \pm 0.0077$ (μ^+) and $0.93399 \pm 0.0018 \pm 0.0080$ (μ^-)[48].

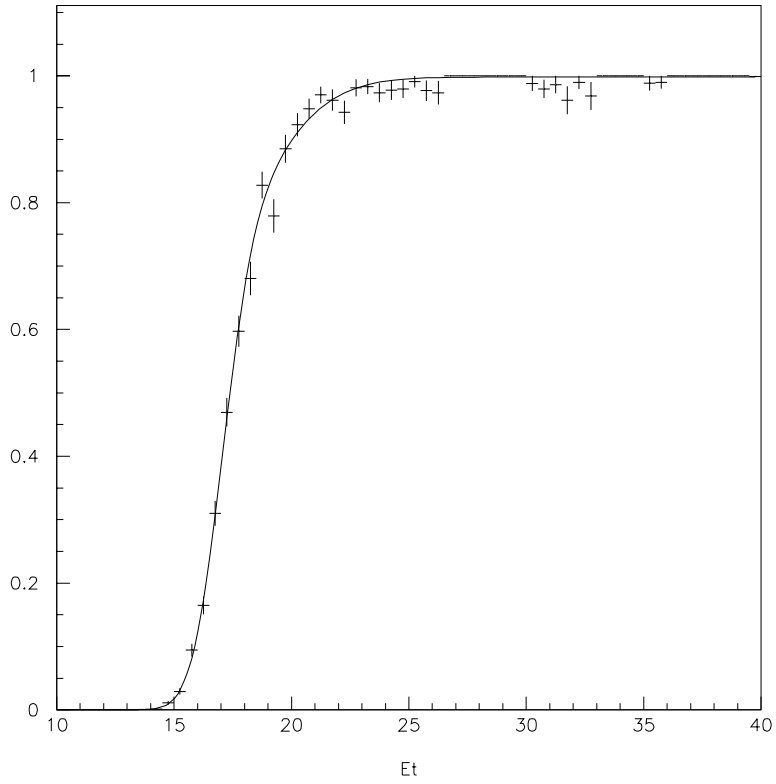

FIG. 22. CEM_16_CFT_12* efficiency as a function of transverse energy of the electron. Taken from Ref. [45].

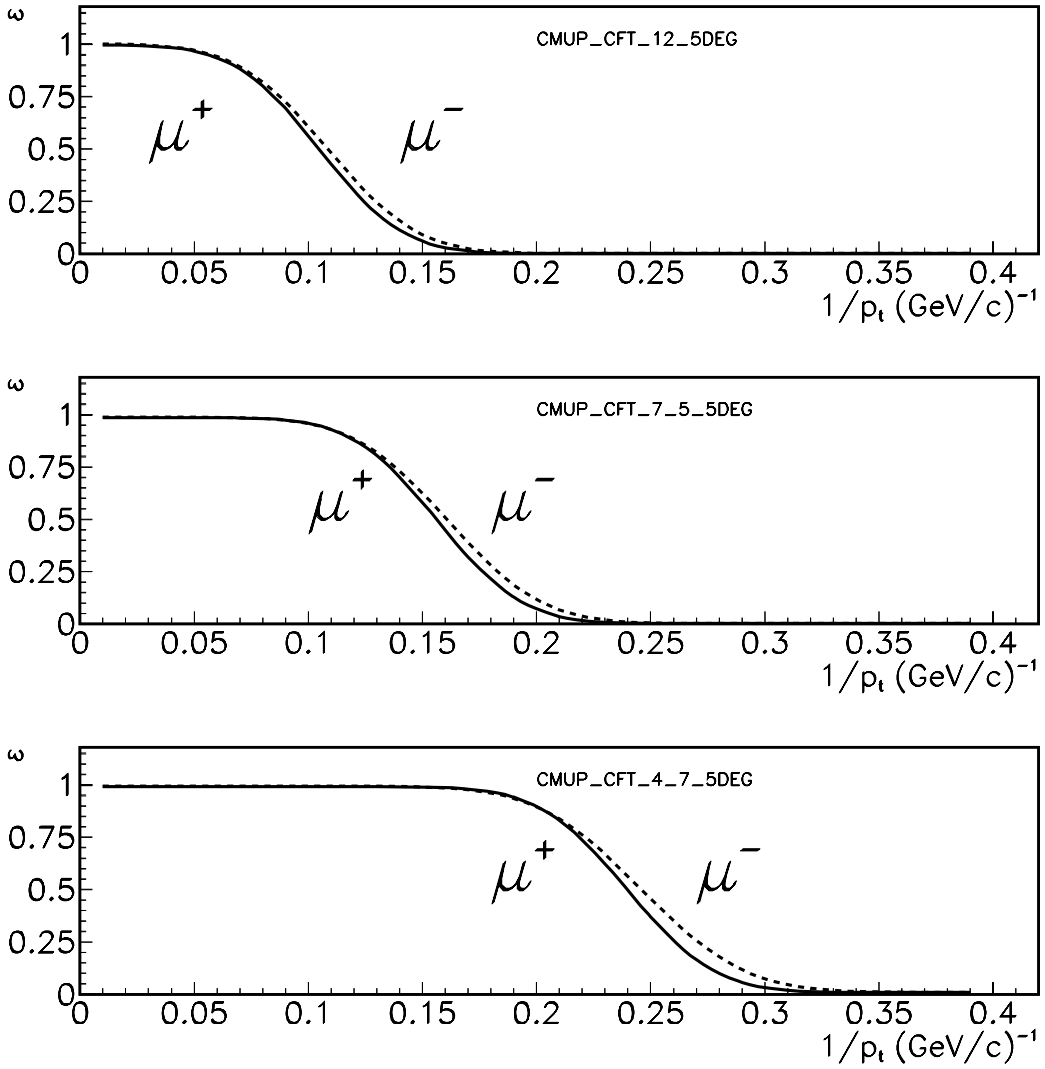

FIG. 23. Run IB level 2 muon trigger efficiency curves fitted for positive and negative muons relative to CFT bin 0 trigger [48]. These efficiencies are plotted as functions of inverse transverse momentum of the muon since the triggers select muons based on curvature rather than momentum. Taken from Ref. [50].

3. Level 3

The level 3 trigger is a software filter that reconstructs the entire event which is run on 4 Silicon Graphics 8-CPU Power Servers with a combined processing power of a gigaflop [38]. The purpose of the level 3 trigger is to reduce the rate to 5 Hz so that it can be recorded to 8 mm tape. The level 3 exotic dilepton trigger, which accepts dilepton events online in this analysis, requires 2 leptons and a level 2 accept.

The level 3 electron trigger required an event with a good electron from level 2 to pass. In Run IA, it was determined that electrons having transverse energy above 11 GeV have an efficiency of $95.2 \pm 1.5\%$ at the plateau [51]. This result was confirmed for the level 3 electron trigger implemented in Run IB [52].

The level 3 muon trigger required an event with a good muon from level 2 above threshold to pass. In Run IA, the threshold was set at 7 GeV. For Run IB, this threshold was increased to 8 GeV. In Run IA, it was determined that this trigger possesses a plateau efficiency of $99.3 \pm 0.1 \pm 1.0$ % for muons with transverse momentum above above 11 GeV/c [53]. This result was confirmed for the level 3 muon trigger implemented in Run IB for muons with transverse momentum above 11 GeV/c [52].

G. Detector Simulation

The CDF collaboration uses a Monte Carlo package called QFL$'$ to generate effects of the detector response [54]. Its output is based on parameterized results from testbeam rather than calculation from first principles as in GEANT based detector simulations [55]. All simulated events used in this analysis were generated with QFL$'$.

CHAPTER V

DATA SAMPLES

A. **Introduction**

In order to search for Supersymmetry in the dilepton+jets channel, dilepton and dilepton-dijet data samples must be created. These data samples are the SUSY dilepton and the SUSY dilepton-dijet datasets. The selection of these samples are accomplished via electron, muon, and jet identification cuts which are defined in this chapter. Validation of these samples is done by comparison to the $Z^0 \to \ell\ell$ and top dilepton analyses.

B. **The Run I SUSY Dilepton Sample**

The Run I SUSY Dilepton Dataset is composed of the Run IA and Run IB SUSY Dilepton Datasets. The data selection requires that there are at least two leptons with one lepton passing a tight cut and a second passing a loose cut. The first lepton is required to be found in either the central electromagnetic calorimeter (CEM) or in the central muon chambers (CMU or CMP; CMUP represents a muon whose track crosses both the CMU and CMP). The second lepton can be an object found in the above mentioned regions, the plug electromagnetic calorimeter (PEM), the central muon chamber extension (CMX), or a track above 10 GeV/c which leaves minimum ionization in the central calorimeter (CMIO).

In Run IA, the dilepton dataset was composed from the Run IA inclusive electron and muon streams and vetoed duplicate events. The Run IA inclusive electron and muon streams consisted of 3.7 million events and 2.7 million events, respectively. The Run IA dilepton sample is composed of 58,221 dilepton events [56]. In this selection,

at least one central lepton must have momentum above $\simeq$ 9 GeV/c and a second lepton with its momentum above $\simeq$ 3 GeV/c.

In Run IB, the exotic dilepton dataset (XDLB_5P Stream B dataset) was created using the level 3 Exotic Dilepton Trigger (COMBINED_EXOB_DIL) which selected any dilepton (ee, $e\mu$, and $\mu\mu$) event that was passed from level 2 and satisfied the TDLFLT (CDF top dilepton filter) criteria. The Exotic Dilepton Dataset consists of 3,270,488 events. The Run IB sample is composed of 457,478 events that were selected from the Exotic Dilepton Sample to tape. In the Run IB selection, at least one central lepton must have momentum above $\simeq$ 8 GeV/c and a second lepton must have its momentum above $\simeq$ 3 GeV/c.

In selecting this sample, one must ensure that the leptons selected pass certain quality cuts. These cuts are qualified and quantified based on testbeam data. The following subsections discuss the electron and muon identification cuts used in the selection of the SUSY Dilepton Sample. Kinematic variables from this sample are discussed in one of these latter subsections as well.

1. Electron Cuts

Three sets of identification cuts are defined for electrons: tight (TCE), loose (LCE), and plug (PEM). The cuts are made based on the following information: finding of a charged track pointing to the electromagnetic cluster (E/p for CEM or VTX occupancy for PEM), ratio of hadronic to electromagnetic energy deposited in the calorimeter ($\frac{Had}{Em}$), transverse shower profile (L_{shr} for CEM and $\chi^2_{3\times3}$ for PEM), extrapolated track-shower position matching ($\mid \Delta x \mid$ and $\mid \Delta z \mid$), and strip chamber shower shape (χ^2_{strip}). The description for each variable is given in the following subsections. The specified values of the cuts used in the SUSY Dilepton Sample are listed in Table VII. The distributions of the variables for tight (TCE), loose (LCE), and

TABLE VII. Lepton identification cuts applied to the SUSY dilepton sample.

Object type	Cut	Tight Cut	Loose Cut
CEM	$E_{\rm T}^{raw}$	$\geq$ 8.0 GeV	$\geq$ 4.0 GeV
	$p_{\rm T}^{raw}$	$\geq$ 4.0 GeV/c	$\geq$ 2.8 GeV/c
	E^{raw}/p^{raw}	$\leq$ 2.0	$\leq$ 2.0
	$\frac{Had}{Em}$	$\leq$ 0.05	$\leq$ 0.055+0.045(E/100)
	L_{shr}	$\leq$ 0.2	$\leq$ 0.2
	$\mid \Delta x \mid$	$\leq$ 3.0 cm	$\leq$ 3.0 cm
	$\mid \Delta z \mid$	$\leq$ 5.0 cm	$\leq$ 5.0 cm
	χ^2_{strip}	$\leq$ 10.0	$\leq$ 15.0
PEM	$E_{\rm T}^{raw}$		$\geq$ 4.0 GeV
	$\frac{Had}{Em}$		$\leq$ 0.1
	$\chi^2_{3\times3}$		$\leq$ 3.0
	VTX Occ.		$\geq$ 0.5

plug (PEM) electrons in the SUSY dilepton data sample are shown in Figs. 24, 25, and 26, respectively.

a. **Charged Track Requirement**

For central electrons, the ratio of the electromagnetic energy, E, of the electron cluster measured in the calorimeter to the electron's momentum, p, measured in the CTC is required to be less than 2. By requiring the presence of a charged track, electron candidates can be separated from photons (especially those from π^0 decays) in the central electromagnetic calorimeter.

Since the CTC tracking volume does not cover the plug region, a CTC track requirement can not be used adequately for identification. To test the presence of charged tracks pointing towards the PEM cluster, a hit occupancy in the vertex chamber (VTX) of that octant along a possible electron path is used. The VTX occupancy is defined to be the ratio of layers in the VTX on which the electron deposits charge divided by the expected number of layers in the VTX to be traversed

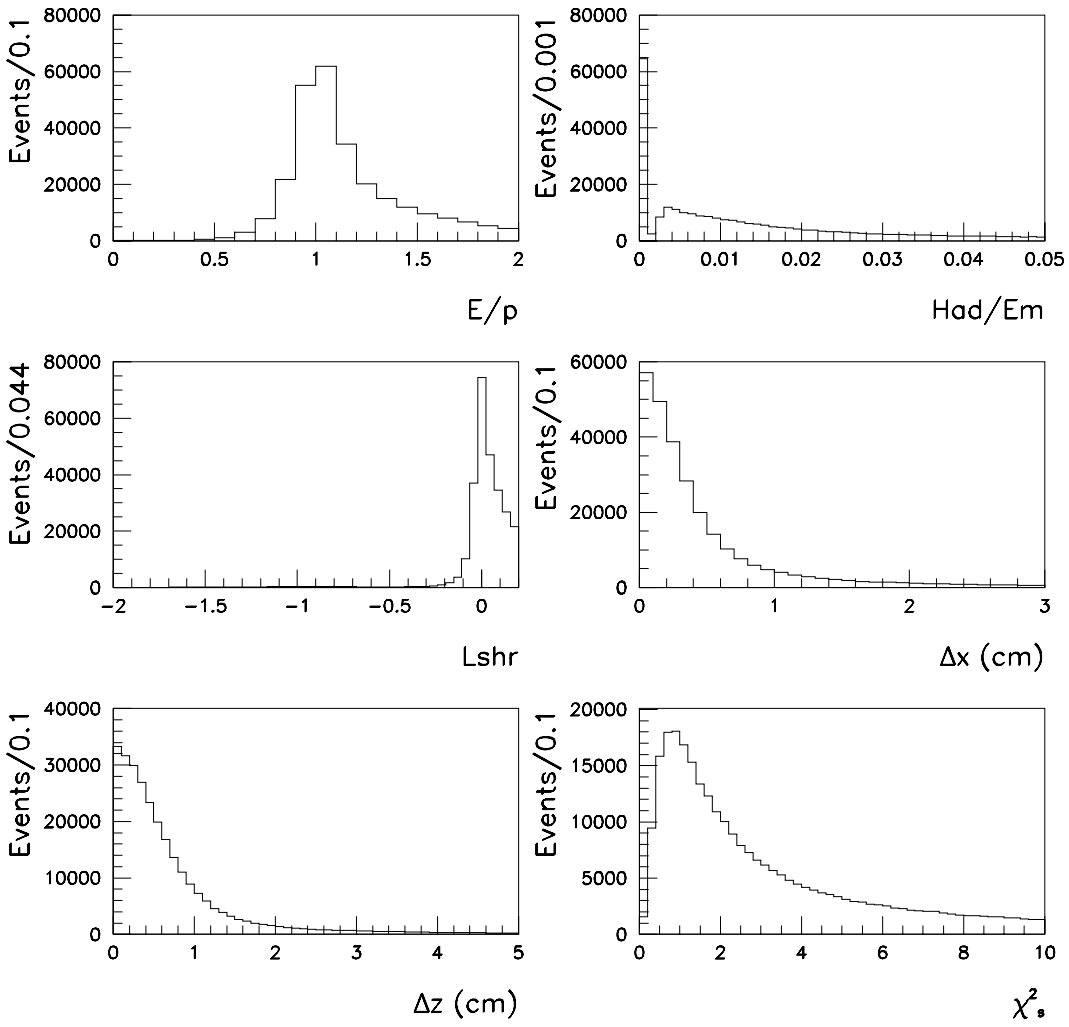

FIG. 24. Distributions of the variables used for identification for objects that are recognized as tight CEM electrons.

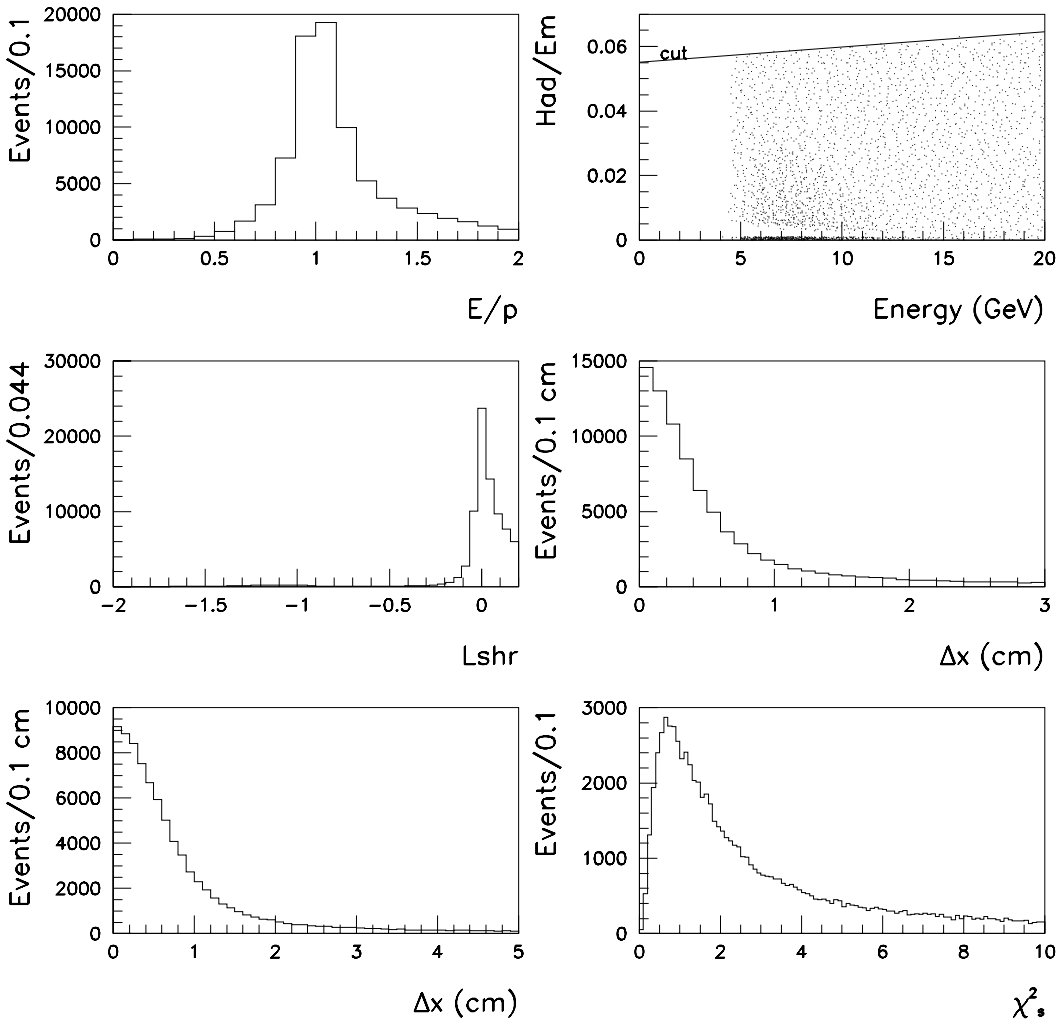

FIG. 25. Distributions of the variables used for identification for electrons that pass the loose CEM criteria.

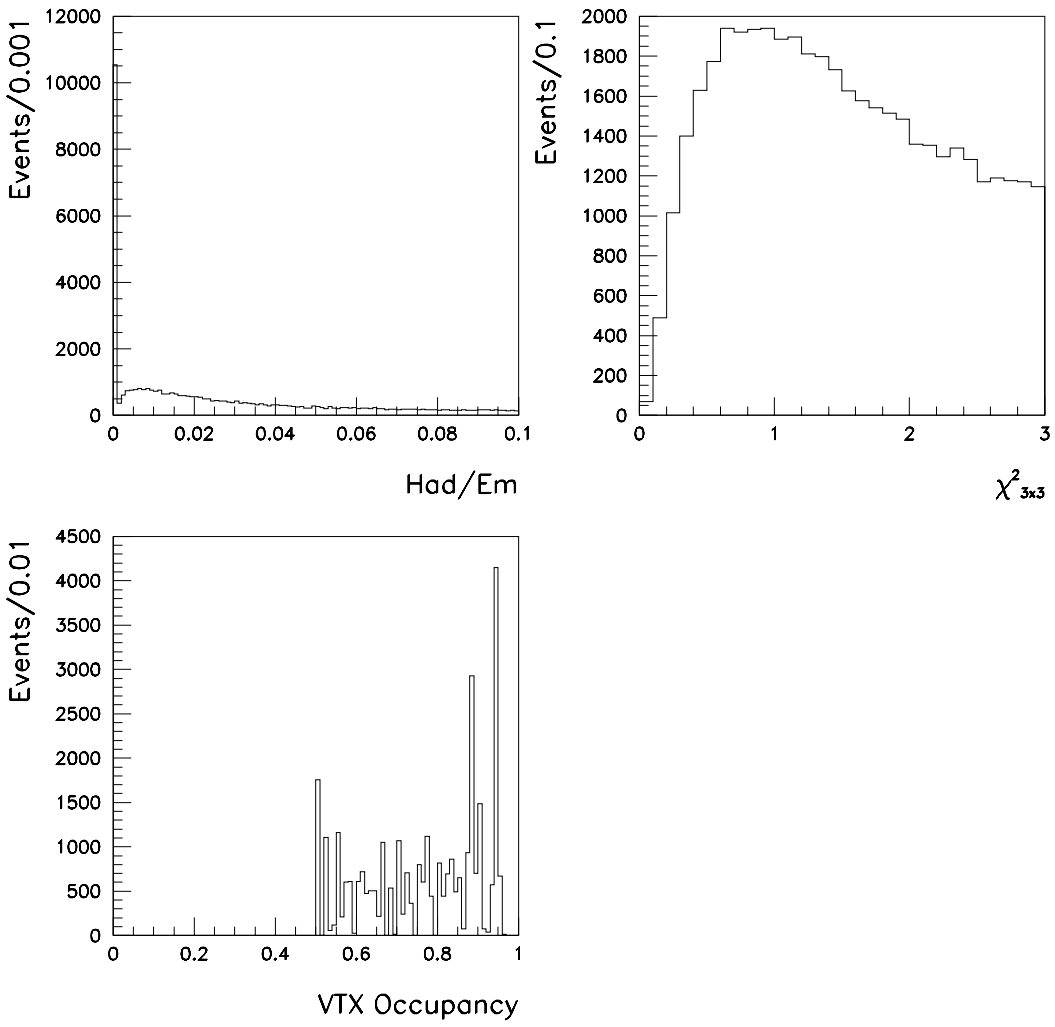

FIG. 26. Distributions of the variables used for identification for electrons that satisfy the PEM criteria.

by the electron.

b. Energy Leakage into Hadron Calorimeters

A small value of the ratio Had/Em of the energy in the hadronic towers to the energy in the electromagnetic towers in the calorimeter cluster is used to discriminate against jets which have a high electromagnetic fraction.

c. Electron Lateral Shower Profile

The transverse profile, or "L_{shr}," of a central electron allows a comparison of the lateral sharing of the energy in the calorimeter towers of an electron cluster to electron shower shapes from test beam data. The variable L_{shr} is defined as:

$$L_{shr} \equiv 0.14 \sum_i \frac{E_i^{adj} - E_i^{prob}}{\sqrt{(0.14\sqrt{E})^2 + (\Delta E_i^{prob})^2}} \tag{5.1}$$

where E_i^{adj} is the measured energy in a tower adjacent to the seed tower, E_i^{prob} is expected energy in the seed tower, $0.14\sqrt{E}$ represents the energy resolution of the calorimeter, and ΔE_i^{prob} is the uncertainty on the expected energy in the seed tower. Note that E_i^{prob} is determined from test beam data.

For plug electrons, a variable denoted $\chi^2_{3\times3}$ measures the deviation of the shower from the predicted shower shape from test beam data by using 3×3 array of the plug electromagnetic calorimeter towers.

d. Track-Shower Matching Variables

The track pointing to a central electron cluster is extrapolated to the CES chamber. The CES chamber, embedded 6 radiation lengths into the CEM, can be used to

observe the lateral profile of an electromagnetic shower at its maximum. The extrapolated position is then compared to the shower position as measured in the CES. Δx is the separation in the $r - \phi$ view between the extrapolated track position and the CES strip cluster position. Δz is the corresponding separation in the z-view.

e. **Pulse Height Shape in Strip Chambers**

The CES pulse height shape is used for electron identification in the central region of the detector. An electromagnetic shower in the calorimeters begins much earlier for an electron than for a hadron. It is compared to test beam data using a χ^2 test. χ^2_{strip} is a quality of the fit of the energy deposited on each of the 11 CES z-strips compared to the test beam shape.

2. Muon Cuts

Four sets of lepton identification classes for central muons are used : tight (TCM), loose (LCM), CMX, and CMIO (see Table VIII). The cuts in each class are based on the following information: calorimeter energy (EM and Had), impact parameter of the associated track (d_0), and a track matching cut ($\mid \Delta x \mid$ or χ^2_x). Description of the variables are given in the following sections. The distributions of the identifying variables for tight, loose, CMX, and CMIO muons are given in Figs. 27, 28, 29, and 30, respectively.

a. **Calorimeter Energy**

Since the muon chambers lie outside the calorimetry, hits in the muon chambers are expected from energetic hadronic jets. Since the muon is a minimum ionizing particle, there are limits on the amount of electromagnetic (EM) and hadronic (Had) energy that can be deposited into a calorimeter tower projected before a muon chamber. The

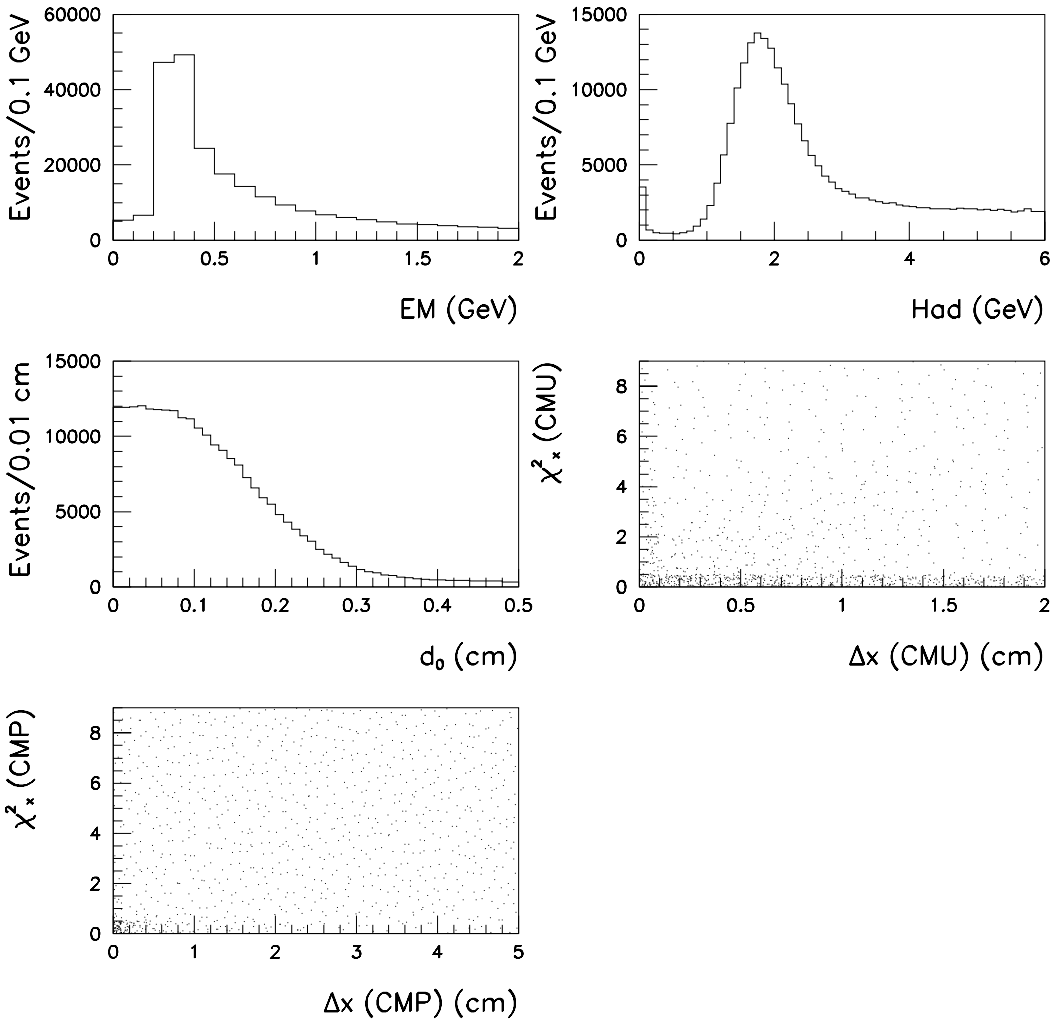

FIG. 27. Distributions of the variables used for identification for physics objects that pass the tight CMU/CMP/CMUP criteria.

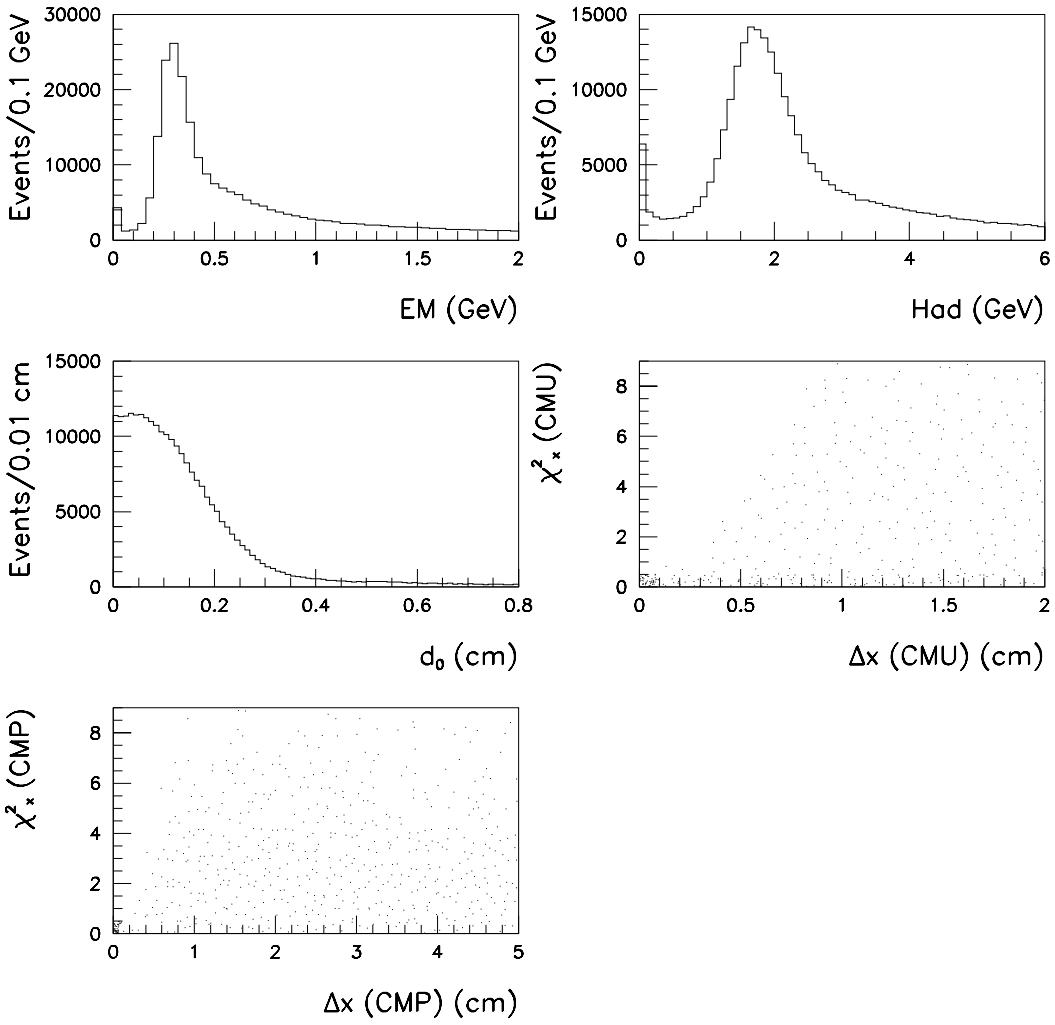

FIG. 28. Distributions of the variables used for identification for objects that pass the loose CMU/CMP/CMUP criteria.

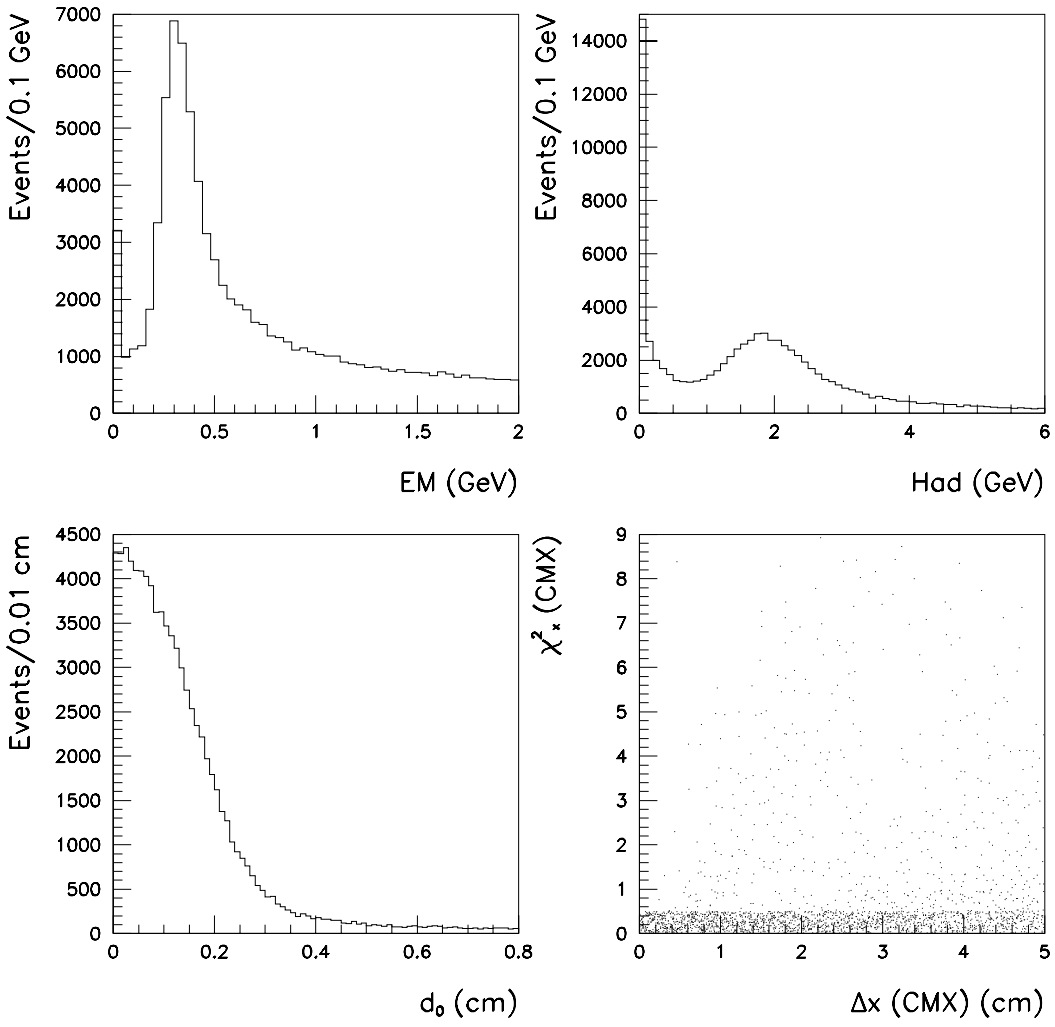

FIG. 29. Distributions of the variables used for identification for objects recognized as CMX muons.

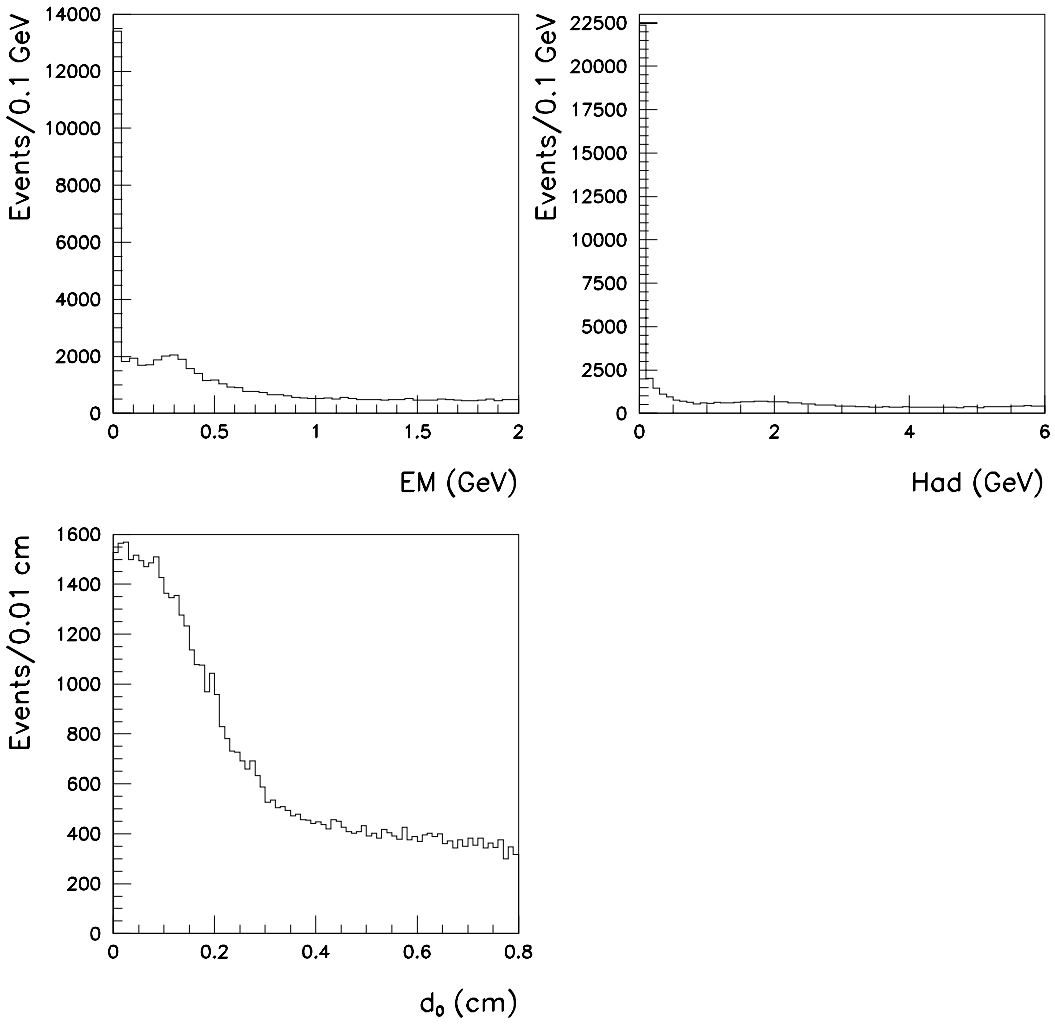

FIG. 30. Distributions of the variables used for identification for objects recognized as CMIO muons.

TABLE VIII. Muon identification cuts applied to the SUSY dilepton sample.

Object type	Cut	Tight Cut	Loose Cut
	p_{T}^{raw}	$\geq$ 7.5 GeV/c	$\geq$ 1.4 GeV/c
	EM	$\leq$ 2.0 GeV	$\leq$ 2.0 GeV
	Had	$\leq$ 6.0 GeV	$\leq$ 6.0 GeV
CMU/CMP/CMUP	CMU $\mid \Delta x \mid$ or χ^2_x	$\leq$ 2.0 cm or $\leq$ 9.0	$\leq$ 2.0 cm or $\leq$ 9.0
	CMP $\mid \Delta x \mid$ or χ^2_x	$\leq$ 5.0 cm or $\leq$ 9.0	$\leq$ 5.0 cm or $\leq$ 9.0
	$\mid d_0 \mid$ (raw)	$\leq$ 0.5 cm	$\leq$ 0.8 cm
	p_{T}^{raw}		$\geq$ 1.4 GeV/c
	EM		$\leq$ 2.0 GeV
CMX	Had		$\leq$ 6.0 GeV
	CMX $\mid \Delta x \mid$ or χ^2_x		$\leq$ 5.0 cm or $\leq$ 9.0
	$\mid d_0 \mid$ (raw)		$\leq$ 0.8 cm
	p_{T}^{raw}		$\geq$ 10.0 GeV/c
CMIO	EM		$\leq$ 2.0 GeV
	Had		$\leq$ 6.0 GeV
	$\mid d_0 \mid$ (raw)		$\leq$ 0.8 cm

mean electromagnetic and hadronic energies for a typical muon are 0.3 and 2 GeV, respectively.

b. **Impact Parameter**

The impact parameter, d_0, is the distance of closest approach between the reconstructed muon track and the beam axis in the $r-\phi$ plane. The cuts are designed to exclude muons which originate from decays-in-flight and cosmic rays.

c. **Track Matching**

In order to determine the correct track associated with a hit in the muon chambers, a muon candidate is required to satisfy a matching cut: χ^2_x or Δx. χ^2_x represents the quality of the fit for the extrapolated CTC track to the muon stub. Δx is the difference in $r-\phi$ between the extrapolated position in the muon chambers of the CTC track and the muon hit. A muon is required to pass at least one of these cuts.

3. Kinematics

The transverse energies (momenta) of electrons (muons) were examined after cuts. Azimuthal angle (ϕ) and pseudorapidity (η) of the leptons have been checked as well. These kinematic distributions of the leptons can be found in Figs. 31 and 32.

Figure 31 displays the transverse energy distributions of the first and second electron. The pseudorapidity displays show where central and plug electrons are expected to be found in the detector. The dip at $\eta = 0$ is due to the gap where the west and east part of the CDF calorimeter meet. Since the calorimeter is uniform in azimuthal angle, the plots of azimuthal angle of the electromagnetic energy clusters are as well.

Figure 32 displays the transverse momentum distributions of the first and second muon. The pseudorapidity displays show where CMU/CMP/CMUP, CMX, and CMIO muons are expected to be found in the detector. The dip at $\eta = 0$ is due to the gap where the west and east part of the CDF detector meet. Since the CMU and CMP are uniform in azimuthal angle, the plots of azimuthal angle of the muon tracks associated with CMU/CMP/CMUP are as well. Tracks associated with minimum ionization in the calorimeter (CMIO) are flat in ϕ. The azimuthal angle of the tracks associated with hits in the CMX display gaps where there is no coverage.

C. Stage-1: Isolated Dilepton Sample

In order to study dilepton events of good quality, isolation cuts are imposed on the dilepton sample. The calorimeter isolation ($ISO^{cal}_{0.4}$) is determined by summing the transverse energy deposited in the calorimeter in a cone in η-ϕ space of $\Delta R = \sqrt{(\Delta\eta)^2 + (\Delta\phi)^2} = 0.4$ around the lepton subtracting the transverse energy of

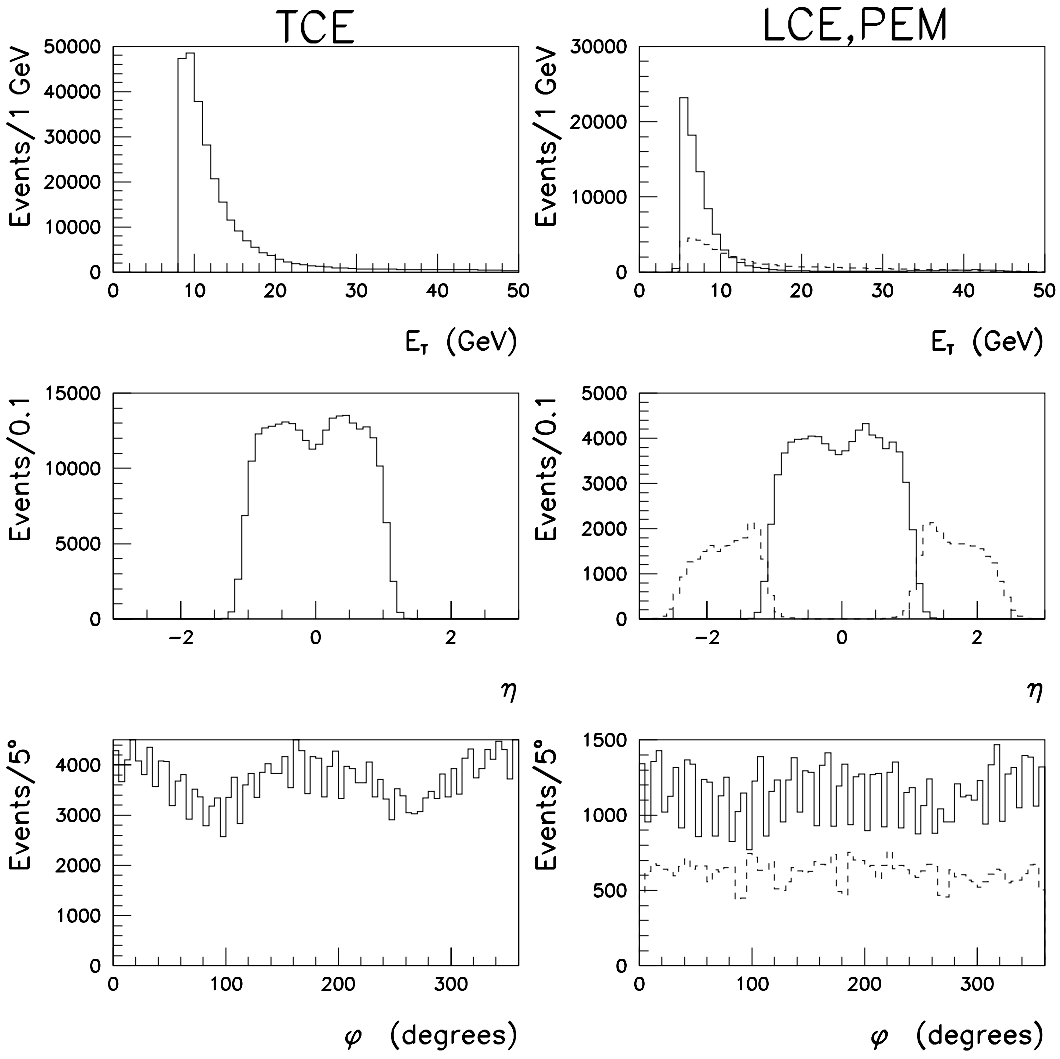

FIG. 31. Distributions of the kinematic variables for physics objects that pass the CEM (TCE and LCE) (solid) and PEM (dashed) identification criteria.

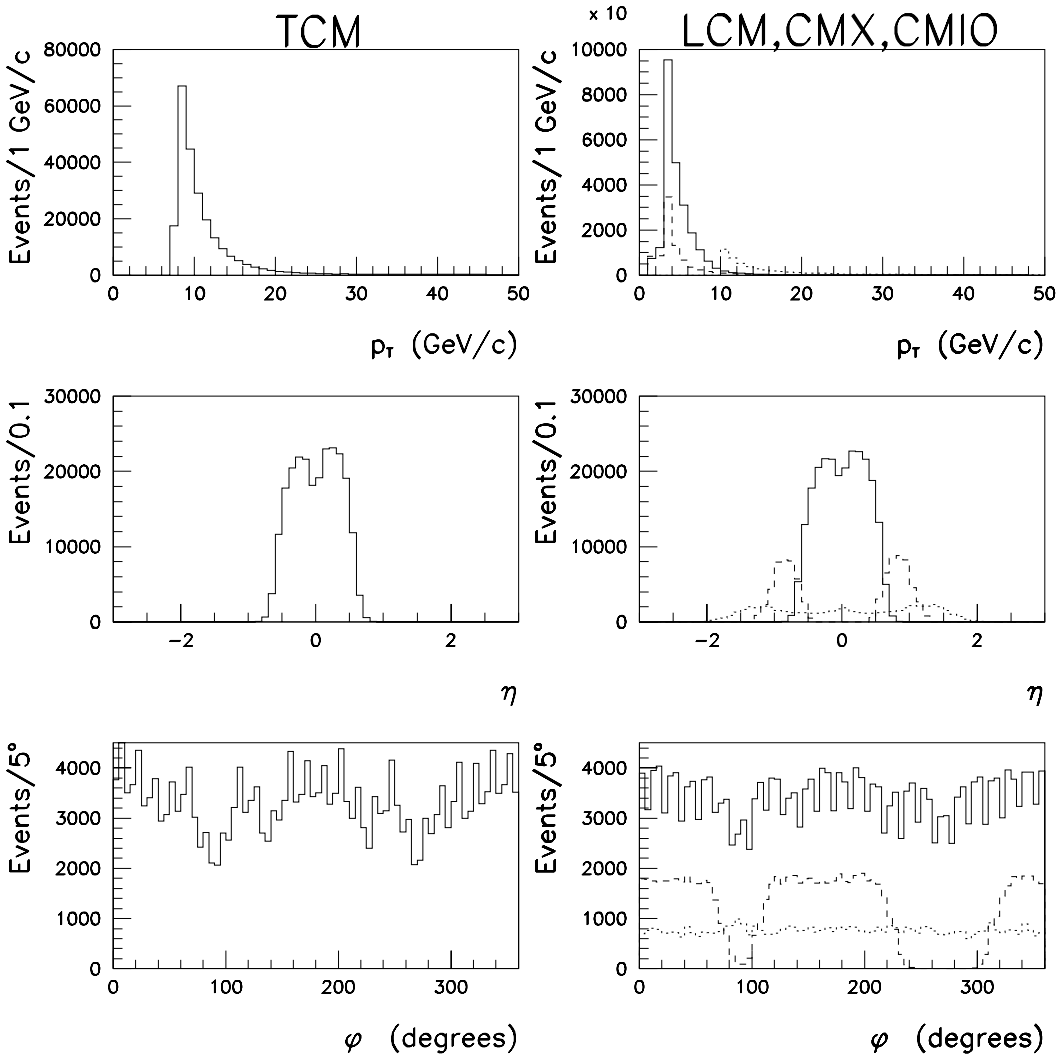

FIG. 32. Distributions of the kinematic variables for physics objects that pass the CMU/CMP/CMUP (TCM and LCM) (solid), CMX (dashed), and CMIO (dotted) identification criteria.

the lepton:

$$ISO_{0.4}^{cal} = \sum_{\Delta R<0.4} E_{\rm T} - E_{\rm T}(\ell)$$

In this stage of data selection, it is required that at least two isolated ($ISO_{0.4}^{cal} \leq 4$ GeV) lepton candidates pass the lepton quality cuts (see Tables VII and VIII) where at least one tight lepton (CEM or CMU/CMP/CMUP) with $E_{\rm T}^{raw}(e) \geq 8$ GeV or $p_{\rm T}^{raw}(\mu) \geq 7.5$ GeV/c; and a second lepton (CEM, PEM, CMU/CMP/CMUP, CMX, CMIO) pass loose-quality cuts with $p_{\rm T}^{raw}(\mu) \geq 2.8$ GeV/c (≥ 10 GeV/c for CMIO muons) or $E_{\rm T}^{raw}(e) \geq 4$ GeV.

After imposing these criteria, there are **20,349** events and **143,305** events from Run IA and IB, respectively. Note that a cut on charge significance for leptons (CEM, PEM, CMU/CMP/CMUP, CMX, and CMIO) is applied only for the Run IA data sample. The efficiencies for the lepton identification and isolation cuts are studied in Appendices B and C. The distributions of calorimeter isolation for electrons and muons are shown in Figs. 33 and 34. The distributions of the isolation show that there are many events where a lepton is isolated. Note that the isolation associated with plug electrons is shifted to higher values than the central electrons because the plug calorimeter receives deposited energies from many lower $p_{\rm T}$ particles which follow the magnetic field lines. Since muons found in the CMX are at a slightly higher pseudorapidity range than those found in the CMU or CMP, a shift to higher isolation values is also seen.

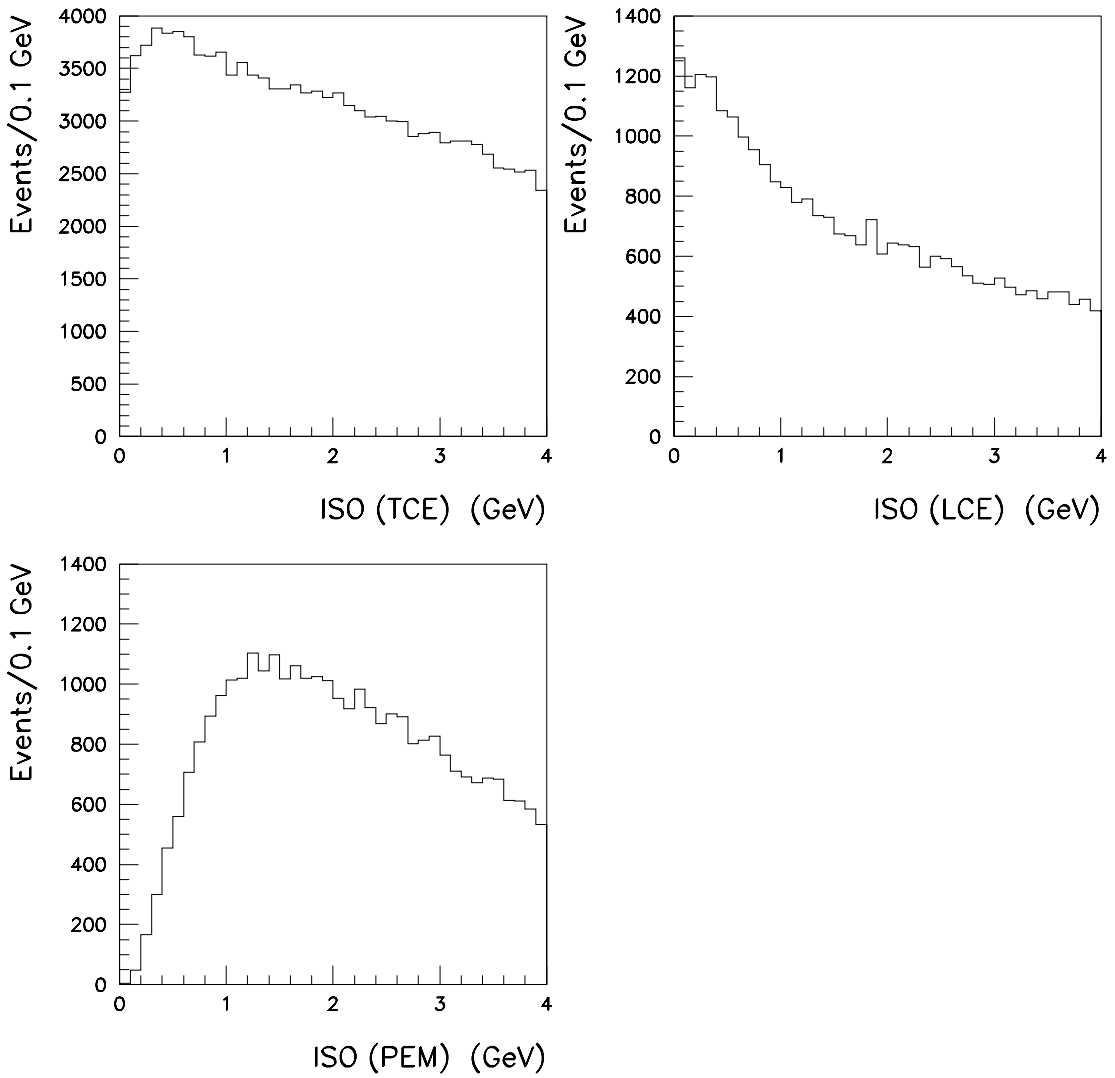

FIG. 33. Calorimeter isolation in $\Delta R = 0.4$ for the three electron classifications.

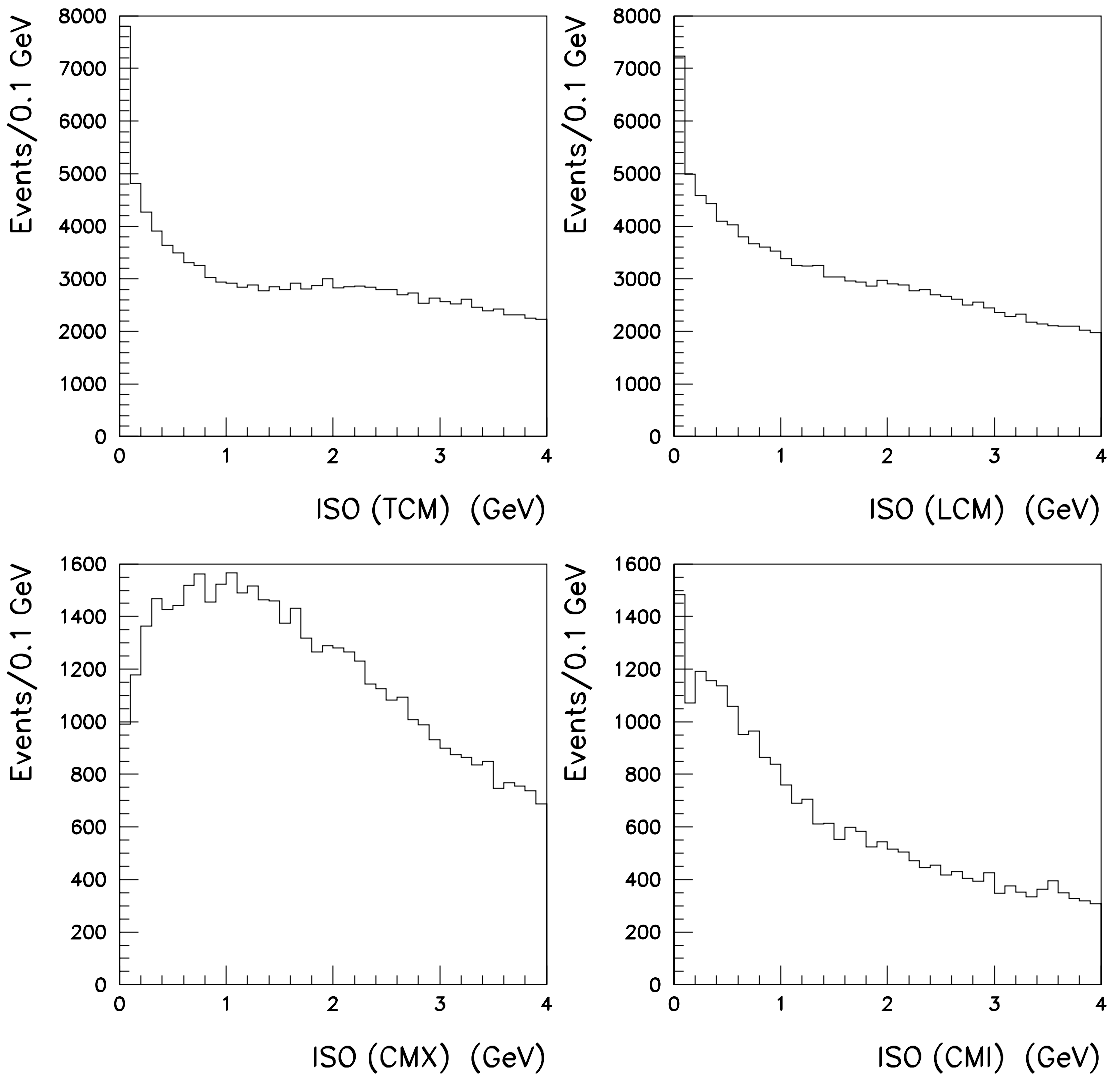

FIG. 34. Calorimeter isolation in $\Delta R = 0.4$ for the four muon classifications.

D. SUSY Dilepton Dijet Sample

1. Stage-2: Isolated Dilepton Dijet (uncorrected $E_{\rm T}$) Sample

In the second stage of the selection, there are at least two jets within $\mid \eta_{det} \mid \ \leq 2.4$, each having $E_{\rm T}^{raw} \geq 10$ GeV. Jets are clustered with a cone of $\Delta R_j^{cone} = 0.4$. There is a Run IA sample of **4,604** events and a Run IB sample of **33,100** events.

2. Stage-3: Isolated Dilepton Dijet (corrected $E_{\rm T}$) Sample

At this stage of the data selection, two isolated ($ISO_{0.4}^{cal} \leq 4$ GeV) leptons are required with one tight lepton having momentum above 11 GeV/c and the other lepton to have momenta above 5 GeV/c . The electromagnetic energy scale must be corrected for run dependence and local variations in the calorimetry. Therefore, these corrections to the calorimeter energy scale are provided (via ELCR92) for central (CEM) and plug (PEM) electrons. After reconstruction of the event, it is necessary to provide a beam-constrained fit (TRKSVC) for tracks that are associated with muons to provide accurate measurement of their momenta. This selection requires that there are at least two jets with corrected $E_{\rm T} \ \geq \ 15$ GeV based on jet cone size $\Delta R_j^{cone} = 0.4$. These jet corrections incorporate absolute and relative corrections as well as out-of-cone corrections and estimations for the underlying event (see Appendix D for details). Electron and jet separation is required to prevent counting electrons as jets ($\Delta R(e,j) \geq 0.4$).

A summary of cuts is given in Table IX. Note that there is no cut on $\Delta R(\mu, j)$ in this stage. With these requirements, there are **229** and **1,487** events from Run IA and IB, respectively, for jets with $\Delta R_j^{cone} = 0.4$. The cumulative number of events after each cut in this analysis is summarized in Table X. Note that the opposite-sign (OS) $\mu\mu$ event (Run/Event = 47311/71056) found in the Run IA SUSY dilepton

analysis is also found in the Stage-3 sample[56].

Note that the ratio of the number of events in the Run IA data to those in the Run IB data in the Stage-3 sample is not close to the ratio (= 0.213) of the luminosities of the two data samples. The difference can be explained by the fact that the Run IB sample is created from the level 3 exotic dilepton trigger which accepts events passing level 2 inclusive lepton or dilepton triggers, while the Run IA sample is from the inclusive lepton triggers. Therefore, a large number of $J/\psi \to \ell^+\ell^-$ and $\Upsilon \to \ell^+\ell^-$ events are still left in the Run IB data sample in this stage as seen in Fig. 35. The Z^0, Υ, and J/ψ peaks are clearly seen for the ee and $\mu\mu$ channels. Also, one can see that the $J/\psi \to \mu^+\mu^-$ distribution is much more pronounced than in the $J/\psi \to e^+e^-$ channel due to the $ISO^{cal}_{0.4}$ cut and the better tracking resolution at low $p_{\rm T}(\mu)$ compared to the energy resolution for electrons.

E. Comparison with Other Analyses

To validate the Stage-1 and Stage-3 SUSY dilepton samples, the number of Z^0 and top dilepton events in the samples are compared to the results from the CDF standard analyses.

1. Z^0 Events

The number of Z^0 event candidates in Stage-1 and Stage-3 samples are examined using cuts in addition to those stated in Tables VII and VIII are described in Tables XI and XII. Jets are counted with $\Delta R(\ell, j) > 0.4$. The results, including a comparison with the previous CDF analyses are summarized in Table XIII [57, 58, 59].

There is a good agreement between the number of $Z^0 \to$ CEM-CEM and $\mu\mu$ events in the different analyses and also between different data samples. A significant

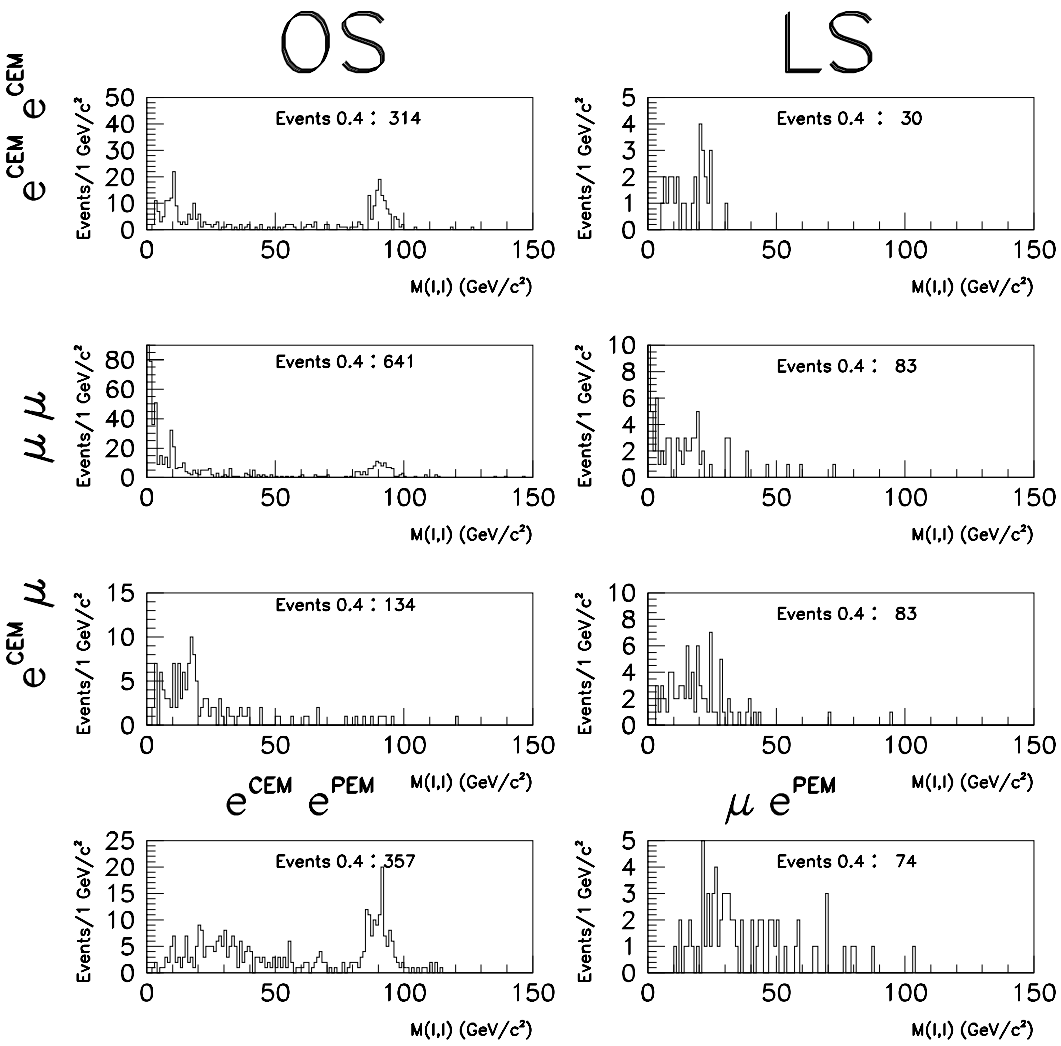

FIG. 35. Dilepton mass spectra in the Stage-3 sample for $\Delta R_j^{cone} = 0.4$. The Z^0 and Υ peaks are clearly seen for the ee and $\mu\mu$ channels. The J/$\psi \rightarrow \mu^+\mu^-$ events are also obvious. The J/$\psi \rightarrow e^+e^-$ events have been removed by the isolation requirements.

TABLE IX. $E_{\rm T}$ and $p_{\rm T}$ cuts for leptons and jets in the Stage-3 dilepton dijet sample. Lepton $E_{\rm T}$ and $p_{\rm T}$ values are corrected values. Additional lepton identification cuts applied to the Stage-1 cuts are listed. A good CTC track is defined to be a 3D track with $\geq$ 3 axial superlayer hits, $\geq$ 2 stereo superlayer hits, and $\geq$ 6 total superlayer hits in the CTC. C and δC are the curvature of the CTC track and its uncertainty. Note that there is no cut on $\Delta R(\mu, j)$. Further discussion about these cuts and their efficiencies can be found in Appendix B.

Object type	Cut	Tight Cut	Loose Cut
CEM	$E_{\rm T}^{ELCR92}$	$\geq$ 11 GeV	$\geq$ 5 GeV
	$p_{\rm T}^{raw}$	$\geq$ 4 GeV/c	$\geq$ 2.8 GeV/c
	$E_{\rm T}^{ELCR92}/p_{\rm T}^{raw}$	$\leq$ 2	$\leq$ 2
	good CTC track	yes	yes
	CONVERT2 [64]	yes	yes
	$C/\delta C$	$\geq$ 1.0	$\geq$ 1.0
PEM	$E_{\rm T}^{ELCR92}$	—	$\geq$ 5 GeV
CMU/CMP/CMUP	$p_{\rm T}^{b.c.}$	$\geq$ 11 GeV/c	$\geq$ 5 GeV/c
	good CTC track	yes	yes
	$\mid d_0 \mid$(b.c.)	$\leq$ 0.2 cm	$\leq$ 0.5 cm
	$C/\delta C$	$\geq$ 1.0	$\geq$ 1.0
CMX	$p_{\rm T}^{b.c.}$	—	$\geq$ 5 GeV/c
	good CTC track	—	yes
	$\mid d_0 \mid$(b.c.)	—	$\leq$ 0.5 cm
	$C/\delta C$	—	$\geq$ 1.0
CMIO	$p_{\rm T}^{b.c.}$	—	$\geq$ 10 GeV/c
	good CTC track	—	yes
	$\mid d_0 \mid$(b.c.)	—	$\leq$ 0.5 cm
	$C/\delta C$	—	$\geq$ 1.0
JETS	$E_{\rm T}$ (raw)	$\geq$ 10 GeV	
	$E_{\rm T}$ (corrected)	$\geq$ 15 GeV	
	$\mid \eta_{det} \mid$	$\leq$ 2.4	
	$\Delta R(e, j^{0.4})_{det}$	$\geq$ 0.4	

TABLE X. Cumulative number of events left after each cut in the dilepton analysis. The original CDF data sample corresponds to $\int \mathcal{L}\, dt = 18.6$ pb^{-1} and 87.5 pb^{-1} for Run IA and IB, respectively. No bad-run removal is applied.

	Run IA	Run IB	IA/IB
Cut $\int \mathcal{L}\, dt$ (pb^{-1}) $\rightarrow$	18.6	87.5	0.213
SUSY dilepton sample	58,221	457,478	0.127
Stage-1: Isolated dilepton ($ISO^{cal}_{0.4} \leq 4$ GeV)	20,349	143,305	0.142
Stage-2: Isolated dilepton-dijet ($E^{raw}_{\rm T}(j^{0.4}) \geq$10 GeV)	4,604	33,100	0.139
Stage-3: Isolated dilepton-dijet sample ($E_{\rm T}(j^{0.4}) \geq 15$ GeV)	229	1487	0.154
(a) Raise momentum cuts			
$p_{\rm T}(\ell_1) : 8 \rightarrow 11$ GeV/c			
$p_{\rm T}(\ell_2) : 3/4 \rightarrow 5/5$ GeV/c for μ/e			
(b) $ISO^{cal}_{0.4} \leq 4$ GeV			
(c) No fiducial volume cuts for leptons			
(d) $E_{\rm T}(j) \geq 15$ GeV with JTC96X			
(e) $\Delta R(e, j^{0.4})_{det} \geq 0.4$			

TABLE XI. Cuts used to select $Z^0 \rightarrow e^+e^-$ from the SUSY dilepton sample in addition to those listed in Table VII. The following criteria are also applied : (a) $\Delta R(e_1, e_2)_{det} > 0.4$; (b) $|z_0^{trk1} - z_0^{trk2}| \leq 10$ cm for central-central dielectron events; (c) $|z_0^{CEM} - z_0^{PEM}| \leq 10$ cm for CEM-PEM dilepton events where z_0^{CEM} and z_v^{PEM} are the track-z for CEM and the VTVZ-vertex in the PEM ELES bank, respectively. Further discussion concerning these cuts and their efficiencies can be found in Appendix B.

	Cut	Tight Cut	Loose Cut
CEM	$E_{\rm T}^{corr}$	$\geq$ 20.0 GeV	$\geq$ 20.0 GeV
	$p_{\rm T}^{raw}$	$\geq$ 10.0 GeV	$\geq$ 10.0 GeV/c
	$ISO_{0.4}^{cal}$	$\leq$ 4.0 GeV	$\leq$ 4.0 GeV
	FIDELE	yes	yes
	CONVERT2 [64]	yes	yes
PEM	$E_{\rm T}^{corr}$		$\geq$ 20.0 GeV
	$ISO_{0.4}^{cal}$		$\leq$ 4.0 GeV
	FIDELE		yes

TABLE XII. Cuts used to select $Z^0 \rightarrow \mu^+\mu^-$ from the SUSY dilepton sample in addition to those listed in Table VIII. The following cuts are applied : (a) $\Delta R(\mu_1, \mu_2)_{phys} > 0.4$; (b) $|z_0^{trk1} - z_0^{trk2}| \leq 10$ cm for central-central dimuon events.

	Cut	Tight Cut	Loose Cut
CMU/CMP	Muon Type	CMUP	CMU/CMP/CMUP
	$p_{\rm T}^{b.c.}$	$\geq$ 20.0 GeV/c	$\geq$ 20.0 GeV/c
	$EM + Had$	$\geq$ 0.1 GeV	$\geq$ 0.1 GeV
	$ISO_{0.4}^{cal}$	$\leq$ 4.0 GeV	$\leq$ 4.0 GeV
	CMUSWM	yes	yes
CMX	$p_{\rm T}^{b.c.}$		$\geq$ 20.0 GeV/c
	$EM + Had$		$\geq$ 0.1 GeV
	$ISO_{0.4}^{cal}$		$\leq$ 4.0 GeV
	CMUSWM		yes
CMX CMIO	$p_{\rm T}^{b.c.}$		$\geq$ 20.0 GeV/c
	$EM + Had$		$\geq$ 0.1 GeV
	$ISO_{0.4}^{cal}$		$\leq$ 4.0 GeV
	CMIOFID		yes

TABLE XIII. Number of Z^0 events in SUSY isolated dilepton samples before and after the two-jet requirement. The cuts to select dilepton events in this analysis are summarized in Tables XI and XII. Jets are counted with $\Delta R(\ell, j) > 0.4$. The number of Z^0 candidate events is obtained by counting events in 76 GeV/c^2 $\leq M(\ell\ell) \leq$ 106 GeV/c^2. The numbers in brackets are given as a reference from previous CDF analyses [57, 58, 59].

Category	Run IA	Run IB	IA/IB
Stage-1: Isolated dilepton sample	20,349	143,305	
(1) $Z^0 \rightarrow$ CEM-CEM	469 [560]	2,065 [2,392]	0.227
(2) $Z^0 \rightarrow$ CEM-PEM	341 [632]	2,375 [2,495]	0.144
(3) $Z^0 \rightarrow \mu^+\mu^-$	334 [330]	1,666 [1,938]	0.200
$Z^0 \rightarrow$ CMUP-CMU	46	197	
$Z^0 \rightarrow$ CMUP-CMP	20	182	
$Z^0 \rightarrow$ CMUP-CMUP	89	424	
$Z^0 \rightarrow$ CMUP-CMX	103	542	
$Z^0 \rightarrow$ CMUP-CMIO	76	321	
Stage-3: Isolated dilepton-dijet sample			
($\Delta R_j^{cone} = 0.4$)	229	1,487	
(1) $Z^0 \rightarrow$ CEM-CEM	23	85	0.271
(2) $Z^0 \rightarrow$ CEM-PEM	8	78	0.103
(3) $Z^0 \rightarrow \mu^+\mu^-$	11	50	0.220
$Z^0 \rightarrow$ CMUP-CMU	4	9	
$Z^0 \rightarrow$ CMUP-CMP	1	6	
$Z^0 \rightarrow$ CMUP-CMUP	3	11	
$Z^0 \rightarrow$ CMUP-CMX	1	12	
$Z^0 \rightarrow$ CMUP-CMIO	2	12	

deficit in $Z^0 \rightarrow$ CEM-PEM events in Run IA data can be explained by a charge significance cut ($C/\delta C \geq 1$ in Table IX) for all leptons including the plug (PEM) electrons. In Run IB, no such requirement was made for the dilepton sample. However, due to the charge requirement of the leptons, only the number of central-central dilepton events for the SUSY dilepton analyses are important and therefore the number of CEM-PEM events in the final sample are unimportant, but this is mentioned for sake of completeness. The number of $Z^0 \rightarrow ee$ events in each jet multiplicity is listed in Table XIV. There is a disagreement of $N(Z^0 \rightarrow ee + n\text{-jet})$ between this analysis and a previous published CDF analysis [57]. This is mainly explained by an inclusion of $Z^0 \rightarrow$ CEM-FEM events in the other analysis and a deficit in $Z^0 \rightarrow$ CEM-PEM events (because of a charge significance cut with $C/\delta C \geq 1$ for PEM) in the Run IA selected data. A Run IB Stream A dimuon sample is provided by the Harvard University and Johns Hopkins University groups. Using the same analysis code, one finds that there are 1632 $Z^0 \rightarrow \mu\mu$ events counted in the Z^0 mass window $76 \leq M(\mu\mu) \leq 106$ GeV/c^2. This is in agreement with results of 1666 events (counted in the Z^0 mass window)[60]. The number of $Z^0 \rightarrow \mu\mu$ events in each jet multiplicity is listed in Table XV. Figure 36 shows distributions of relative jet multiplicity of Z^0 event candidates from the SUSY Stage-1 sample, ISAJET Monte Carlo sample, and the results from another CDF analysis on the properties of jets in $Z^0 \rightarrow ee$ events [57, 61, 62]. For comparison, the relative jet multiplicity is also shown for cone size 0.7 [65]. They agree with each other within the statistical uncertainties. In conclusion, the number of $Z^0 \rightarrow$ central-central dilepton (ee, $\mu\mu$) events in the Stage-3 sample is consistent with results from other analyses [57, 58, 59, 60].

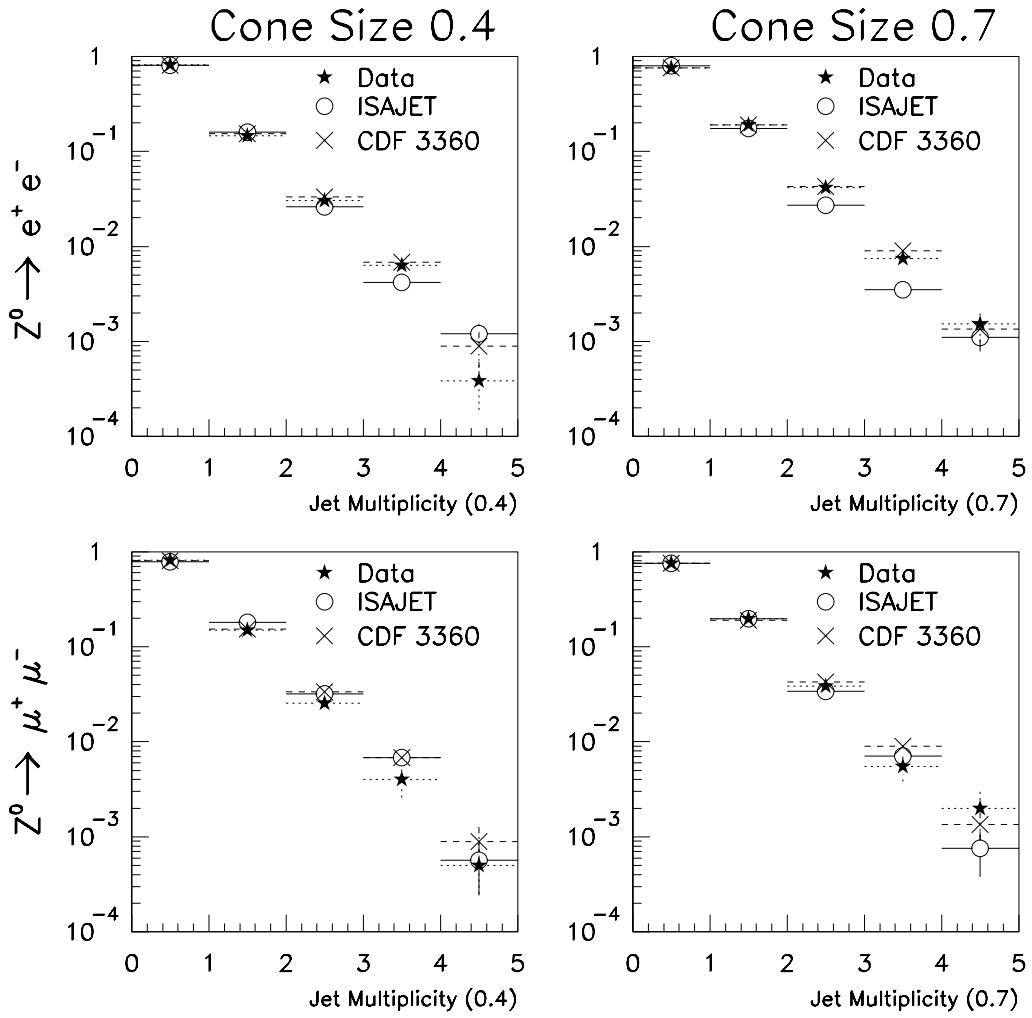

FIG. 36. Jet multiplicity in the $Z^0 \rightarrow \ell^+\ell^-$ events in the SUSY isolated dilepton sample (from Stream B exotic dilepton sample) using both cone sizes. Results are compared to ISAJET Monte Carlo and the CDF $Z^0 \rightarrow ee$ analysis (from the Stream A inclusive sample) which was previously labeled under CDF internal report number 3360[57].

TABLE XIV. Number of $Z^0(\rightarrow ee) + n$-jets events in the Stage-3 sample (Run IA + IB). The cuts to select dilepton events in this analysis are summarized in Table XI. Jets are separated from electrons ($\Delta R(e,j) > 0.4$). The number of Z^0 events is obtained by counting events in 76 GeV/$c^2 \leq M(ee) \leq$ 106 GeV/c^2. The numbers in brackets refer to the CDF published analysis in Ref. [57] and include $Z^0 \rightarrow$ CEM-CEM, CEM-PEM, and CEM-FEM events [57].

N_j	$Z^0 \rightarrow ee$ (CEM-CEM & CEM-PEM)		$Z^0 \rightarrow ee$ (CEM-CEM)	$Z^0 \rightarrow ee$ (CEM-PEM)
≥ 2	194	[281]	108	86
2	157	[224]	87	70
3	32	[46]	19	13
4	2	[6]	1	1
5	3	[3]	1	2
6	0	[1]	0	0
7	0	[1]	0	0

TABLE XV. Number of $Z^0(\rightarrow \mu\mu) + n$-jets events in the Stage-3 sample (Run IA + IB). The cuts to select dilepton events in this analysis are summarized in Table XII. Jets are counted with $\Delta R(\mu,j) > 0.4$. The number of Z^0 events is obtained by counting events in 76 GeV/$c^2 \leq M(\mu^+\mu^-) \leq$ 106 GeV/c^2.

N_j	$Z^0 \rightarrow \mu\mu$	CMUP -CMU	CMUP -CMP	CMUP -CMUP	CMUP -CMX	CMUP -CMIO
≥ 2	61	13	7	14	13	14
2	51	13	5	11	10	12
3	8	0	1	2	3	2
4	1	0	0	1	0	0
5	1	0	1	0	0	0

2. **Top Dilepton Events**

There are nine top OS-dilepton event candidates (7 $e\mu$, 1 ee, and 1 $\mu\mu$) in the latest analysis[63]. Only one (Run/Event = 57621/45230) out of nine dilepton events is not in the SUSY dilepton sample. The event does not exist in the XDLB_5P sample.

Seven are found in the Stage-3 ΔR_j^{cone}=0.4 sample. The reasons for rejecting four (five) dilepton events in the top dilepton analysis can completely be explained by the differences in selection cuts between two independent analyses. The results are summarized in Table XVI.

TABLE XVI. List of the nine dilepton events found in 'official' top OS-dilepton event candidates (7 $e\mu$, 1 ee, and 1 $\mu\mu$) in the latest analysis are also indicated by $\surd$[63]. Seven of the nine events are found in the Stage-3 ΔR_j^{cone}=0.4 sample and indicated by ‡. A cross-check with jet cone size ΔR_j^{cone}=0.7 is denoted by $*$.

		Run/Event Numbers [63]	Event Type by This Analysis ($\Delta R_j^{cone} = 0.7$)	(a) Not in sample (0.4/0.7) ? (b) Any other comments
	$\surd$	41540/ 127085	$\mu_1^+ e_2^- + j_1(\mu_3^-)\ j_2(\mu_4^+)$	(a) $ISO_{0.4}^{cal}(\mu_1^+) = 76$ GeV (b) $\Delta R(\mu_1, j_1) \simeq 0.4$ $ISO_{0.4}^{cal}(e_2^-) = 0.9$ GeV
	$\surd$	45047/ 104393	$\mu_1^- e_2^+ + j_1\ j_2$	(a) $ISO_{0.4}^{cal}(e_2) = 4.3$ GeV (> 4 GeV) and $Had/Em(e_2) = 0.06$ (> 0.05). (b) $\phi(\mu_1) \simeq \phi(j_1) \simeq \phi(j_2)$
$*‡$	$\surd$	47122/ 38382	$e_1^+ \mu_2^- + j_1 j_2$	(a) –
	$\surd$	57621/ 45230	$e_1^+ \mu_2^- + j_1(\mu_3^+) + j_2$	(a) Not in XDLB_5P sample. (b) $ISO_{0.4}^{cal}(\mu_3) = 19$ GeV
$*‡$	$\surd$	63700/ 272140	$\mu_1^+ \mu_2^- + j_1 j_2$	(a) – (b) $M(\mu\mu) = 65$ GeV/c^2 $\Delta R(\mu_1, j_1) \simeq 0.7$
$*‡$	$\surd$	66046/ 380045	$e_1^+ \mu_2^- + j_1 j_2 j_3$	(a) –
‡	$\surd$	67581/ 129896	$e_1^+ \mu_2^- + j_1(e_3^-)$	(a) No second jet with $\Delta R_j^{cone} = 0.7$ (b) $j_1(E_{\rm T}^{raw} = 99$ GeV$) = j_2 + e_3$ $E_{\rm T}^{raw}(j_2) = 71$ GeV $E_{\rm T}^{raw}(e_3) = 24$ GeV
$*‡$	$\surd$	68185/ 174611	$e_1^+ e_2^- + j_1 j_2$	(a) – (b) $M(ee) = 31$ GeV/c^2
$*‡$	$\surd$	69808/ 639398	$\mu_1^+ e_2^- + j_1 j_2 j_3$	(a) – (b) j_1/j_2 (0.7) are j_2/j_1 (0.4).

CHAPTER VI

RESULTS

A. Introduction

This chapter discusses the reduction of data through cuts which either veto backgrounds or ensure proper identification of leptons, jets, and missing energy. It is here that the reduction is confirmed via the background estimate provided from ISAJET[61] Monte Carlo simulations which are passed through the detector simulation (QFL′[54]) and weighted by lepton identification, isolation, and trigger efficiency corrections. Afterwards, the acceptance of signal events from squarks ($\tilde{q}$) and gluinos ($\tilde{g}$) based on ISAJET Monte Carlo simulations is analyzed. Systematic uncertainties on the total efficiency of accepting dilepton events from supersymmetric processes are also studied. Due to the consequence of finding no events after all cuts, mass and production limits for gluinos ($\tilde{g}$) and squarks ($\tilde{q}$) at the 95% confidence level are presented.

B. Data Analysis

The reduction of the number of events in the Stage-3 sample is done to remove Standard Model background processes. Bad runs are also removed from this sample. This reduction of the data occurs in six stages.

1. Stage-4: Trigger Selected Isolated Dilepton Dijet Sample

Stage-4 is the Stage-3 dataset requiring that events pass chosen trigger paths. The sample is required to have either an electron or a muon trigger path. Here, it is required that at least one lepton (e or μ) pass level 1, level 2, and level 3 inclusive

lepton triggers since these triggers (see Tables IV and V) compose the majority of the dilepton samples. The tight lepton passes the trigger since stringent quality cuts are imposed. The number of events surviving are **179** and **1024** from Run IA and Run IB, respectively.

2. Stage-5: Isolated Central-Central Dilepton Dijet Sample

The Stage-5 criteria demand that the tight lepton is either a fiducial electron or muon in the central region. Tight muons are required to traverse the CMU and CMP muon detectors. The track z position at the beamline is within 5 cm of the primary interaction in z. The interaction vertex is required to be within 60 cm of the center of the detector which is the fiducial region of the VTX. The requirements made on the tight lepton ensure that it was passed by one of the inclusive triggers. The second lepton is required to pass fiducial requirements, pass through the central region of the CDF detector, and whose vertex is within 5 cm of the tight lepton. Electrons that originate from photon conversions are vetoed [64]. Muons that originated from cosmic rays are also vetoed [66]. The leptons are required to be well separated ($\Delta R(\ell_1, \ell_2) \geq 0.4$) to aid the isolation requirement. Track isolation ($ISO^{trk}_{0.4} \leq 4$ GeV/c) is imposed on both leptons (see Appendix C). Tracks recognized as muons are required to present some minimum amount of ionization in the calorimeter ($EM + Had \geq 0.1$ GeV). Leptons and jets are required to be separated ($\Delta R(\ell, j) \geq 0.4$) in order to prevent the misidentification of leptons as hadronic jets. At this stage, bad runs are removed. There are **71** and **279** events remaining after selection from Run IA and Run IB, respectively.

3. Stage-6: $M(\ell\ell') \geq 12$ GeV/c^2

The ISAJET Monte Carlo program which generates the signal events as well as the Standard Model background processes for this analysis does not generate J/ψ, Υ, and other resonances. Hence, this analysis requires $M(\ell^+\ell^-) \geq 12$ GeV/c^2. This analysis requires a low-mass dilepton mass cut ($M(\ell\ell') > 12$ GeV/c^2) for opposite sign as well as like-sign dilepton events in order to equalize the topology in the remaining selected events. After applying this cut, there are **53** and **202** events in CDF Run IA and IB data, respectively.

4. Stage-7: Z^0 Veto

Since one of the dominant Standard Model backgrounds is $Z^0 \rightarrow \ell\ell$, events where the invariant mass of opposite-sign and same-flavor ($e^{\pm}e^{\mp}$ or $\mu^{\pm}\mu^{\mp}$) dilepton pair lies within the Z^0 mass window (76 GeV/$c^2 \leq M(\ell^+\ell^-) \leq$ 106 GeV/c^2) are vetoed. There are 81 $Z^0(\rightarrow e^+e^-)+ \geq 2$ jet events and 46 $Z^0(\rightarrow \mu^+\mu^-)+ \geq 2$ jet events from CDF Run I in the Stage-6 sample. Thus, the number of events at Stage-7 is **29** and **99** events from Run IA and IB, respectively.

5. Stage-8: Missing Transverse Energy Cut

In order to remove most of the events from Drell-Yan and $b\bar{b}/c\bar{c}$ production, events are required to have a large $\not\!\!E_{\rm T}$ value. Missing transverse energy in the detector is based on calorimeter tower energies. The electromagnetic and hadronic energies (E^{EM} and E^{HAD}) in the central, plug, and forward calorimeter are measured :

$$E_{x_i} = E_i^{EM} \sin\theta_i^{EM} \cos\phi_i + E_i^{HAD} \sin\theta_i^{HAD} \cos\phi_i \quad (6.1)$$

$$E_{y_i} = E_i^{EM} \sin\theta_i^{EM} \cos\phi_i + E_i^{HAD} \sin\theta_i^{HAD} \cos\phi_i \quad (6.2)$$

where θ_i and ϕ_i are the polar and azimuthal angles of the electromagnetic and hadronic

parts of i^{th} tower measured from the vertex. These calorimeter tower energies are summed over all towers :

$$\not\!\!E_{\mathrm{T}x} = -\sum_{i=1}^{N_{towers}} E_{x_i} \tag{6.3}$$

$$\not\!\!E_{\mathrm{T}y} = -\sum_{i=1}^{N_{towers}} E_{y_i} \tag{6.4}$$

The missing transverse energy is thus presented as a vector:

$$\vec{\not\!\!E}_{\mathrm{T}}^{\,METS} = \vec{\not\!\!E}_{\mathrm{T}x}\hat{\mathbf{x}} + \vec{\not\!\!E}_{\mathrm{T}\mathbf{y}}\hat{\mathbf{y}} \tag{6.5}$$

with magnitude :

$$|\,\vec{\not\!\!E}_{\mathrm{T}}^{\,METS}\,| = \sqrt{\not\!\!E_{\mathrm{T}x}^{\,2} + \not\!\!E_{\mathrm{T}y}^{\,2}} \tag{6.6}$$

This measurement of $\not\!\!E_{\mathrm{T}}$ is stored in the METS bank. However, since muons are minimum ionizing, their transverse momenta are not reconstructed by the calorimeter. Jets can be mismeasured during event reconstruction. Therefore, the missing transverse energy needs to be corrected for muons and mismeasured jets. Hence, the missing transverse energy ($\vec{\not\!\!E}_{\mathrm{T}}$) must be calculated via the following equation :

$$\vec{\not\!\!E}_{\mathrm{T}} = \vec{\not\!\!E}_{\mathrm{T}}^{\,METS} + \sum_{\mu}[(\vec{E}_{\mathrm{T}}(\mu)^{tower} - \vec{p}_{\mathrm{T}}(\mu)] + \sum_{jet}[(\vec{E}_{\mathrm{T}}(j)^{raw} - \vec{E}_{\mathrm{T}}(j)^{NNDD}] \tag{6.7}$$

where $E_{\mathrm{T}}(j)^{NNDD}$ refers to jet energy corrected by JTC96X (see Appendix D) with the NNDD option (N = no underlying-event correction; N = no out-of-cone correction; D = default absolute energy scale; D = default relative energy scale) which is done to avoid double counting of the energy corrections. $\not\!\!E_{\mathrm{T}}^{\,METS}$ is the missing transverse energy value read from the METS bank. With $\not\!\!E_{\mathrm{T}} > 25$ GeV, **19** events are accepted from the CDF Run I dataset. All 19 events are OS dilepton events. Six of them are top dilepton events. Table XVII is a summary of the top dilepton event candidates

TABLE XVII. List of nine 'official' top OS-dilepton event candidates (7 $e\mu$, 1 ee, and 1 $\mu\mu$) in the latest analysis [63]. Six of the nine events are found in the Stage-8 sample and indicated by $\surd$.

Run/Event Numbers	Stage-8	Dilepton Type	Why not in the sample ?
41540/ 127085		$\mu_1^+ e_2^-$	$ISO_{0.4}^{cal}(\mu_1^+) = 76$ GeV $\Delta R(\mu_1, j_1) \simeq 0.4$
45047/ 104393		$\mu_1^- e_2^+$	$ISO_{0.4}^{cal}(e_2) = 4.3$ GeV (> 4 GeV) $Had/Em(e_2) = 0.06$ (> 0.05).
47122/ 38382	$\surd$	$e_1^+ \mu_2^-$	–
57621/ 45230		$e_1^+ \mu_2^-$	Not in XDLB_5P sample.
63700/ 272140	$\surd$	$\mu_1^+ \mu_2^-$	–
66046/ 380045	$\surd$	$e_1^+ \mu_2^-$	–
67581/ 129896	$\surd$	$e_1^+ \mu_2^-$	–
68185/ 174611	$\surd$	$e_1^+ e_2^-$	–
69808/ 639398	$\surd$	$\mu_1^+ e_2^-$	–

in the Stage-8 sample[63]. All events rejected by the SUSY analysis can be explained by the difference of the event selection cuts between the SUSY and the top dilepton analyses.

At the present stage, the lepton $p_{\rm T}$ cuts are lower than those in the Run IA SUSY dilepton analysis, while the lepton identification cuts are similar in both analyses. Thus, the dilepton dijet analysis should accept the two events that were found previously :

47122/38382 This top $e^+\mu^-$ (CEM+CMX) event is found after the $\not\!\!E_T \geq 25$ GeV cut (in the Stage-8 sample).

47311/71056 This $\mu^+\mu^-$ (CMP+CMX) event is rejected at Stage-4, because the present cuts require the tight muon to pass through the CMU and CMP, while Ref. [56] accepts this dimuon (CMP+CMX) event.

The present result is consistent with the previous analysis.

6. Stage-9: Like-Sign Dilepton Cut

In order to effectively remove Standard Model dilepton backgrounds which are mostly opposite sign dilepton events, a like-sign dilepton ($e^\pm e^\pm$, $\mu^\pm\mu^\pm$, or $e^\pm\mu^\pm$) cut is required. No candidates remain after this cut. The cumulative number of events after each cut in this analysis is summarized in Table XVIII.

C. Background Estimate

The principal Standard Model backgrounds to the like-sign dilepton signature are events from: (*i*) Drell-Yan (γ,Z^0) process, (*ii*) diboson production, (*iii*) $b\bar{b}/c\bar{c}$ production, and (*iv*) $t\bar{t}$ production. The yield for each process is evaluated with the integrated luminosity of 106 pb^{-1} using ISAJET Monte Carlo events with MRSD0′ used as the parton distribution function. The validation of the ISAJET Monte Carlo is described in Appendix E. The cross-section from ISAJET is corrected to the next-to-leading order (NLO) cross-section or to the CDF measured cross-section (see details in Appendix E).

TABLE XVIII. The event selection is presented in stages for Run IA and Run IB data samples. The result consists of no like-sign dilepton dijet events with significant $\not\!\!E_{\rm T}$ in 106 pb^{-1} of data.

Cut	Run IA	Run IB	IA+IB
SUSY Dilepton Sample	58221	457478	515699
Stage-1: Isolation Dilepton ($ISO^{cal}_{0.4} \leq 4$ GeV)	20349	143305	163654
Stage-2: Isolated Dilepton Dijet ($E_T^{raw}(j) > 10$ GeV)	4604	33100	37704
Stage-3: Isolated Dilepton Dijet ($E_T(j) > 15$ GeV)	229	1487	1716
Stage-4: Trigger Selected Isolated Dilepton Dijet	179	1024	1203
Stage-5: Isolated CC Dilepton Dijet	71	279	350
OS $ee/\mu\mu$	32/27	135/100	167/127
OS $e\mu$	6	25	31
LS $ee/\mu\mu$	3/ 1	5/ 1	8/ 2
LS $e\mu$	2	13	15
Stage-6: $M(\ell\ell') > 12$ GeV/c^2	53	202	255
OS $ee/\mu\mu$	28/18	101/ 69	129/87
OS $e\mu$	3	20	23
LS $ee/\mu\mu$	2/ 0	4/ 0	6/ 0
LS $e\mu$	2	8	10
Stage-7: Z^0 (76-106 GeV/c^2) veto	29	99	128
OS $ee/\mu\mu$	14/8	34/33	48/41
OS $e\mu$	3	20	23
LS $ee/\mu\mu$	2/ 0	4/ 0	6/ 0
LS $e\mu$	2	8	10
Stage-8: $\not\!\!E_{\rm T} > 25$ GeV	2	17	19
OS $ee/\mu\mu$	1/0	3/5	4/5
OS $e\mu$	1	9	10
LS $ee/\mu\mu$	0/0	0/0	0/0
LS $e\mu$	0	0	0

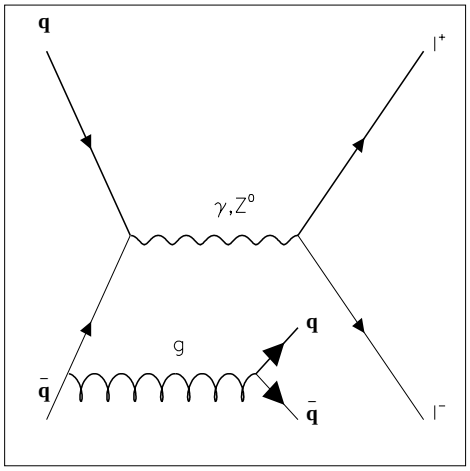

FIG. 37. A Feynman diagram is shown displaying Drell-Yan plus two jets.

1. **Drell-Yan Process**

Drell-Yan (γ, Z^0) can contribute to dilepton dijet sample via the Feynman diagram shown in Fig. 37. Missing energy from these events is due to mismeasurement of jets associated with this process. Like-sign dilepton events are contributed from misidentified leptons in addition to the leptons produced from the Drell-Yan process. The number of events expected in 106 pb^{-1}of data is 0.00 $\pm$ 0.01 (stat) $\pm$ 0.01 (syst) for γ^*, and 0.00 $\pm$ 0.04 (stat) $\pm$ 0.02 (syst) for Z^0.

2. **Diboson Production**

The main contribution from diboson production is $W^{\pm}Z^0$ associated with two or more jets via gluon radiation as seen in Fig. 38. The leptonic decay of the $W^{\pm}Z^0$ diboson pair with two or more jets mimics the supersymmetric signal searched for in this analysis. The number of diboson ($W^{\pm}W^{\mp}$, $W^{\pm}Z^0$, and Z^0Z^0) events expected in 106 pb^{-1}of data is estimated to be 0.24 $\pm$ 0.10 (stat) $\pm$ 0.01 (syst).

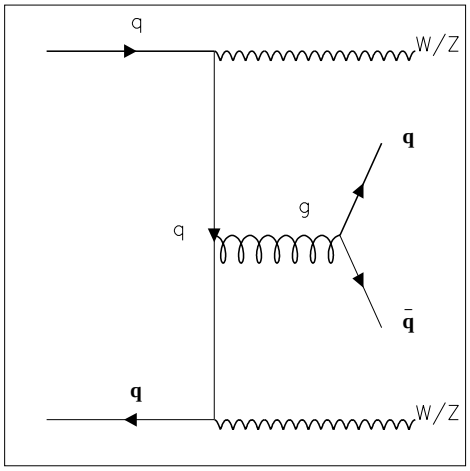

FIG. 38. A Feynman diagram is shown displaying diboson production and decay.

3. Bottom and Charm Production

A Monte Carlo sample of $b\overline{b}/c\overline{c}$ was simulated for three different processes : direct production, initial state gluon splitting, and final state gluon splitting (in three different $p_{\rm T}$ ranges) for $b\overline{b}/c\overline{c}$. Each event in the Monte Carlo sample contains at least two leptons (either muon or electron). One lepton must have $p_{\rm T} > 9.0$ GeV/c and $|\eta| < 1.5$, and the other lepton must have $p_{\rm T} > 2.8$ GeV/c and $|\eta| < 3.0$. These cuts guarantee full efficiency for tight leptons (≥ 11 GeV/c) and loose leptons (≥ 5 GeV/c). It has been known that $B^0\bar{B}^0$ mixing can yield like-sign dileptons [68]. The Feynman diagram demonstrating $B^0\bar{B}^0$ mixing is shown in Fig. 39.

Since ISAJET does not generate like-sign dileptons due to $B^0\bar{B}^0$ mixing, the effect must be incorporated by hand. The proper number of opposite sign (OS) and like-sign (LS) events from $B^0\bar{B}^0$ mixing are given in Eq. 6.8 [69]:

$$\left.\begin{aligned} N_{OS} &= ((1-\chi)^2+\chi^2)OS_{ISAJET} + 2\chi(1-\chi)LS_{ISAJET} \\ N_{LS} &= 2\chi(1-\chi)OS_{ISAJET} + ((1-\chi)^2+\chi^2)LS_{ISAJET} \end{aligned}\right\} \quad (6.8)$$

where χ is the averaged mixing parameter. With a CDF measurement of $\chi = 0.118 \pm$

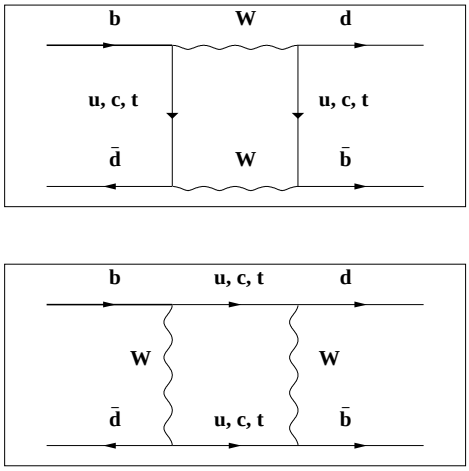

FIG. 39. A Feynman diagram demonstrates $B^0\bar{B}^0$ mixing.

0.008 ± 0.020 [69], one obtains:

$$\left.\begin{aligned} N_{OS} &= (0.792 \pm 0.044)OS_{ISAJET} + (0.208 \pm 0.044)LS_{ISAJET} \\ N_{LS} &= (0.208 \pm 0.044)OS_{ISAJET} + (0.792 \pm 0.044)LS_{ISAJET} \end{aligned}\right\} \tag{6.9}$$

The number of $b\bar{b}/c\bar{c}$ events expected in 106 pb^{-1}data is 0.23 $\pm$ 0.23 (stat) $\pm$ 0.06 (syst).

4. $t\bar{t}$ Production

One of main decay modes is

$$t + \bar{t} \;\rightarrow\; (W^+b) + (W^-\bar{b}) \rightarrow (\ell^+\nu + \bar{b}) + (q\bar{q}' + c\;\ell^+\nu). \tag{6.10}$$

The Feynman diagram demonstrating a like-sign signature from $t\bar{t}$ is shown in Fig. 40.

The yield at 106 pb^{-1} is expected to be about 20 events before any cuts (*i.e.*, just calculated by cross section and branching ratios). The following numbers are used for the above calculation: $\sigma_{t\bar{t}} = 7.6$ pb, $BR(W^+ \rightarrow q\bar{q}') = 0.678$, $BR(W^- \rightarrow \ell^-\nu)$ = 0.107 (per lepton), $BR(\bar{b} \rightarrow \bar{c}\ell^+\nu) = 0.095$ (per lepton). The acceptance for

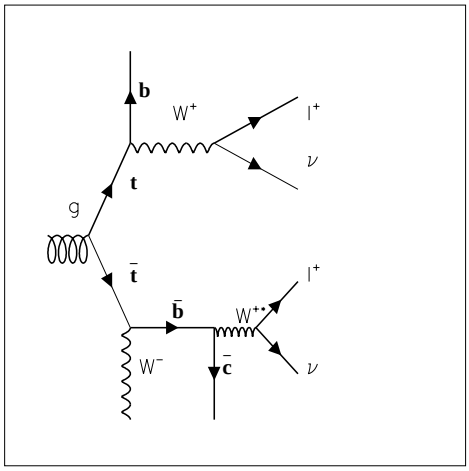

FIG. 40. A Feynman diagram indicates a like-sign dilepton signature can be contributed from $t\bar{t}$.

$W \to \ell\nu$ is about 30%. Thus, about six like-sign dilepton events are expected before the isolation requirement for the lepton from b-decay. Roughly, one expects less than one event after the isolation is required. The mass of the top quark is assumed to be 175 GeV/c^2. Taking $\sigma_{t\bar{t}} = 7.6$ pb, the number of events expected in 106 pb^{-1}data is obtained to be 0.08 ± 0.04 (stat) $\pm$ 0.02 (syst).

5. Total Dilepton Background in Run I

The distributions of the dilepton mass and missing transverse energy from data and the Standard Model background Monte Carlo after applying the $M(\ell,\ell) \geq 12$ GeV/c^2 cut but before the Z^0 veto are shown in Fig. 41. There is good agreement between data and Monte Carlo events. The Standard Model background contributions after the $\not\!\!E_{\rm T} \geq 25$ GeV cut are summarized in Table XIX. Systematic uncertainties on the normalization from Monte Carlo are discussed elsewhere (see Appendix E).

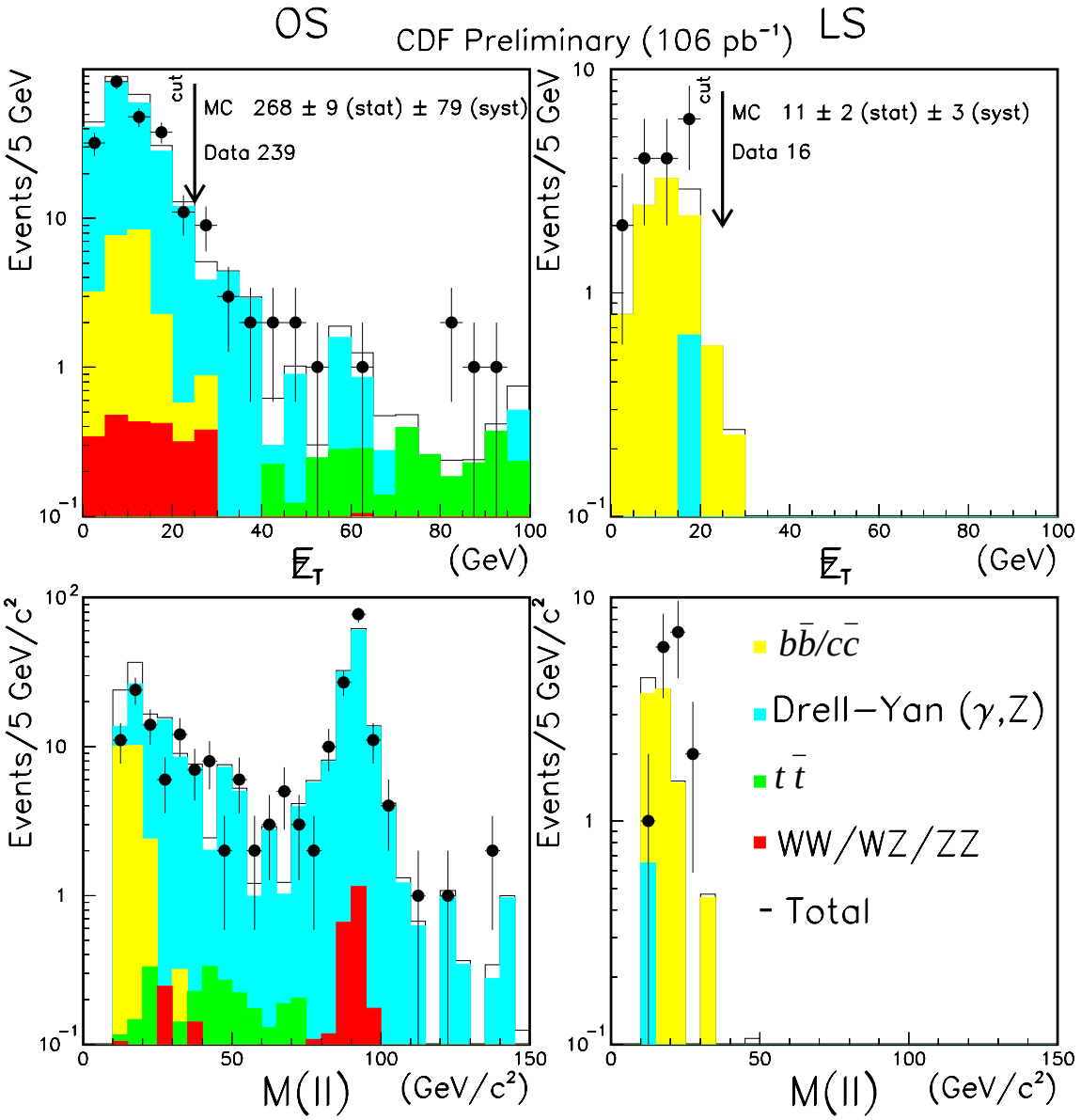

FIG. 41. The $\not\!\!E_{\rm T}$ and $M(\ell,\ell)$ distributions displaying data and the expected Standard Model background using ISAJET 7.16 [61] with MRSD0′ as the parton density function at Stage-6. The arrow displays where the $\not\!\!E_{\rm T}$ cut is made. One can see that there are no like-sign dilepton events after $\not\!\!E_{\rm T} \geq 25$ GeV.

TABLE XIX. The CDF preliminary estimate on the numbers of opposite sign and like-sign dilepton events from expected Standard Model sources using ISAJET (MRSD0′) after $\not\!\!E_{\rm T} \geq 25$ GeV cut is compared to 106 pb^{-1} of data.

Source	OS	LS
Drell-Yan	$8.7 \pm 0.9 \pm 0.4$	$0.00 \pm 0.01 \pm 0.01$
$t\bar{t}$	$4.0 \pm 0.3 \pm 1.0$	$0.08 \pm 0.04 \pm 0.02$
$b\bar{b}/c\bar{c}$	$0.9 \pm 0.9 \pm 0.2$	$0.23 \pm 0.23 \pm 0.06$
$WW/WZ/ZZ$	$0.5 \pm 0.1 \pm 0.1$	$0.24 \pm 0.10 \pm 0.01$
Total	$14.1 \pm 1.3 \pm 1.1$	$0.55 \pm 0.25 \pm 0.06$
Data	19	0

D. Total Detection Efficiency

1. Definition

The total detection efficiency, ϵ^{tot}, for $\tilde{g}\tilde{g}, \tilde{g}\tilde{q}, \tilde{q}\tilde{q}, \tilde{q}\bar{\tilde{q}} \to \ell^{\pm}\ell'^{\pm} + X$ can be expressed as

$$\epsilon^{tot} = A \cdot \epsilon_{2\ell}^{trig}, \tag{6.11}$$

where

A = acceptance for dilepton events after all cuts;

$\epsilon_{2\ell}^{trig}$ = $p_{\rm T}$-dependent dilepton trigger efficiency.

Here, ℓ_1 represents a tight electron or muon and ℓ_2 refers to a loosely selected lepton in the central region.

2. Acceptance of Signal

The acceptance, A, for $\tilde{g}\tilde{g}, \tilde{g}\tilde{q}, \tilde{q}\tilde{q}, \tilde{q}\bar{\tilde{q}} \to \ell^{\pm}\ell'^{\pm} + X$ is defined as :

$$A = \epsilon_{2\ell}^{kin/geom} \cdot \epsilon_{2j}^{kin/geom} \cdot \underbrace{\left[\epsilon_{\ell_1}^{ID}\epsilon_{\ell_2}^{ID}\right]}_{\epsilon_{2\ell}^{ID}} \cdot \underbrace{\left[\epsilon_{\ell_1}^{ISO}\epsilon_{\ell_2}^{ISO}\right]}_{\epsilon_{2\ell}^{ISO}} \cdot \epsilon_{\not\!\!E_{\rm T}} \cdot \epsilon_z \cdot \epsilon_{LS}, \qquad (6.12)$$

where

$\epsilon_{2\ell}^{kin/geom}$ = Kinematical/geometrical acceptance for leptons with $\Delta R(\ell_1\ell_2) > 0.4$;

$\epsilon_{2j}^{kin/geom}$ = Kinematical/geometrical acceptance for jets with $\Delta R(\ell j) > 0.4$;

ϵ_{ℓ}^{ID} = Lepton ID efficiency for ℓ;

ϵ_{ℓ}^{ISO} = $\epsilon_{\ell}^{ISO_{0.4}^{cal}<4\ \rm GeV} \times \epsilon_{\ell}^{ISO_{0.4}^{trk}<4\ \rm GeV/c}$;

$\epsilon_{\not\!\!E_{\rm T}}$ = Event acceptance for $\not\!\!E_{\rm T} > 25$ GeV;

ϵ_z = Event acceptance for $|z_{event}| < 60$ cm;

ϵ_{LS} = Event acceptance for like-sign cut.

The acceptance is defined as the ratio of dilepton events passing all cuts to the number of dilepton events at generator level using ISAJET 7.20[61] (CTEQ3L[71]). The acceptance varies between 1-3% in the region where a limit is expected. The acceptance increases as a function of gluino mass in the case where the squark mass is heavy. One sees that the acceptance decreases slightly with increasing gluino mass where the squark and gluino have nearly the same mass. This is due to different contributions of the rates of the intermediary charginos and neutralinos in the cascade decays. The acceptance of signal is determined as a function of gluino mass for two scenarios: (1) $M_{\tilde{q}} = M_{\tilde{g}} + 1$ GeV/c^2 and (2) $M_{\tilde{q}} \gg M_{\tilde{g}}$ in Fig. 42.

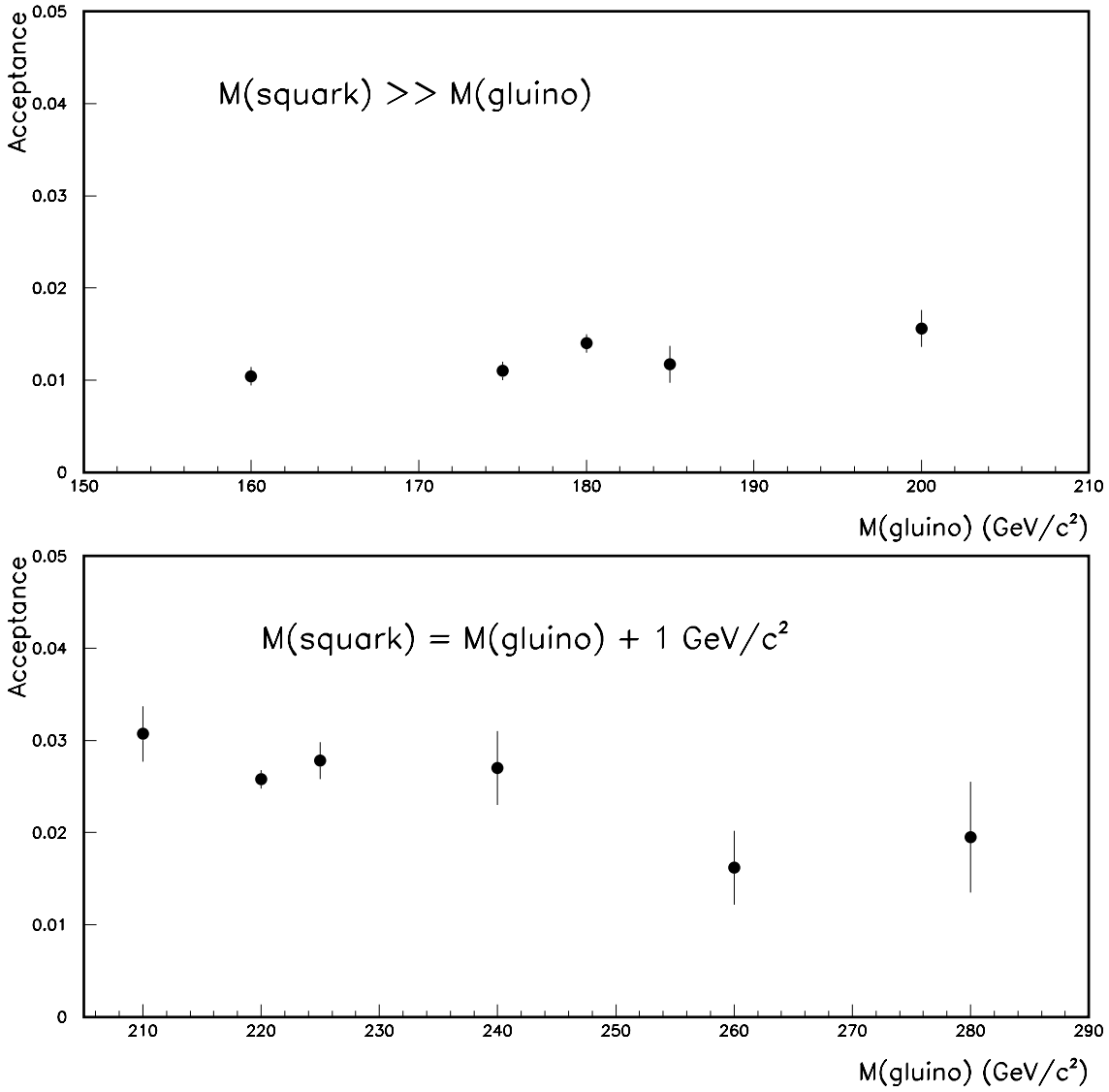

FIG. 42. Acceptance is presented as a function of $M_{\tilde{g}}$ for the case where $M_{\tilde{q}} \gg M_{\tilde{g}}$ and also for the case where $M_{\tilde{q}} \simeq M_{\tilde{g}}$ using ISAJET 7.20[61] (CTEQ3L[71]). Only statistical errors are shown.

3. Efficiency Corrections

Due to the fact that the Monte Carlo does not simulate effects due to aging or multiple interactions, the lepton identification and lepton isolation efficiencies must be corrected (see Appendices C and D). The lepton identification correction between Monte Carlo and data is $\simeq 90\%$ (per dilepton event) and weakly dependent on gluino mass. The lepton isolation correction factor is $\simeq 85\%$ (per dilepton event) and also depends weakly on gluino mass.

Only inclusive lepton trigger efficiencies are studied for this analysis. The parameterized trigger efficiency is applied to the tight lepton. A weighting of the Run IA and Run IB trigger efficiencies is done. In Run IB, there are low and high p_T^ℓ triggers. The maximum of the two efficiencies is taken. The trigger efficiency estimated for the SUSY Monte Carlo is $\simeq 80\%$.

Multiplying the efficiency corrections, trigger efficiency, and the acceptance, one forms the product called the total efficiency. The total efficiency now represents the ability to find a supersymmetric dilepton event in the CDF detector. It is this total efficiency that is used to determine the cross-section limit after determining the statistical and systematic uncertainties.

E. Systematic Uncertainties

The cross section (σ) times the branching ratio (BR) is experimentally measured by

$$\sigma \cdot BR \;=\; \frac{N_{obs} - N_{BG}}{\epsilon^{tot} \cdot \int \mathcal{L}\, dt}\,. \tag{6.13}$$

Thus, the uncertainty in this measurement is estimated due to uncertainties in the determination of total detection efficiency (ϵ^{tot}) and integrated luminosity ($\int \mathcal{L}\, dt$).

1. Lepton Trigger Efficiency

The trigger efficiency for dilepton is calculated event by event, depending on the lepton $p_{\mathrm{T}}^{\ell_1}$. The systematic uncertainty due to the trigger efficiencies is determined by varying the parameterized curves by one standard deviation for level 1, level 2, and level 3 triggers which comprise the majority of the dilepton sample. Uncertainty due to the trigger efficiency is $\simeq 5\%$.

2. Lepton Identification Efficiencies

The lepton identification (ID) efficiency (ϵ_ℓ^{ID}) is determined from real data for Run IA and Run IB (see Appendix B). Both Run IA and Run IB results are found to be consistent within statistical uncertainty. Thus, the result from Run IB data is used to evaluate the uncertainty. In the present dilepton dijet selection, the first lepton is required to have either an energy cluster in the CEM (if it is an electron) or a track crossing both the CMU and CMP (if it is a muon). The second lepton (electron or muon) is loosely required to be in the central region. This uncertainty is determined by varying the ID efficiency by one standard deviation and applying this to the Monte Carlo sample. The uncertainty is found to be $\simeq 3\%$.

3. Lepton Isolation Efficiencies

The lepton isolation efficiency (ϵ_ℓ^{ISO}) is determined from $Z^0(\rightarrow \ell^+\ell^-)+ \geq$ 2-jets events in Run I (see Appendix C). The isolation efficiency is calculated by the product of the calorimeter isolation efficiency and the track isolation efficiency. Here, again, the efficiency as seen in data is varied by one standard deviation to examine the effect on the Monte Carlo. This uncertainty is found to be $\simeq 11\%$.

4. Jet Energy Scale

The jet energy scale can effect the missing transverse energy spectra as well as the threshold for observing dilepton dijet events. The major components effected by this are the absolute and relative energy corrections (see Appendix D). The absolute and relative energy scales are varied by 5% to determine the effect on the acceptance. This uncertainty varies between 1-5% depending on the gluino and squark masses.

5. Gluon Radiation

Gluon radiation can be produced in $\tilde{g}\tilde{g}$, $\tilde{g}\tilde{q}$, and $\tilde{q}\tilde{q}$ creation as seen in Fig. 43. Radiated jets in the event can degrade the isolation of the leptons and decrease signal. The ISAJET routine decjet.f is modified to exclude jets generated by gluon radiation via the parton shower fragmentation. The effect due to gluon radiation on the acceptance is determined by taking one-half the difference between the acceptance with gluon radiation "on" and the acceptance with gluon radiation "off". This uncertainty varies between 2-10% depending on the squark and gluino masses.

6. Integrated Luminosity

The luminosity is measured by the beam-beam counters (BBC). The BBC is composed of a plane of scintillation counters placed at low angles near the interaction region. The uncertainty of the luminosity measurement in CDF Run I which is almost entirely due to the uncertainty on the BBC normalization is found to be 4.1% [36].

7. Total Systematic Uncertainty

The systematic uncertainty from the sources mentioned above are summed in quadrature. The total systematic uncertainty is $\simeq$ 16%. Figure 44 demonstrates that the

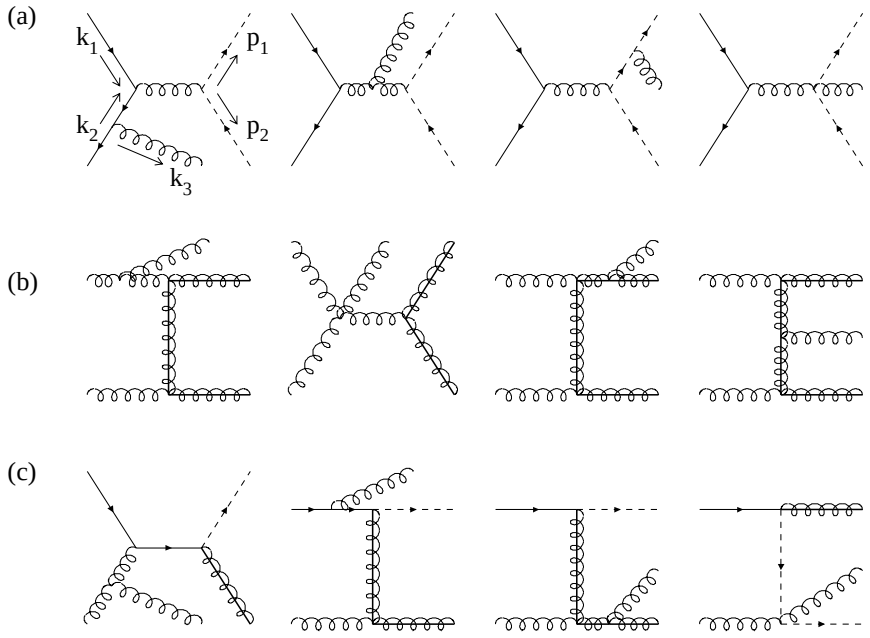

FIG. 43. Feynman diagrams yielding real gluon radiation for (a) $\tilde{q}\tilde{q}$, (b) $\tilde{g}\tilde{g}$, and (c) $\tilde{q}\tilde{g}$ production are presented to demonstrate the effects due to initial state and final state radiation.

systematic uncertainty is roughly flat with gluino mass. The uncertainties are summarized as a function of gluino mass for $M_{\tilde{q}} \gg M_{\tilde{g}}$ and $M_{\tilde{q}} \simeq M_{\tilde{g}}$ in Tables XX and XXI, respectively.

F. **Limits**

Limits on the production of $\tilde{g}\tilde{g}$, $\tilde{g}\tilde{q}$, $\tilde{q}\tilde{q}$, and $\tilde{q}\bar{\tilde{q}}$ have been determined for the dilepton channel for five degenerate squark masses. The limits are calculated at the 95% confidence level (see Appendix F). The mass limit is determined from the intersection of the NLO cross-section (for $\tilde{g}\tilde{g}$, $\tilde{g}\tilde{q}$, $\tilde{q}\tilde{q}$, and $\tilde{q}\bar{\tilde{q}}$) times dilepton (ee, $e\mu$, and $\mu\mu$) branching ratio ($\sigma^{NLO} \cdot Br_{2\ell}$) with the 95% confidence level curve. The NLO cross-section is calculated from PROSPINO[70] (CTEQ3M [71]). The dilepton branching ratio is evaluated using ISAJET 7.20[61] (CTEQ3L[71]).

TABLE XX. The CDF preliminary estimate of total uncertainty on the total efficiency is presented as a function of $M_{\tilde{g}}$ for $M_{\tilde{q}} \gg M_{\tilde{g}}$ ($\tan\beta = 2$ and $\mu = -800$ GeV/c^2).

	$M_{\tilde{g}}$ (GeV/c^2)			
	160	180	200	220
Lepton Isolation	0.108	0.110	0.106	0.109
Gluon Radiation	0.0140	0.0540	0.0370	0.0500
Lepton ID	0.0241	0.0227	0.0238	0.0255
Luminosity	0.0410	0.0410	0.0410	0.0410
Trigger	0.0218	0.0406	0.0304	0.0341
Jet Energy Scale	0.0348	0.0479	0.0271	0.0166
MC Statistics	0.096	0.143	0.128	0.199
Total	0.159	0.204	0.181	0.240

TABLE XXI. The CDF preliminary estimate of total uncertainty on the total efficiency is presented as a function of $M_{\tilde{g}}$ for $M_{\tilde{q}} \simeq M_{\tilde{g}}$ ($\tan\beta = 2$ and $\mu = -800$ GeV/c^2).

	$M_{\tilde{g}}$ (GeV/c^2)			
	220	240	260	280
Lepton Isolation	0.109	0.108	0.103	0.116
Gluon Radiation	0.0976	0.0753	0.0737	0.0316
Lepton ID	0.0241	0.0228	0.0256	0.0297
Trigger	0.0303	0.0393	0.0411	0.0426
Luminosity	0.0410	0.0410	0.0410	0.0410
Jet Energy Scale	0.0114	0.0086	0.0060	0.0100
MC Statistics	0.0500	0.148	0.250	0.308
Total	0.165	0.207	0.288	0.338

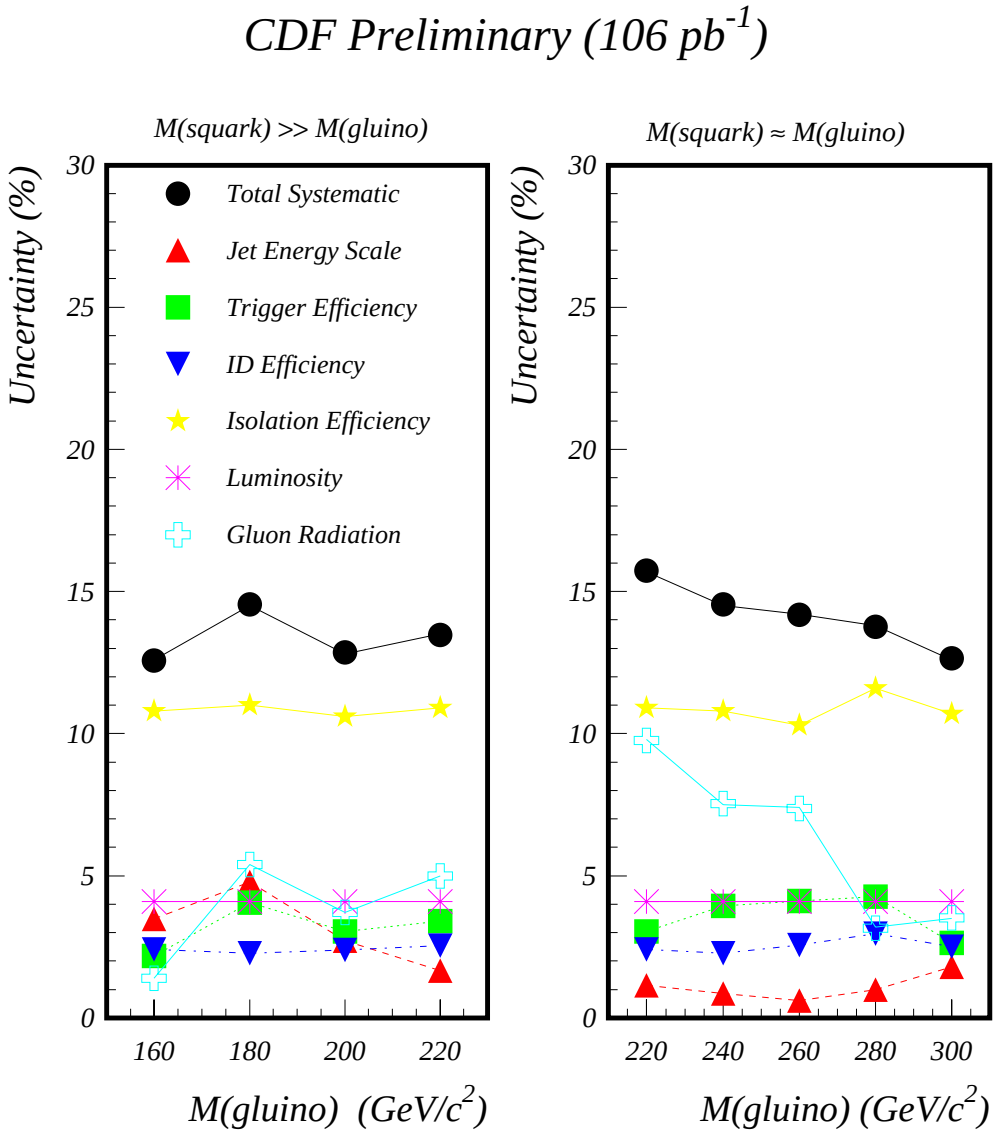

FIG. 44. Systematic uncertainties are displayed as a function of gluino mass (for $\tan\beta = 2$ and $\mu = -800$ GeV/c^2). Here, the total systematic uncertainty is seen to be $\simeq 16\%$ regardless of gluino mass. This is due, for the most part, to the contribution from the uncertainties due to the lepton isolation efficiency and gluon radiation.

Figure 45 shows the limit for this region ($\mu = -800$ GeV/c^2, $\tan\beta = 2$). It is possible to exclude $M(\tilde{g}) < 225$ GeV/c^2 for $M(\tilde{g}) \simeq M(\tilde{q})$ and $M(\tilde{g}) < 169$ GeV/c^2 for regions independent of the squark mass for $Q^2 = m^2$. If theoretical uncertainties are included, the mass limits for the gluino are lower: $M(\tilde{g}) > 218$ GeV/c^2 ($M(\tilde{g}) \simeq M(\tilde{q})$) and $M(\tilde{g}) > 163$ GeV/c^2 ($M(\tilde{q}) \gg M(\tilde{g})$).

1. **Squark-Gluino Mass Plane**

Mass limits for gluinos and squarks have been set in a squark-gluino mass plane since the gluino and squark masses are independent parameters in Supersymmetry. The limit in this analysis is compared with those set by other experiments. The limit at the 95% C.L. in the squark-gluino mass plane for $\mu = -800$ GeV, $\tan\beta = 2$, and $Q^2 = m^2$ is shown in Fig. 46. The region of sensitivity increases near the diagonal ($M_{\tilde{g}} = M_{\tilde{q}}$) because the sleptons become lighter and enhance the branching ratio to dileptons.

2. **Higgsino Mixing Parameter**

Since the value of the Higgsino mixing parameter (μ) is an independent parameter, the limit for the mass of gluino has been examined for different values of μ (both positive and negative). For the study of this sensitivity, $\tan\beta$ has been fixed to a value of 2 and the energy scale, Q^2, was taken at m^2 (where $m = M_{\tilde{g}}$ for $\tilde{g}\tilde{g}$ production, $m = M_{\tilde{q}}$ for $\tilde{q}\tilde{q}$ production, and $m = \frac{1}{2}(M_{\tilde{g}} + M_{\tilde{q}})$ for $\tilde{q}\tilde{g}$ production. One can see in Fig. 47 that the mass limit is independent as a function of μ.

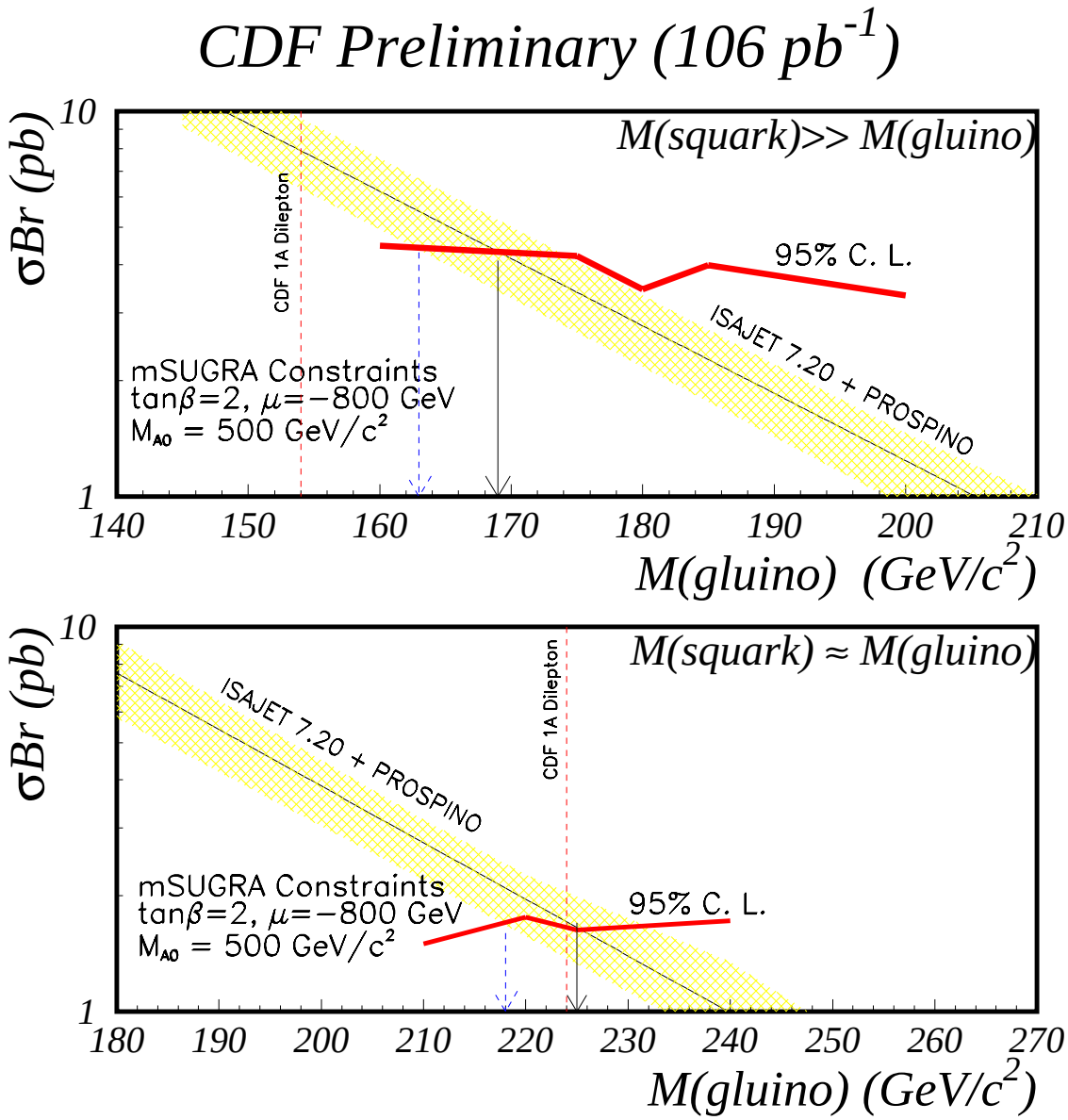

FIG. 45. The production limit is presented as a function of gluino mass from which the mass limit is derived. The solid arrow denotes the limit at $Q^2 = m^2$. The dashed arrow indicates the limit incorporating the shaded theoretical uncertainty. The NLO cross-section (σ) is calculated from PROSPINO[70](CTEQ3M [71]). The dilepton branching ratio (Br) is evaluated using ISAJET 7.20[61] (CTEQ3L[71]).

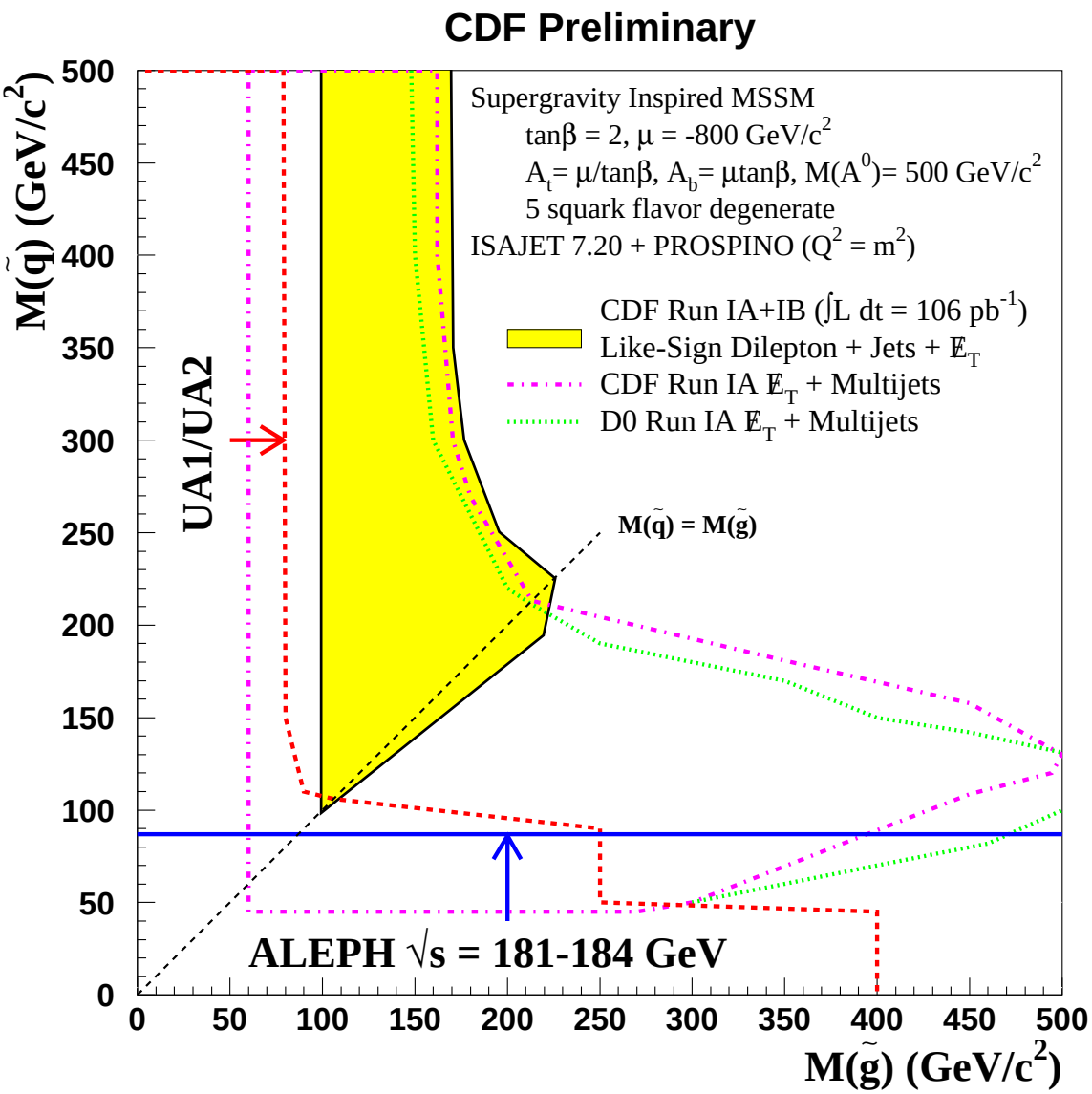

FIG. 46. The limit at the 95% C.L. is displayed in the squark-gluino mass plane. Here, the contour is shaded where more than 3.2 events are expected from the ISAJET 7.20 [61] (CTEQ3L [71]) Monte Carlo simulations for $\tan\beta = 2$ and $\mu = -800$ GeV for a supergravity inspired MSSM ($Q^2 = m^2$). Note that the cross-section for $\tilde{g}\tilde{g}$, $\tilde{g}\tilde{q}$, and $\tilde{q}\tilde{q}$ has been raised to NLO using PROSPINO [70] (CTEQ3M [71]). The limits have been set at the renormalization and factorization scale, $Q^2 = m^2$.

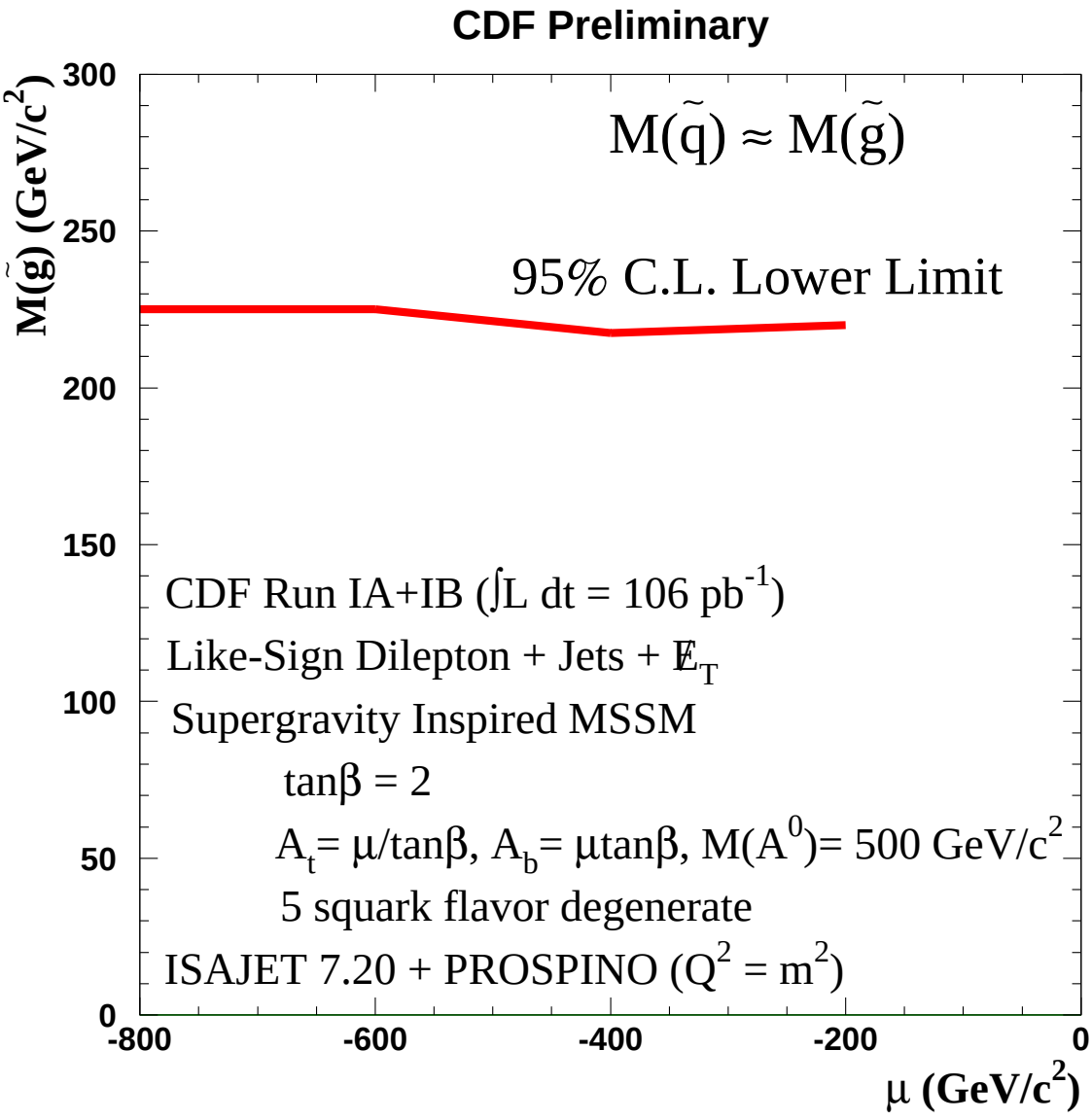

FIG. 47. The gluino mass limit is shown as a function of the Higgsino mixing parameter using ISAJET 7.20 [61] (CTEQ3L [71]) with $\tan\beta = 2$. One can see that the choice of μ does not affect the limit greatly.

CHAPTER VII

CONCLUSION

A search for like-sign dilepton events with two or more jets and large missing missing transverse energy has been performed using 106 pb^{-1} of dilepton data collected at CDF. After all cuts, no events have been found. A 95% confidence level limit is thus determined for the gluino mass (assuming five degenerate squark masses):

$$\begin{aligned} M(\tilde{g}) &> 169 \text{ GeV}/c^2 \quad \text{for M}(\tilde{g}) < \text{M}(\tilde{q}) \text{ and } Q^2 = m^2 \\ M(\tilde{g}) &> 225 \text{ GeV}/c^2 \quad \text{for M}(\tilde{g}) = \text{M}(\tilde{q}) \text{ and } Q^2 = m^2 \end{aligned}$$

with $\tan\beta = 2.0$, $\mu = -800$ GeV/c^2, $M(A^0) = 500$ GeV/c^2. It has also been determined that the choice of the value of the Higgsino mixing parameter (μ) affects the limit weakly.

Although no supersymmetric signal was detected in this collider run, it is encouraging to note that the next Fermilab collider run should yield twenty times the data of Run I at a slightly higher center-of-mass energy ($\sqrt{s} = 2$ TeV). Furthermore, both the CDF and D0 detectors have been improved extensively in order to study this and other supersymmetric signatures. The like-sign dilepton analysis which is nearly background free can be performed at each experiment to determine if strongly produced supersymmetric particles such as gluinos and squarks exist. Should Supersymmetry be observed, this will represent a major step forward in the ultimate unification of the four fundamental forces into a "Theory of Everything".

REFERENCES

[1] D. V. Volkov and V. P. Akulov, Phys. Lett. **46B**, 109 (1973); J. Wess and B. Zumino, Nucl. Phys. B **70**, 39 (1974).

[2] H. P. Nilles, Phys. Rep. **110**, 1 (1984); H. E. Haber and G. L. Kane, Phys. Rep. **117**, 75 (1985).

[3] A. H. Chamseddine, R. Arnowitt, and P. Nath, Phys. Rev. Lett. **49**, 970 (1982); R. Barbieri, S. Ferrora, and C. A. Savoy, Phys. Lett. B **119**, 343 (1982); L. Hall, J. Lykken, and S. Weinberg, Phys. Rev. D **27**, 2359 (1983). For recent reviews, see R. Arnowitt and P. Nath, in *Proceedings of the VIIth J. A. Swieca Summer School, Campos de Jordao, Brazil, 1993*, edited by O.J.P. Eboli and V.O. Rivelles (World Scientific, Singapore, 1994), p. 3; J.L. Lopez, hep-ph/9601208 (1996); Rep. Prog. Phys. **59**, 819 (1996).

[4] P. Langacker, in *Proceedings of the 1st International Symposium on Particles, Strings and Cosmology, Boston, 1990*, edited by P. Nath and S. Reucroft (World Scientific, Singapore, 1991), p. 237; J. Ellis, S. Kelley, and D. V. Nanopoulos, Phys. Lett. B **249**, 441 (1990); U. Amaldi, W. de Boer, and H. Fürstenau, Phys. Lett. B **260**, 447 (1991); P. Langacker and M.-X. Luo, Phys. Rev. D **44**, 817 (1991).

[5] R. Arnowitt, private communication.

[6] J. Ellis and S. Rudaz, Phys. Lett. **128B**, 248 (1983).

[7] H. Baer *et al.*, Phys. Rev. D **47**, 2739 (1992); M. Drees and M. Nojiri, Nucl. Phys. B **369**, 54 (1992).

[8] W. Beenakker, R. Höpker, M. Spira, and P. Zerwas, Nucl. Phys. B **492**, 51 (1997).

[9] UA1 Collaboration, C. Albajar *et al.*, Phys. Lett. B **198**, 261 (1987).

[10] UA2 Collaboration, J. Alitti *et al.*, Phys. Lett. B **235**, 363 (1990).

[11] ALEPH Collaboration, R. Barate, *et al.*, Phys. Lett. B **434**, 189 (1998).

[12] CDF Collaboration, F. Abe *et al.*, Phys. Rev. Lett. **69**, 3439 (1992).

[13] CDF Collaboration, F. Abe *et al.*, Phys. Rev. D **56** (Rapid Communications), 1357 (1997).

[14] D0 Collaboration, S. Abachi *et al.*, Phys. Rev. Lett. **75**, 618 (1995).

[15] H. Baer, J. Ellis, G. Gelmini, D. Nanopoulos, and X. Tata, Phys. Lett. **161B**, 175 (1985); G. Gamberini, Z. Phys. C **30**, 605 (1986).

[16] H. Baer, V. Barger, D. Karatas, and X. Tata, Phys. Rev. D **36**, 96 (1987).

[17] H. Baer *et al.*, Phys. Rev. D **48**, 2978 (1993); H. Baer, X. Tata, and J. Woodside, Phys. Rev. D **45**, 142 (1992).

[18] H. Haber, in *Proceedings of the International Workshop on Supersymmetry and Unification of Fundamental Interactions, SUSY 93, Boston, 1993*, edited by P. Nath (World Scientific, Singapore, 1993), p. 373.

[19] D. Cline, P. McIntyre, F. Mills, and C. Rubbia, in *Proceedings of the International Neutrino Conference, Aachen, 1976*, edited by H. Faissner, H. Reithler, and P. Zerwas (Vieweg, Braunschweig, 1977), p. 683; Print-76-0840 (Harvard), 1976 (unpublished); R. Wilson, "The Tevatron", FERMILAB-TM-0763, 1978 (unpublished).

[20] UA1 Collaboration, G. Arnison *et al.*, Phys. Lett. B **122** 103 (1983).

[21] CDF Collaboration, F. Abe *et al.*, Phys. Rev. Lett. **73** 225 (1994).

[22] D0 Collaboration, S. Abachi *et al.*, Phys. Rev. Lett. **74** 2632 (1995).

[23] K. Desler and D. A. Edwards, Eur. Phys. C. **3**, 1-4, 138 (1998).

[24] CDF Collaboration, F. Abe *et al.*, Nucl. Instrum. and Methods Phys. Res., Sect. A **271**, 387 (1988).

[25] F. Bedeschi *et al.*, Nucl. Instrum. and Methods Phys. Res., Sect. A **268**, 50 (1988).

[26] F. Snider *et al.*, Nucl. Instrum. and Methods Phys. Res., Sect. A **268**, 75 (1988).

[27] P. Azzi *et al.*, Nucl. Instrum. and Methods Phys. Res., Sect. A **360**, 137 (1995); D. Amidei *et al. ibid.*, **350**, 73 (1994).

[28] L. Balka *et al.*, Nucl. Instrum. and Methods Phys. Res., Sect. A **267**, 272 (1988).

[29] S Bertolucci *et al.*, Nucl. Instrum. and Methods Phys. Res., Sect. A **267**, 301 (1988).

[30] Y. Fukui *et al.*, Nucl. Instrum. and Methods Phys. Res., Sect. A **267**, 280 (1988).

[31] C. Haber *et al.*, in *Proceedings of the Gas Sampling Calorimeter 2nd Workshop, Fermilab, 1985*, edited by P. Hale, J. Perrington, D. Jovanovic, and R. Fenner (Fermilab, Batavia, Illinois, 1985), p. 74.

[32] G. Brandenburg *et al.*, Nucl. Instrum. and Methods Phys. Res., Sect A **267**, 257 (1988).

[33] S. Cihangir *et al.*, Nucl. Instrum. and Methods Phys. Res., Sect A **267**, 249 (1988).

[34] J. Lu, M. S. thesis, Texas A&M University, 1995.

[35] G. Ascoli *et al.*, Nucl. Instrum. and Methods Phys. Res., Sect A **268**, 33 (1988).

[36] D. Cronin-Hennessy and A. Beretvas, CDF Note 4721, 1998 (unpublished).

[37] D. Amidei *et al.*, Nucl. Instrum. and Methods Phys. Res., Sect A **269**, 51 (1988).

[38] J. Carroll *et al.*, Nucl. Instrum. and Methods Phys. Res., Sect A **300**, 552 (1991).

[39] S. Kopp, CDF Note 2391, 1993 (unpublished).

[40] G. Ascoli *et al.*, Nucl. Instrum. and Methods Phys. Res., Sect A **269**, 63 (1988).

[41] T. LeCompte and W. Sakumoto, CDF Note 3028, 1995 (unpublished).

[42] G. W. Foster *et al.*, Nucl. Instrum. and Methods Phys. Res., Sect A **269**, 93 (1988).

[43] K. Byrum and A. B. Wicklund, CDF Note 3665, 1996 (unpublished).

[44] W. Taylor, K. Byrum, and P. Sinervo, CDF Note 4691, 1998 (unpublished).

[45] W. Sakumoto, *et al.*, CDF Note 4561, 1999 (unpublished).

[46] A. Scott, J. Hauser, and D. Saltzberg, CDF Note 4894, 1999 (unpublished).

[47] J. Olsen, Ph.D. thesis, University of Wisconsin, 1998.

[48] S. Pappas and J. Lewis, CDF Note 3070, 1995 (unpublished); S. Pappas, J. Lewis, and G. Michail, CDF Note 4076, 1997 (unpublished); S. Pappas, CDF Note 3537, 1996 (unpublished).

[49] J. Lewis, CDF Note 3130, 1995 (unpublished).

[50] J. Done *et al.*, CDF Note 4017, 1999 (unpublished).

[51] Y. Kato, Ph.D. thesis, Osaka City University, 1996.

[52] N. L. Bruner, CDF Note 4700, 1998 (unpublished).

[53] T. LeCompte, T. Liss, and A. Martin, CDF Note 3041, 1995 (unpublished).

[54] M. Shapiro *et al.*, CDF Note 1810, 1992 (unpublished).

[55] CERN Program Library Long Writeup W5013, 1993 (unpublished); http://wwwinfo.cern.ch/asdoc/geant_html3/geantall.html.

[56] CDF Collaboration, F. Abe *et al.*, Phys. Rev. Lett. **76**, 2006 (1996).

[57] CDF Collaboration, F. Abe *et al.*, Phys. Rev. Lett.**77**, 448 (1996).

[58] R. Keup, Ph.D. thesis, University of Illinois, 1995.

[59] CDF Collaboration, F. Abe *et al.*, Phys. Rev. D **59**:052002, (1999).

[60] D. Glenzinski, Ph.D. thesis, Johns Hopkins University, 1995.

[61] H. Baer, F. E. Paige, S. D. Protopopescu, and X. Tata, in *Proceedings of the Workshop on Physics at Current Accelerators and the Supercolliders, Argonne, Illinois, 1993*, edited by J. Hewett, A. White, and D. Zeppenfeld (Argonne, Illinois, 1993) p. 703; F. Paige and S.D. Protopopescu, BNL Report No. 38034, 1986 (unpublished).

[62] S. Lammel, CDF Note 2889, 1996 (unpublished); http://www-cdf.fnal.gov/internal/physics/exotic/susy/susy.html.

[63] M. Kruse, Ph.D. thesis, Purdue University, 1996.

[64] D. Gerdes, CDF Note 2903, 1994 (unpublished).

[65] J. Done, M. Chertok, T. Kamon, and S. Lammel, CDF Note 4447, 1998 (unpublished).

[66] M. Krasberg and T. J. LeCompte, CDF Note 2032, 1993 (unpublished).

[67] CDF Collaboration, F. Abe *et al.*, Phys. Rev. Lett. **80** 5275 (1998).

[68] A.B. Carter and A.I. Sanda, Phys. Rev. Lett. **45**, 952 (1980); A.B. Carter and A.I. Sanda, Phys. Rev. D **23**, 1567 (1981); I.I. Bigi and A.I. Sanda, Nucl. Phys. **B193**, 85 (1981); I.I. Bigi and A.I. Sanda, Nucl. Phys. **B281**, 41 (1987).

[69] H. Mitsushio, Ph.D. thesis, University of Tsukuba, 1996; H. Mitsushio, I. Nakano, and Y. Seiya, CDF Note 3042, 1995 (unpublished).

[70] W. Beenakker, R. Höpker, M. Spira, and P.M. Zerwas, hep-ph/9611232, (1996);http://home.cern.ch/m/mspira/www/.

[71] CTEQ Collaboration, H. L. Lai *et al.*, Phys. Rev. D **51**, 4763 (1995).

[72] G. Sterman and S. Weinberg, Phys. Rev. Lett. **39**, 1436 (1977).

[73] L. Keeble, Ph.D. thesis, Texas A&M University, 1992.

[74] N. Eddy, CDF Note 3534, 1996 (unpublished).

[75] CDF Collaboration, F. Abe *et al.*, Phys. Rev. Lett. **81**, 5742 (1998).

[76] D. Glenzinski, Ph.D. thesis, Johns Hopkins University, 1995.

[77] H. Kim, CDF Note 4124, 1997 (unpublished).

[78] M. Spiropulu, CDF Note 4512, 1998 (unpublished); F. Keyvan, CDF Note 3391, 1996 (unpublished).

[79] C. Balazs and C.-P. Yuan, Phys. Rev. D **56**:5558-5583, 1997; http://pilot.msu.edu/user/balazscs/ResBos/

[80] CDF Collaboration, F. Abe *et al.*, Phys. Rev. D **49**, 1 (1994).

[81] CDF Collaboration, F. Abe *et al.*, Phys. Rev. Lett. 80, 2773 (1998).

[82] CDF Collaboration, F. Abe *et al.*, Phys. Rev. Lett.**78** 4536, (1997); J. Ohnemus, Phys. Rev. D **44** (1991) 1403.

[83] J. Ohnemus, Phys. Rev. D **44** (1991) 3477.

[84] J. Ohnemus and J. Owens, Phys. Rev. D **43** (1991) 3626.

[85] R. Cousins, Am. J. Phys. 63, 398 (1995); T. Huber *et al.*, Phys. Rev. D **41**, 2709 (1990); G. Zech, Nucl. Instrum. and Methods Phys. Res., Sect A **277**, 608 (1989).

[86] J. Conway and K. Maeshima, CDF Note 4476, 1998 (unpublished).

APPENDIX A

CDF AUTHOR LIST

T. Affolder,[21] H. Akimoto,[42] A. Akopian,[35] M. G. Albrow,[10] P. Amaral,[7] S. R. Amendolia,[31] D. Amidei,[24] J. Antos,[1] G. Apollinari,[35] T. Arisawa,[42] T. Asakawa,[40] W. Ashmanskas,[7] M. Atac,[10] P. Azzi-Bacchetta,[29] N. Bacchetta,[29] M. W. Bailey,[26] S. Bailey,[14] P. de Barbaro,[34] A. Barbaro-Galtieri,[21] V. E. Barnes,[33] B. A. Barnett,[17] M. Barone,[12] G. Bauer,[22] F. Bedeschi,[31] S. Belforte,[39] G. Bellettini,[31] J. Bellinger,[43] D. Benjamin,[9] J. Bensinger,[4] A. Beretvas,[10] J. P. Berge,[10] J. Berryhill,[7] S. Bertolucci,[12] B. Bevensee,[30] A. Bhatti,[35] C. Bigongiari,[31] M. Binkley,[10] D. Bisello,[29] R. E. Blair,[2] C. Blocker,[4] K. Bloom,[24] S. Blusk,[34] A. Bocci,[31] A. Bodek,[34] W. Bokhari,[30] G. Bolla,[33] Y. Bonushkin,[5] D. Bortoletto,[33] J. Boudreau,[32] A. Brandl,[26] S. van den Brink,[17] C. Bromberg,[25] N. Bruner,[26] E. Buckley-Geer,[10] J. Budagov,[8] H. S. Budd,[34] K. Burkett,[14] G. Busetto,[29] A. Byon-Wagner,[10] K. L. Byrum,[2] M. Campbell,[24] A. Caner,[31] W. Carithers,[21] J. Carlson,[24] D. Carlsmith,[43] J. Cassada,[34] A. Castro,[29] D. Cauz,[39] A. Cerri,[31] P. S. Chang,[1] P. T. Chang,[1] J. Chapman,[24] C. Chen,[30] Y. C. Chen,[1] M. -T. Cheng,[1] M. Chertok,[37] G. Chiarelli,[31] I. Chirikov-Zorin,[8] G. Chlachidze,[8] F. Chlebana,[10] L. Christofek,[16] M. L. Chu,[1] S. Cihangir,[10] C. I. Ciobanu,[27] A. G. Clark,[13] M. Cobal,[31] E. Cocca,[31] A. Connolly,[21] J. Conway,[36] J. Cooper,[10] M. Cordelli,[12] J. Guimaraes da Costa,[24] D. Costanzo,[31] D. Cronin-Hennessy,[9] R. Cropp,[23] R. Culbertson,[7] D. Dagenhart,[41] F. DeJongh,[10] S. Dell'Agnello,[12] M. Dell'Orso,[31] R. Demina,[10] L. Demortier,[35] M. Deninno,[3] P. F. Derwent,[10] T. Devlin,[36] J. R. Dittmann,[10] S. Donati,[31] J. Done,[37] T. Dorigo,[14] N. Eddy,[16] K. Einsweiler,[21] J. E. Elias,[10] E. Engels, Jr.,[32]

W. Erdmann,[10] D. Errede,[16] S. Errede,[16] Q. Fan,[34] R. G. Feild,[44] C. Ferretti,[31] I. Fiori,[3] B. Flaugher,[10] G. W. Foster,[10] M. Franklin,[14] J. Freeman,[10] J. Friedman,[22] Y. Fukui,[20] S. Gadomski,[23] S. Galeotti,[31] M. Gallinaro,[35] T. Gao,[30] M. Garcia-Sciveres,[21] A. F. Garfinkel,[33] P. Gatti,[29] C. Gay,[44] S. Geer,[10] D. W. Gerdes,[24] P. Giannetti,[31] P. Giromini,[12] V. Glagolev,[8] M. Gold,[26] J. Goldstein,[10] A. Gordon,[14] A. T. Goshaw,[9] Y. Gotra,[32] K. Goulianos,[35] H. Grassmann,[39] C. Green,[33] L. Groer,[36] C. Grosso-Pilcher,[7] M. Guenther,[33] G. Guillian,[24] R. S. Guo,[1] C. Haber,[21] E. Hafen,[22] S. R. Hahn,[10] C. Hall,[14] T. Handa,[15] R. Handler,[43] W. Hao,[38] F. Happacher,[12] K. Hara,[40] A. D. Hardman,[33] R. M. Harris,[10] F. Hartmann,[18] K. Hatakeyama,[35] J. Hauser,[5] J. Heinrich,[30] A. Heiss,[18] B. Hinrichsen,[23] K. D. Hoffman,[33] C. Holck,[30] R. Hollebeek,[30] L. Holloway,[16] R. Hughes,[27] J. Huston,[25] J. Huth,[14] H. Ikeda,[40] M. Incagli,[31] J. Incandela,[10] G. Introzzi,[31] J. Iwai,[42] Y. Iwata,[15] E. James,[24] H. Jensen,[10] M. Jones,[30] U. Joshi,[10] H. Kambara,[13] T. Kamon,[37] T. Kaneko,[40] K. Karr,[41] H. Kasha,[44] Y. Kato,[28] T. A. Keaffaber,[33] K. Kelley,[22] M. Kelly,[24] R. D. Kennedy,[10] R. Kephart,[10] D. Khazins,[9] T. Kikuchi,[40] M. Kirk,[4] B. J. Kim,[19] H. S. Kim,[23] S. H. Kim,[40] Y. K. Kim,[21] L. Kirsch,[4] S. Klimenko,[11] D. Knoblauch,[18] P. Koehn,[27] A. Köngeter,[18] K. Kondo,[42] J. Konigsberg,[11] K. Kordas,[23] A. Korytov,[11] E. Kovacs,[2] J. Kroll,[30] M. Kruse,[34] S. E. Kuhlmann,[2] K. Kurino,[15] T. Kuwabara,[40] A. T. Laasanen,[33] N. Lai,[7] S. Lami,[35] S. Lammel,[10] J. I. Lamoureux,[4] M. Lancaster,[21] G. Latino,[31] T. LeCompte,[2] A. M. Lee IV,[9] S. Leone,[31] J. D. Lewis,[10] M. Lindgren,[5] T. M. Liss,[16] J. B. Liu,[34] Y. C. Liu,[1] N. Lockyer,[30] M. Loreti,[29] D. Lucchesi,[29] P. Lukens,[10] S. Lusin,[43] J. Lys,[21] R. Madrak,[14] K. Maeshima,[10] P. Maksimovic,[14] L. Malferrari,[3] M. Mangano,[31] M. Mariotti,[29] G. Martignon,[29] A. Martin,[44] J. A. J. Matthews,[26] P. Mazzanti,[3] K. S. McFarland,[34] P. McIntyre,[37] E. McKigney,[30] M. Menguzzato,[29] A. Menzione,[31] E. Meschi,[31] C. Mesropian,[35] C. Miao,[24] T. Miao,[10] R. Miller,[25] J. S. Miller,[24] H. Minato,[40] S. Miscetti,[12] M. Mishina,[20] N. Moggi,[31]

E. Moore,[26] R. Moore,[24] Y. Morita,[20] A. Mukherjee,[10] T. Muller,[18] A. Munar,[31] P. Murat,[31] S. Murgia,[25] M. Musy,[39] J. Nachtman,[5] S. Nahn,[44] H. Nakada,[40] T. Nakaya,[7] I. Nakano,[15] C. Nelson,[10] D. Neuberger,[18] C. Newman-Holmes,[10] C.-Y. P. Ngan,[22] P. Nicolaidi,[39] H. Niu,[4] L. Nodulman,[2] A. Nomerotski,[11] S. H. Oh,[9] T. Ohmoto,[15] T. Ohsugi,[15] R. Oishi,[40] T. Okusawa,[28] J. Olsen,[43] C. Pagliarone,[31] F. Palmonari,[31] R. Paoletti,[31] V. Papadimitriou,[38] S. P. Pappas,[44] A. Parri,[12] D. Partos,[4] J. Patrick,[10] G. Pauletta,[39] M. Paulini,[21] A. Perazzo,[31] L. Pescara,[29] T. J. Phillips,[9] G. Piacentino,[31] K. T. Pitts,[10] R. Plunkett,[10] A. Pompos,[33] L. Pondrom,[43] G. Pope,[32] F. Prokoshin,[8] J. Proudfoot,[2] F. Ptohos,[12] G. Punzi,[31] K. Ragan,[23] D. Reher,[21] A. Ribon,[29] F. Rimondi,[3] L. Ristori,[31] W. J. Robertson,[9] A. Robinson,[23] T. Rodrigo,[6] S. Rolli,[41] L. Rosenson,[22] R. Roser,[10] R. Rossin,[29] W. K. Sakumoto,[34] D. Saltzberg,[5] A. Sansoni,[12] L. Santi,[39] H. Sato,[40] P. Savard,[23] P. Schlabach,[10] E. E. Schmidt,[10] M. P. Schmidt,[44] M. Schmitt,[14] L. Scodellaro,[29] A. Scott,[5] A. Scribano,[31] S. Segler,[10] S. Seidel,[26] Y. Seiya,[40] A. Semenov,[8] F. Semeria,[3] T. Shah,[22] M. D. Shapiro,[21] P. F. Shepard,[32] T. Shibayama,[40] M. Shimojima,[40] M. Shochet,[7] J. Siegrist,[21] G. Signorelli,[31] A. Sill,[38] P. Sinervo,[23] P. Singh,[16] A. J. Slaughter,[44] K. Sliwa,[41] C. Smith,[17] F. D. Snider,[10] A. Solodsky,[35] J. Spalding,[10] T. Speer,[13] P. Sphicas,[22] F. Spinella,[31] M. Spiropulu,[14] L. Spiegel,[10] L. Stanco,[29] J. Steele,[43] A. Stefanini,[31] J. Strologas,[16] F. Strumia, [13] D. Stuart,[10] K. Sumorok,[22] T. Suzuki,[40] R. Takashima,[15] K. Takikawa,[40] M. Tanaka,[40] T. Takano,[28] B. Tannenbaum,[5] W. Taylor,[23] M. Tecchio,[24] P. K. Teng,[1] K. Terashi,[40] S. Tether,[22] D. Theriot,[10] R. Thurman-Keup,[2] P. Tipton,[34] S. Tkaczyk,[10] K. Tollefson,[34] A. Tollestrup,[10] H. Toyoda,[28] W. Trischuk,[23] J. F. de Troconiz,[14] S. Truitt,[24] J. Tseng,[22] N. Turini,[31] F. Ukegawa,[40] J. Valls,[36] S. Vejcik III,[10] G. Velev,[31] R. Vidal,[10] R. Vilar,[6] I. Vologouev,[21] D. Vucinic,[22] R. G. Wagner,[2] R. L. Wagner,[10] J. Wahl,[7] N. B. Wallace,[36] A. M. Walsh,[36] C. Wang,[9] C. H. Wang,[1] M. J. Wang,[1] T. Watanabe,[40]

T. Watts,[36] R. Webb,[37] H. Wenzel,[18] W. C. Wester III,[10] A. B. Wicklund,[2] E. Wicklund,[10] H. H. Williams,[30] P. Wilson,[10] B. L. Winer,[27] D. Winn,[24] S. Wolbers,[10] D. Wolinski,[24] J. Wolinski,[25] S. Worm,[26] X. Wu,[13] J. Wyss,[31] A. Yagil,[10] W. Yao,[21] G. P. Yeh,[10] P. Yeh,[1] J. Yoh,[10] C. Yosef,[25] T. Yoshida,[28] I. Yu,[19] S. Yu,[30] A. Zanetti,[39] F. Zetti,[21] and S. Zucchelli[3]

(CDF Collaboration)

[1] *Institute of Physics, Academia Sinica, Taipei, Taiwan 11529, Republic of China*

[2] *Argonne National Laboratory, Argonne, Illinois 60439*

[3] *Istituto Nazionale di Fisica Nucleare, University of Bologna, I-40127 Bologna, Italy*

[4] *Brandeis University, Waltham, Massachusetts 02254*

[5] *University of California at Los Angeles, Los Angeles, California 90024*

[6] *Instituto de Fisica de Cantabria, University of Cantabria, 39005 Santander, Spain*

[7] *Enrico Fermi Institute, University of Chicago, Chicago, Illinois 60637*

[8] *Joint Institute for Nuclear Research, RU-141980 Dubna, Russia*

[9] *Duke University, Durham, North Carolina 27708*

[10] *Fermi National Accelerator Laboratory, Batavia, Illinois 60510*

[11] *University of Florida, Gainesville, Florida 32611*

[12] *Laboratori Nazionali di Frascati, Istituto Nazionale di Fisica Nucleare, I-00044 Frascati, Italy*

[13] *University of Geneva, CH-1211 Geneva 4, Switzerland*

[14] *Harvard University, Cambridge, Massachusetts 02138*

[15] *Hiroshima University, Higashi-Hiroshima 724, Japan*

[16] *University of Illinois, Urbana, Illinois 61801*

[17] *The Johns Hopkins University, Baltimore, Maryland 21218*

[18] *Institut für Experimentelle Kernphysik, Universität Karlsruhe, 76128 Karlsruhe, Germany*

[19] *Korean Hadron Collider Laboratory: Kyungpook National University, Taegu 702-701; Seoul National University, Seoul 151-742; and SungKyunKwan University, Suwon 440-746; Korea*

[20] *High Energy Accelerator Research Organization (KEK), Tsukuba, Ibaraki 305, Japan*

[21] *Ernest Orlando Lawrence Berkeley National Laboratory, Berkeley, California 94720*

[22] *Massachusetts Institute of Technology, Cambridge, Massachusetts 02139*

[23] *Institute of Particle Physics: McGill University, Montreal H3A 2T8; and University of Toronto, Toronto M5S 1A7; Canada*

[24] *University of Michigan, Ann Arbor, Michigan 48109*

[25] *Michigan State University, East Lansing, Michigan 48824*

[26] *University of New Mexico, Albuquerque, New Mexico 87131*

[27] *The Ohio State University, Columbus, Ohio 43210*

[28] *Osaka City University, Osaka 588, Japan*

[29] *Universita di Padova, Istituto Nazionale di Fisica Nucleare, Sezione di Padova, I-35131 Padova, Italy*

[30] *University of Pennsylvania, Philadelphia, Pennsylvania 19104*

[31] *Istituto Nazionale di Fisica Nucleare, University and Scuola Normale Superiore of Pisa, I-56100 Pisa, Italy*

[32] *University of Pittsburgh, Pittsburgh, Pennsylvania 15260*

[33] *Purdue University, West Lafayette, Indiana 47907*

[34] *University of Rochester, Rochester, New York 14627*

[35] *Rockefeller University, New York, New York 10021*

[36] *Rutgers University, Piscataway, New Jersey 08855*

[37] *Texas A&M University, College Station, Texas 77843*

[38] *Texas Tech University, Lubbock, Texas 79409*

[39] *Istituto Nazionale di Fisica Nucleare, University of Trieste/ Udine, Italy*

[40] *University of Tsukuba, Tsukuba, Ibaraki 305, Japan*

[41] *Tufts University, Medford, Massachusetts 02155*

[42] *Waseda University, Tokyo 169, Japan*

[43] *University of Wisconsin, Madison, Wisconsin 53706*

[44] *Yale University, New Haven, Connecticut 06520*

APPENDIX B

LEPTON IDENTIFICATION EFFICIENCIES

A. **Introduction**

Efficiencies of lepton identification (ID), photon-conversion removal, "good" CTC track, and cosmic ray removal cuts are studied using Z^0 events from the Run IB inclusive electron and muon data samples. These cuts are used for several SUSY analyses. The results are compared to Run IA results as well as to ISAJET + QFL′ Monte Carlo (MC) results. The results from data are compared to those from Monte Carlo because it is well known that the CDF detector simulation (QFL′) overestimates performance and does not incorporate luminosity or aging effects. It also does not include effects due to multiple interactions. In completing this work, Monte Carlo correction factors for each detector element is provided. The selection cuts for the inclusive electron and muon samples are summarized in Tables XXII and XXIII, respectively.

B. **Method**

Z^0 events are selected from the inclusive electron and muon data samples as well as from the Monte Carlo sample. A 422.7 pb^{-1} Monte Carlo sample of Drell-Yan (Z^0) events is used[62]. The events are generated using ISAJET 7.16 with CTEQ2L structure function and simulated through the CDF detector simulation (QFL′).

The tight lepton (ℓ_1 = CEM or CMUP) with $p_{\rm T}(\ell_1) > 20$ GeV/c is required to

TABLE XXII. Cuts applied to the inclusive electron sample.

Object type	Variable	Cut
CEM	$E_{\rm T}$	$\geq$ 20 GeV
	E/p (corrected)	$\leq$ 1.8
	Had/Em (3×3)	$\leq$ 0.05
	$LSHR$	$\leq$ 0.2
	$\mid \Delta x \mid$	$\leq$ 1.5 cm
	$\mid \Delta z \mid$	$\leq$ 3.0 cm
	χ^2_{strip}	$\leq$ 10.0
	$\mid z_{vertex} \mid$	$\leq$ 60 cm
	$\mid z_{vertex} - z_0^e \mid$	$\leq$ 5 cm (Vertex Class $\geq$ 10)
	Fiducial (FIDELE)	Yes
	Conversion Removal (CONVERT2)[64]	Yes

pass tighter identification cuts[1] than the cuts in Tables XXII and XXIII, $ISO^{cal}_{0.4} < 4$ GeV, fiducial volume cut (CEM), and a photon-conversion removal cut (CEM)[64].

There are no identification cuts for any additional isolated ($ISO^{cal}_{0.4} < 4$ GeV) lepton (ℓ_2) with momentum above 20 GeV/c and separated from the tight lepton ($\Delta R(\ell_1, \ell_2) > 0.4$) originating from the same vertex as the tight lepton ($\mid z_0^{\ell 1} - z_0^{\ell 2} \mid <$ 10 cm) must pass fiducial volume cuts (CEM, PEM, CMIO), and a photon-conversion removal cut (CEM)[64]. The dilepton mass must fall in a specified window ($84 < M(\ell_1, \ell_2) < 96$ GeV/c^2). The dilepton pair is required to be opposite sign except for CEM-PEM events.

The formula for the efficiency of any cut C as applied to CEM or CMUP is given by Eq. B.1.

[1]The tighter cuts for CEM are $E/p < 1.5$, Had/Em < 0.04, $LSHR < 0.1$, $|\Delta x| <$ 1.5 cm, and $|\Delta z| < 2$ cm. Tighter cuts are applied for CMUP muons for the deposited calorimeter energy: EM $<$ 1.5 GeV and Had $<$ 4 GeV and the CTC matching requirements: $\chi^2_{CMU} < 6$, $\chi^2_{CMP} < 6$, $\mid \Delta x(CMU) \mid < 1.5$ cm, OR $\mid \Delta x(CMP) \mid < 3.0$ cm.

TABLE XXIII. Cuts applied to the inclusive muon sample.

Object type	Variable	Cut
	$p_{\rm T}$ (beam constrained)	$\geq$ 20 GeV/c
	EM	$\leq$ 2 GeV
	Had	$\leq$ 6 GeV
	EM+Had	$\geq$ 0.1 GeV
CMUP	d_0 (beam constrained)	$\leq$ 0.3 cm
	$\mid \Delta x \mid$ (CMU)	$\leq$ 2.0 cm
	$\mid \Delta x \mid$ (CMP)	$\leq$ 5.0 cm
	$\mid z_{vertex} \mid$	$\leq$ 60 cm
	$\mid z_{vertex} - z_0^{\mu} \mid$	$\leq$ 5 cm (Vertex Class $\geq$ 10)
	Cosmic Ray Removal (CMCOS [66])	yes

$$\epsilon_C = \frac{N_C + N_{TT}}{N_{tot} + N_{TT}} \pm \sqrt{\frac{(N_C + N_{TT})(N_{tot} - N_C)}{(N_{tot} + N_{TT})^3}}, \tag{B.1}$$

N_{tot} is the total number of events in the sample, N_{TT} is the subset in which both leptons pass "tighter" cuts, and N_C is the subset in which the second-leg leptons pass C, where C can be a single cut or set of cuts. C is assumed to be included in the tighter cuts, *i.e.*, if a lepton passes tighter cuts then it is also guaranteed to pass C. In the case of PEM, CMX, and CMIO cut efficiencies where the first lepton can not be mistaken as the second, the following formula is used :

$$\epsilon_C = \frac{N_C}{N_{tot}} \pm \sqrt{\frac{N_C(N_{tot} - N_C)}{N_{tot}^3}}, \tag{B.2}$$

The Run IB results are reported and compared to the Run IA and Monte Carlo results. Total lepton identification efficiencies are found by applying all cuts. Efficiencies of conversion removal, cosmic ray removal, and "good" CTC track finding are determined requiring the application of all other appropriate identification criteria.

The efficiency of the cut independent of the other cuts is given for Monte Carlo, Run IA, and Run IB.

C. Electron Identification Efficiency

The electron identification efficiency is tabulated for tight central electrons (TCE), loose central electrons (LCE), and plug electrons (PEM). The tight and loose CEM (TCE, LCE) efficiencies are summarized in Tables XXIV and XXV, respectively. The PEM identification efficiencies are summarized in Table XXVI.

TABLE XXIV. Identification efficiency for tight CEM (TCE) electrons using the Z^0 data and MC samples. Conversion removal and "good" CTC track efficiencies are discussed later.

	Efficiency (MC)	Efficiency (IA)	Efficiency (IB)
E/p (raw) ≤ 2.0	0.944±0.003	N/A	0.924±0.005
E/p (corrected) ≤ 2.0	0.943±0.003	0.945±0.009	0.927±0.005
Had/Em ≤ 0.05	0.981±0.002	0.971±0.006	0.968±0.003
$LSHR \leq 0.2$	0.974±0.002	0.982±0.005	0.985±0.002
$\|\Delta x\| \leq 3$ cm	0.977±0.002	0.969±0.007	0.973±0.003
$\|\Delta z\| \leq 5$ cm	0.994±0.001	0.981±0.005	0.996±0.001
$\chi^2_{strip} \leq 10.0$	0.973±0.002	0.955±0.008	0.958±0.004
Total (TCE)	0.888±0.004	0.864±0.013	0.854±0.007

A photon-conversion electron is removed using the CONVERT2 module if the following is satisfied[64]: ($|\cot(\theta)| < 0.06$, $|\Delta(r\text{-}\phi_{separation})| < 0.3$, and -20 cm $< R_c <$ 50 cm) **or** (VTX occupancy < 0.2). These standard CONVERT2 cuts for electrons are applied. The results are summarized in Table XXVII.

If the track associated with the electron is close to an opposite charged track or if the VTX occupancy is less than 20%, then the event is removed as a conversion. The efficiency of this defined cut is independent of pseudorapidity. In the SUSY like-sign dilepton analysis, only the conversion removal for central electrons is used.

TABLE XXV. Identification efficiency for loose CEM (LCE) electrons using the Z^0 data and MC samples. Conversion removal and "good" CTC track efficiencies are discussed later.

	Efficiency (MC)	Efficiency (IA)	Efficiency (IB)
E/p (raw) ≤ 2.0	0.944±0.003	N/A	0.924±0.005
E/p (corrected) ≤ 2.0	0.945±0.003	0.945±0.009	0.927±0.005
Had/Em $\leq 0.055 + 0.045(E/100)$	0.992±0.001	0.995±0.003	0.990±0.002
$LSHR \leq 0.2$	0.974±0.002	0.982±0.005	0.985±0.002
$\|\Delta x\| \leq 3$ cm	0.977±0.002	0.969±0.007	0.973±0.003
$\|\Delta z\| \leq 5$ cm	0.994±0.001	0.981±0.005	0.996±0.001
$\chi^2_{strip} \leq 15.0$	0.988±0.001	0.964±0.007	0.975±0.003
Total (LCE)	0.914±0.003	0.890±0.012	0.888±0.006

TABLE XXVI. Identification efficiency for PEM electrons using the Z^0 data and MC samples. Since the $\chi^2_{3\times3}$ distribution for the MC events is broader, a cut at 9 instead of 3 is applied for MC events.

	Efficiency (MC)	Efficiency (IA)	Efficiency (IB)
Had/Em ≤ 0.1	0.999±0.001	$1.000^{+0.000}_{-0.002}$	0.996±0.002
$\chi^2_{3\times3} \leq 3.0$	0.922±0.004	0.954±0.010	0.956±0.005
VTX Occupancy ≥ 0.5	0.999±0.001	0.937±0.012	0.963±0.005
Total (PEM)	0.924±0.004	0.890±0.012	0.920±0.007

However, efficiencies for plug electrons are listed for sake of completeness. Here, all other electron identification criteria have been applied prior to rejecting conversions.

D. **Muon Identification Efficiency**

The muon identification differs from the top dilepton analysis only due to the matching cuts for the muons. The tight and loose (TCM, LCM) identification efficiencies are summarized in Tables XXVIII and XXIX. A matching cut for CMU/CMP/CMUP muons is applied: CMU (CMP) Δx $<$ 2 cm (5 cm) OR $\chi^2_x(CMU/CMP)$ $<$ 9. "Good" CTC track and cosmic ray removal efficiencies are estimated later in this

TABLE XXVII. Conversion removal efficiency for electrons using the Z^0 data and MC.

	Efficiency (MC)	Efficiency (IA)	Efficiency (IB)
TCE	0.977±0.002	0.955±0.007	0.958±0.004
LCE	0.977±0.002	0.955±0.007	0.958±0.004
PEM	$1.000^{+0.000}_{-0.001}$	0.985±0.009	0.993±0.002

chapter. Totals are found after applying all identification cuts. The loose CMX identification efficiencies are summarized in TableXXX. Note: matching (CMX) refers to $\Delta x(CMX) < 5$ cm OR $\chi^2_x(CMX) < 9$. The CMIO identification efficiencies are summarized in Table XXXI. Muons that could be categorized as cosmic rays have been removed using the routine CMCOS [66]. The cosmic ray flag in the CMUO/CMIO banks (MOCrFl) is determined using this routine. If the flag is set greater than 1, the muon is said to have failed the cosmic ray filter. Table XXXII displays the efficiency of the cut in Monte Carlo as well as in data.

TABLE XXVIII. Identification efficiency for tight CMU/CMP (TCM) muons using the Z^0 sample.

	Efficiency (MC)	Efficiency (IA)	Efficiency (IB)
EM $\leq$ 2.0 GeV	0.989±0.002	0.966±0.015	0.960±0.005
Had $\leq$ 6.0 GeV	0.983±0.002	0.993±0.007	0.969±0.005
EM+Had $\geq$ 0.1 GeV	0.995±0.001	0.993±0.007	0.976±0.005
$d_0 \leq$ 0.5 cm (raw)	0.995±0.001	N/A	0.981±0.004
$d_0 \leq$ 0.2 cm (b. c.)	0.994±0.001	$1.000^{+0.000}_{-0.009}$	0.972±0.004
Matching (CMU or CMP)	0.995±0.001	0.938±0.020	0.983±0.004
Total (TCM)	0.977±0.003	0.903±0.025	0.929±0.007

E. "Good" CTC Track Efficiency

A "good" CTC track is a 3D track found with $\geq$ 3 axial CTC superlayer (SL) hits, $\geq$ 2 stereo SL hits, and $\geq$ 6 total SL hits. Efficiencies of track cuts on the second leg

TABLE XXIX. Identification efficiency for loose CMU/CMP (LCM) muons using the Z^0 sample. Note: matching (CMU or CMP) refers to CMU (CMP) $\Delta x < 2$ cm (5 cm) OR $\chi^2_x(CMU/CMP) < 9$.

	Efficiency (MC)	Efficiency (IA)	Efficiency (IB)
EM $\leq$ 2.0 GeV	0.989±0.002	0.966±0.015	0.960±0.005
Had $\leq$ 6.0 GeV	0.983±0.002	0.993±0.007	0.969±0.005
EM+Had $\geq$ 0.1 GeV	0.995±0.001	0.993±0.007	0.976±0.005
$d_0 \leq$ 0.8 cm (raw)	0.995±0.001	N/A	0.983±0.004
$d_0 \leq$ 0.5 cm (b. c.)	0.994±0.001	$1.000^{+0.000}_{-0.009}$	0.980±0.004
Matching (CMU or CMP)	0.995±0.001	0.938±0.020	0.983±0.004
Total (LCM)	0.976±0.003	0.903±0.025	0.937±0.006

TABLE XXX. Identification efficiency for CMX muons using the Z^0 sample.

	Efficiency (MC)	Efficiency (IA)	Efficiency (IB)
EM $\leq$ 2.0 GeV	0.987±0.003	0.970±0.021	0.969±0.007
Had $\leq$ 6.0 GeV	0.988±0.003	$1.000^{+0.000}_{-0.015}$	0.969±0.007
EM+Had $\geq$ 0.1 GeV	0.999±0.001	$1.000^{+0.000}_{-0.015}$	0.991±0.004
$d_0 \leq$ 0.8 cm (raw)	0.999±0.001	N/A	$1.000^{+0.000}_{-0.001}$
$d_0 \leq$ 0.5 cm (b. c.)	0.999±0.001	$1.000^{+0.000}_{-0.015}$	$1.000^{+0.000}_{-0.001}$
Matching (CMX)	0.999±0.001	0.970±0.021	$1.000^{+0.000}_{-0.001}$
Total (CMX)	0.977±0.005	0.940±0.029	0.929±0.010

(except PEM) are summarized in Table XXXIII.

F. Comparison to Top Dilepton Analysis

A consistency check between the top and SUSY identification efficiency studies is performed. Since the two analyses are very similar, the identification efficiencies are expected to be similar. However, some modifications are necessary in order to compare results between the two analyses. The conversion removal efficiencies (CEM), cosmic ray removal (muons only), and "good" CTC track selection (except for PEM) are folded in with the SUSY lepton identification efficiencies. The top dilepton TCE

TABLE XXXI. Identification efficiency for CMIO muons using the Z^0 sample.

	Efficiency (MC)	Efficiency (IA)	Efficiency (IB)
EM $\leq$ 2.0 GeV	0.990±0.003	0.975±0.025	0.960±0.009
Had $\leq$ 6.0 GeV	0.990±0.003	0.950±0.034	0.984±0.006
EM+Had $\geq$ 0.1 GeV	$1.000^{+0.000}_{-0.001}$	$1.000^{+0.000}_{-0.025}$	$1.000^{+0.000}_{-0.002}$
$d_0 \leq 0.8$ cm (raw)	$1.000^{+0.000}_{-0.001}$	$1.000^{+0.000}_{-0.025}$	0.998±0.002
$d_0 \leq 0.5$ cm (b. c.)	$1.000^{+0.000}_{-0.001}$	$1.000^{+0.000}_{-0.025}$	$1.000^{+0.000}_{-0.002}$
Total (CMIO)	0.975±0.004	0.925±0.042	0.942±0.011

TABLE XXXII. Cosmic ray removal efficiency using the Z^0 data and MC.

	Efficiency (MC)	Efficiency (IB)
TCM	$1.000^{+0.000}_{-0.001}$	$1.000^{+0.000}_{-0.001}$
LCM	$1.000^{+0.000}_{-0.001}$	$1.000^{+0.000}_{-0.001}$
CMX	$1.000^{+0.000}_{-0.001}$	$1.000^{+0.000}_{-0.001}$
CMIO	$1.000^{+0.000}_{-0.001}$	$1.000^{+0.000}_{-0.001}$

and LCE efficiencies are scaled to the cut of $E/p < 2$ since the top dilepton group uses a TCE (LCE) identification with a tighter (looser) cut of $E/p < 1.8$ (< 4.0). The efficiencies for various E/p cuts are studied by the top dilepton analysis and summarized in Table XXXIV [63]. The top muon identification efficiencies are not scaled, because the cuts are similar. The top PEM efficiency is not scaled even though the top analysis uses a tighter criteria, because there is a correlation between these cuts. Table XXXV is a list of extra cuts used by the top group for the PEM. Hence, the top PEM efficiency will be lower than that of the SUSY dilepton analysis.

Table XXXVI is a summary of this comparison. The results agree within two standard deviations (except for PEM). Note that the uncertainties of this measurement are smaller than those in the top analysis, because the entire Run IB Z^0 sample is utilized.

The summary is listed in Table XXXVII. Efficiencies of lepton identification are

TABLE XXXIII. "Good" CTC track efficiency using the Z^0 data and MC.

	Efficiency (MC)	Efficiency (IB)
TCE	0.995±0.001	0.996±0.001
LCE	0.995±0.001	0.996±0.001
TCM	$1.000^{+0.000}_{-0.001}$	$1.000^{+0.000}_{-0.001}$
LCM	$1.000^{+0.000}_{-0.001}$	$1.000^{+0.000}_{-0.001}$
CMX	0.980±0.001	$1.000^{+0.000}_{-0.001}$
CMIO	0.903±0.007	0.968±0.008

TABLE XXXIV. Efficiency of E/p in the top dilepton study with all other cuts applied.

E/p	Efficiency (IA)	Efficiency (IB)
1.8	0.982±0.003	0.974±0.004
2.0	0.990±0.003	0.970±0.004
4.0	$1.000^{+0.000}_{-0.001}$	$1.000^{+0.000}_{-0.001}$

multiplied by the photon-conversion removal (CEM), "good" CTC track, and cosmic ray removal (muons only). The Monte Carlo has in most cases overestimated the lepton identification efficiency since luminosity and aging effects were not modeled properly. The results are consistent with those from the top dilepton analysis.

TABLE XXXV. Efficiency of PEM cuts (other than those used in the SUSY analyses) in the top dilepton study with all other cuts applied.

cut	Efficiency (IA)	Efficiency (IB)
$\chi^2_{depth} < 15$	0.976±0.010	0.996±0.004
$ISO < 0.1$	$1.000^{+0.000}_{-0.003}$	0.991±0.004
$p_{\mathrm{T}}^{ExtraTrack} < 1.5$ GeV/c	0.984±0.008	0.991±0.006

TABLE XXXVI. Comparison of the SUSY dilepton identification efficiencies with those from the top dilepton analysis[63].

	Efficiency (IA)	Efficiency (IB)	Efficiency (top)
TCE	0.821±0.013	0.815±0.008	0.815±0.009
LCE	0.846±0.008	0.847±0.008	0.862±0.007
PEM	0.890±0.012	0.920±0.007	0.850±0.017
TCM	0.903±0.025	0.929±0.007	0.942±0.007
LCM	0.903±0.025	0.937±0.006	0.942±0.007
CMX	0.940±0.029	0.929±0.010	0.952±0.008
CMI	0.925±0.042	0.912±0.014	0.920±0.011

TABLE XXXVII. Summary of efficiencies including lepton identification, photon-conversion removal (TCE and LCE only), "good" CTC track (not PEM), and cosmic ray removal (muons only).

	Efficiency (MC)	Efficiency (IA)	Efficiency (IB)
TCE	0.863±0.004	0.821±0.013	0.815±0.008
LCE	0.888±0.003	0.846±0.008	0.847±0.008
PEM	0.924±0.004	0.890±0.012	0.920±0.007
TCM	0.977±0.003	0.903±0.025	0.929±0.007
LCM	0.976±0.003	0.903±0.025	0.937±0.006
CMX	0.957±0.005	0.940±0.029	0.929±0.010
CMI	0.880±0.008	0.925±0.042	0.912±0.014

APPENDIX C

LEPTON ISOLATION EFFICIENCIES

A. **Introduction**

Efficiencies of lepton calorimeter and track isolation cuts are determined using the Run IB $Z^0 \to \ell\ell$ events. These cuts are used for several SUSY multilepton analyses.

The calorimeter isolation ($ISO^{cal}_{0.4}$) is determined by summing the transverse energy deposited in the calorimeter in a cone in η-ϕ space of $\Delta R = \sqrt{(\Delta\eta)^2 + (\Delta\phi)^2} = 0.4$ around the lepton subtracting the transverse energy of the lepton:

$$ISO^{cal}_{0.4} = \sum_{\Delta R<0.4} E_{\rm T} - E_{\rm T}(\ell)$$

The track isolation ($ISO^{trk}_{0.4}$) is determined by summing the transverse momenta from all "good" CTC tracks [2] in a cone of ΔR =0.4 around the lepton (disregarding the transverse momentum of the lepton). In order to minimize the effect of multiple interactions due to high instantaneous luminosity on SUSY processes, only the momenta of those tracks that are within 10 cm of the lepton's z-vertex are summed. A track isolation cut is employed for both leptons to reduce the isolation not measured by the calorimeter.

The track isolation cut is defined as:

$$ISO^{trk}_{0.4} = \sum_{\Delta R<0.4} p_{\rm T} - p_{\rm T}(\ell)$$

[2] A "good" CTC track is a 3D track found with ≥ 3 axial superlayer hits, ≥ 2 stereo superlayer hits, and ≥ 6 total superlayer hits in the CTC.

A comparison between $Z^0 \to \ell\ell$ data and Monte Carlo events is made in order to determine scale factors necessary to apply to Monte Carlo events so that effects can be incorporated that are not simulated (*e.g.*, effects due to luminosity, aging, and multiple interactions).

B. **Data Samples**

The inclusive electron and muon data samples are used to study the lepton isolation efficiencies. The selection cuts for the inclusive electron and muon samples are summarized in Tables XXXVIII and XXXIX, respectively.

TABLE XXXVIII. Cuts applied to the inclusive electron sample.

Object type	Variable	Cut
	$E_{\rm T}$	$\geq$ 20 GeV
	E/p (corrected)	$\leq$ 1.8
	HAD/EM (3×3)	$\leq$ 0.05
	$LSHR$	$\leq$ 0.2
	$\mid \Delta x \mid$	$\leq$ 1.5 cm
CEM	$\mid \Delta z \mid$	$\leq$ 3.0 cm
	χ^2_{strip}	$\leq$ 10.0
	$\mid z_{vertex} \mid$	$\leq$ 60 cm
	$\mid z_{vertex} - z^e_0 \mid$	$\leq$ 5 cm (Vertex Class $\geq$ 10)
	Fiducial (FIDELE)	Yes
	Conversion Removal (CONVERT2)	Yes

Opposite charge dielectron[3] and dimuon events are selected from the inclusive electron and muon samples respectively in the dilepton mass range: $50 \leq M(\ell,\ell) \leq 150$ GeV/c^2. The track vertex of the second leg is required to be within 10 cm of that of the first leg (except for the PEM for which uses the VTVZ vertex). The legs of the dilepton event are required to be well separated ($\Delta R(\ell_1,\ell_2) > 0.4$) in η-ϕ space. The tight electron leg is required to be a CEM cluster with $E_{\rm T} > 20$

[3]except for CEM-PEM events

TABLE XXXIX. Cuts applied to the inclusive muon sample.

Object type	Variable	Cut
	p_{T} (beam constrained)	$\geq$ 20 GeV/c
	EM	$\leq$ 2 GeV
	HAD	$\leq$ 6 GeV
	EM+HAD	$\geq$ 0.1 GeV
CMUP	d_0 (beam constrained)	$\leq$ 0.3 cm
	$\mid \Delta x \mid$ (CMU)	$\leq$ 2.0 cm
	$\mid \Delta x \mid$ (CMP)	$\leq$ 5.0 cm
	$\mid z_{vertex} \mid$	$\leq$ 60 cm
	$\mid z_{vertex} - z_0^{\mu} \mid$	$\leq$ 5 cm (Vertex Class $\geq$ 10)

GeV as a requirement to pass the CEM_16_CFT_12 trigger. The tight muon leg is necessary to have a stub in the CMU and to have $p_{\mathrm{T}}^{\mu} > 20$ GeV/c. Hence the muon sample is inclusive of all high-p_{T} CMUP* and CMNP* triggers [4]. The identification requirements as listed in Table XL are imposed on both legs.

Cuts as listed in Table XLI are applied for jet identification. The JTC96X (correcting for both the underlying event and out of cone corrections) are applied to determine the energies of the jets that are found to be in the central or plug regions of the calorimeter.

C. **Method**

The efficiency of events passing the isolation cut in a dilepton mass window of 76 $\leq M(\ell,\ell) \leq$ 106 GeV/c^2 are estimated using the following formula:

$$\epsilon_{iso} = \frac{N_{iso<x}}{N_{tot}} \pm \sqrt{\frac{N_{iso<x}(N_{tot} - N_{iso<x})}{N_{tot}^3}}, \tag{C.1}$$

where N_{tot} is the total number of events in the sample, x is the isolation cut of choice,

[4] These triggers are CMUP_CFT_12_5DEG* and CMNP_CFT_12_5DEG*

TABLE XL. The cuts used to select the sample.

	Cut	Tight Cut	Loose Cut
CEM	E/p	$\leq$ 2.0	$\leq$ 2.0
	$\frac{Had}{Em}$	$\leq$ 0.05	$\leq$ 0.055+0.045$\frac{E}{100}$
	L_{shr}	$\leq$ 0.2	$\leq$ 0.2
	$\mid \delta x \mid$	$\leq$ 3.0 cm	$\leq$ 3.0 cm
	$\mid \delta z \mid$	$\leq$ 5.0 cm	$\leq$ 5.0 cm
	χ^2_{strip}	$\leq$ 10.0	$\leq$ 15.0
	FIDELE	yes	yes
	CONVERT2	yes	yes
PEM	$\frac{Had}{Em}$		$\leq$ 0.1
	χ^2_{3x3}		$\leq$ 3.0
	VTX Occ.		$\geq$ 0.50
	FIDELE		yes
CMU/CMP	Em	$\leq$ 2.0 GeV	$\leq$ 2.0 GeV
	Had	$\leq$ 6.0 GeV	$\leq$ 6.0 GeV
	Em+Had		$\geq$ 0.1 GeV
	CMU δx	$\leq$ 2.0 cm	$\leq$ 2.0 cm
	CMP δx	$\leq$ 5.0 cm	$\leq$ 5.0 cm
	or χ^2_x	$\leq$ 9.0	$\leq$ 9.0
	d_0 (raw)	$\leq$ 0.5 cm	$\leq$ 0.8 cm
	d_0 (b. c.)	$\leq$ 0.2 cm	$\leq$ 0.5 cm
CMX	Em		$\leq$ 2.0 GeV
	Had		$\leq$ 6.0 GeV
	Em+Had		$\geq$ 0.1 GeV
	CMX δx		$\leq$ 5.0 cm
	or χ^2_x		$\leq$ 9.0
	d_0 (raw)		$\leq$ 0.8 cm
	d_0 (b. c.)		$\leq$ 0.5 cm
CMIO	Em		$\leq$ 2.0 GeV
	Had		$\leq$ 6.0 GeV
	Em+Had		$\geq$ 0.1 GeV
	d_0 (raw)		$\leq$ 0.8 cm
	d_0 (b. c.)		$\leq$ 0.5 cm
	CMUSWM		yes

TABLE XLI. Jet identification criteria.

Object type	Variable	Cut
JETS	$E_{\rm T}$ (raw)	$\geq$ 10 GeV
	E_T (corrected)	$\geq$ 15 GeV
	$\mid \eta \mid$	$\leq$ 2.4
	$\Delta R(\ell, j)$	$\geq$ 0.4
	$\Delta R(j, j)$	$\geq$ 0.4

and $N_{iso<x}$ is the subset in which the second-leg leptons passes that isolation cut. Note, however, if the number of the events that have passed the isolation cut are equal to the number of total entries in that bin, then the error is taken to be $\sqrt{\frac{N_{tot}-1}{N_{tot}}}$. No isolation cut is applied on the first leg.

For TCE-TCE and TCM-TCM, the efficiency is determined using the following formula:

$$\epsilon_{iso} = \frac{2N^{iso_1<x}_{iso_2<x} + N^{iso_1>x}_{iso_2<x} + N^{iso_1<x}_{iso_2>x}}{2N^{iso_1<x}_{iso_2<x} + 2N^{iso_1>x}_{iso_2<x} + 2N^{iso_1<x}_{iso_2>x} + 2N^{iso_1>x}_{iso_2>x}} \pm \sqrt{\frac{(2N^{iso_1<x}_{iso_2<x} + N^{iso_1>x}_{iso_2<x} + N^{iso_1<x}_{iso_2>x})(2N^{iso_1>x}_{iso_2>x} + N^{iso_1>x}_{iso_2<x} + N^{iso_1<x}_{iso_2>x})}{(2N^{iso_1<x}_{iso_2<x} + 2N^{iso_1>x}_{iso_2<x} + 2N^{iso_1<x}_{iso_2>x} + 2N^{iso_1>x}_{iso_2>x})^3}} \quad \text{(C.2)}$$

Note that the errors on the isolation efficiency using "tight-tight" events are smaller than the errors using "tight-loose" events due to the fact that both legs are used to determine the efficiency.

D. **Calorimeter Isolation Efficiency**

Calorimeter efficiencies have been examined as a function of the choice of isolation cut using $Z^0 \to \ell\ell$ events seen at CDF in Run I. Efficiencies are listed for central electrons, plug electrons, and muons at choices of isolation cuts at 2 GeV, 3 GeV, and 4 GeV in a cone of 0.4 in $\eta - \phi$ space in Table XLII. Note that the efficiency

TABLE XLII. Efficiency of the calorimeter isolation cut from $Z^0 \to \ell^+\ell^-$ data. Errors are statistical only.

Object	$ISO^{cal}_{0.4} \leq 2$ GeV	$ISO^{cal}_{0.4} \leq 3$ GeV	$ISO^{cal}_{0.4} \leq 4$ GeV
e^{CEM}	0.8462 ± 0.0084	0.9349 ± 0.0054	0.9666 ± 0.0037
e^{PEM}	0.8000 ± 0.0086	0.9421 ± 0.0050	0.9755 ± 0.0033
μ	0.8384 ± 0.0095	0.9236 ± 0.0069	0.9698 ± 0.0044

TABLE XLIII. Efficiency of the calorimeter isolation cut of 4 GeV from $Z^0 \to \ell^+\ell^-$ data for jet multiplicity of cone size 0.4. Errors are statistical only.

Object	$n_j = 0$	$n_j = 1$	$n_j \geq 2$
e^{CEM}	0.970 ± 0.004	0.956 ± 0.012	0.936 ± 0.028
e^{PEM}	0.977 ± 0.004	0.967 ± 0.010	0.971 ± 0.020
μ	0.971 ± 0.005	0.966 ± 0.011	0.904 ± 0.041

cut at 2 GeV agrees with the Run I low-mass Drell-Yan ($\gamma \to \ell\ell$) analysis [46]. The cut used in this analysis is 4 GeV. The effect of jet multiplicity in the events is also examined in Table XLIII.

E. **Track Isolation Efficiency**

Track isolation efficiencies have been examined as a function of the choice of isolation cut using $Z^0 \to \ell\ell$ events seen at CDF in Run I. Calorimeter isolation cuts of 4 GeV have been placed on each leg. Efficiencies are listed for central electrons and muons at choices of track isolation cuts at 2 GeV/c, 3 GeV/c, and 4 GeV/c in a cone of 0.4 in $\eta - \phi$ space in Table XLIV. The cut used in this analysis is 4 GeV/c. The effect of jet multiplicity in the events is also examined in Table XLV.

TABLE XLIV. Efficiency of the track isolation cut from $Z^0 \to \ell^+\ell^-$ data. Errors are statistical only.

Object	$ISO^{cal}_{0.4} \leq 2$ GeV	$ISO^{cal}_{0.4} \leq 3$ GeV	$ISO^{cal}_{0.4} \leq 4$ GeV
e^{CEM}	0.9535 ± 0.0050	0.9776 ± 0.0035	0.9868 ± 0.0027
μ	0.9393 ± 0.0045	0.9835 ± 0.0024	0.9918 ± 0.0017

TABLE XLV. Efficiency of the track isolation cut of 4 GeV/c from $Z^0 \to \ell^+\ell^-$ data for jet multiplicity of cone size 0.4. Errors are statistical only.

Object	$n_j = 0$	$n_j = 1$	$n_j \geq 2$
e^{CEM}	0.989 ± 0.003	0.982 ± 0.008	0.971 ± 0.020
μ	0.998 ± 0.001	0.992 ± 0.004	$1.000^{+0.000}_{-0.017}$

F. Monte Carlo

A 422.7 pb^{-1} Monte Carlo (MC) sample of Drell-Yan ($Z^0 \to \ell\ell$) events is used. The events are generated using ISAJET 7.16 with CTEQ2L used as the structure function and simulated through the CDF detector simulation (QFL′).

1. Calorimeter Isolation Efficiency

Calorimeter efficiencies have been examined as a function of the choice of isolation cut using $Z^0 \to \ell\ell$ events found in MC. Efficiencies are listed for central electrons, plug electrons, and muons at choices of isolation cuts at 2 GeV, 3 GeV, and 4 GeV in a cone of 0.4 in $\eta - \phi$ space in Table XLVI. The cut used in this analysis is 4 GeV. The effect of jet multiplicity in the events is also examined in Table XLVII.

TABLE XLVI. Efficiency of the calorimeter isolation cut from $Z^0 \to \ell^+\ell^-$ MC. Errors are statistical only.

Object	$ISO^{cal}_{0.4} \leq 2$ GeV	$ISO^{cal}_{0.4} \leq 3$ GeV	$ISO^{cal}_{0.4} \leq 4$ GeV
e^{CEM}	0.9500 ± 0.0029	0.9722 ± 0.0022	0.9815 ± 0.0018
e^{PEM}	0.9805 ± 0.0016	0.9910 ± 0.0011	0.9941 ± 0.0009
μ	0.9379 ± 0.0033	0.9712 ± 0.0023	0.9835 ± 0.0017

TABLE XLVII. Efficiency of the calorimeter isolation cut of 4 GeV from $Z^0 \to \ell^+\ell^-$ MC for jet multiplicity of cone size 0.4. Errors are statistical only.

Object	$n_j = 0$	$n_j = 1$	$n_j \geq 2$
e^{CEM}	0.991 ± 0.002	0.990 ± 0.004	0.994 ± 0.006
e^{PEM}	0.995 ± 0.001	0.995 ± 0.003	0.991 ± 0.009
μ	0.989 ± 0.002	0.985 ± 0.004	0.980 ± 0.011

2. **Track Isolation Efficiency**

Track isolation efficiencies have been examined as a function of the choice of isolation cut using $Z^0 \to \ell\ell$ events seen in MC. Calorimeter isolation cuts of 4 GeV have been placed on each leg. Efficiencies are listed for central electrons and muons at choices of track isolation cuts at 2 GeV/c, 3 GeV/c, and 4 GeV/c in a cone of 0.4 in $\eta - \phi$ space in Table XLVIII. The cut used in this analysis is 4 GeV/c. The effect of jet multiplicity in the events is also examined in Table XLIX.

TABLE XLVIII. Efficiency of the track isolation cut from $Z^0 \to \ell^+\ell^-$ MC. Errors are statistical only.

Object	$ISO^{cal}_{0.4} \leq 2$ GeV	$ISO^{cal}_{0.4} \leq 3$ GeV	$ISO^{cal}_{0.4} \leq 4$ GeV
e^{CEM}	0.9567 ± 0.0028	0.9816 ± 0.0018	0.9905 ± 0.0013
μ	0.9454 ± 0.0022	0.9847 ± 0.0012	0.9939 ± 0.0008

TABLE XLIX. Efficiency of the track isolation cut of 4 GeV/c from $Z^0 \to \ell^+\ell^-$ MC for jet multiplicity of cone size 0.4. Errors are statistical only.

Object	$n_j = 0$	$n_j = 1$	$n_j \geq 2$
e^{CEM}	0.991 ± 0.001	0.990 ± 0.003	0.984 ± 0.009
μ	0.997 ± 0.001	0.992 ± 0.002	0.995 ± 0.004

APPENDIX D

JETS

A. **Definition of Jet**

Many methods can be used to define what is meant by a jet of hadrons. Here, a *cone algorithm* based on the energy deposition in an angular region (*e. g.*, the Sterman-Weinberg definition [72]). In CDF, a jet is a concentration of transverse energy, $E_{\rm T}$, in a 'cone' of radius ΔR, where :

$$\Delta R = \sqrt{(\Delta\eta)^2 + (\Delta\phi)^2} \tag{D.1}$$

and $E_{\rm T}$ is defined as :

$$E_{\rm T} = E \sin\theta \tag{D.2}$$

CDF has performed analyses using jet cone sizes of $\Delta R = 0.4$ and $\Delta R = 0.7$. This analysis employs cone size of $\Delta R = 0.4$ for jets.

By defining ΔR in terms of $\Delta\eta$ (rather than, say $\Delta\theta$) the jet energy remains invariant under longitudinal boosts. In the two-dimensional η-ϕ plane, curves of constant ΔR are circles around the axis of the jet. It is for this reason that the CDF calorimetry is segmented in $\Delta\eta \times \Delta\phi$ (see Fig. 48).

B. **Jet Energy**

The jet energy and momentum components are defined from the list of cluster towers as:

$$E_J = \sum_i^N E_i \tag{D.3}$$

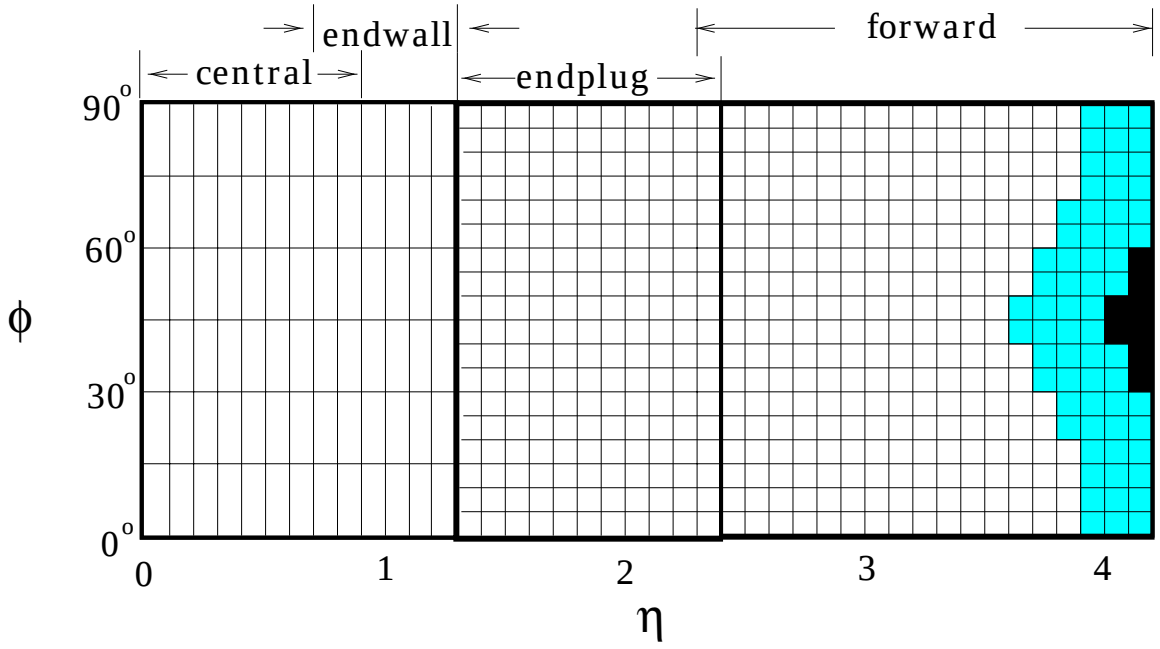

FIG. 48. The $\Delta\eta \times \Delta\phi$ segmentation of the CDF calorimetry.

$$P_{x,J} = \sum_{i}^{N} E_i \sin\theta_i \cos\phi_i \quad \text{(D.4)}$$

$$P_{y,J} = \sum_{i}^{N} E_i \sin\theta_i \sin\phi_i \quad \text{(D.5)}$$

$$P_{z,J} = \sum_{i}^{N} E_i \cos\theta_i \quad \text{(D.6)}$$

$$\text{(D.7)}$$

where i is the tower index and N the number of towers in the cluster.

Using the above defined quantities, the jet energy and momentum transverse components $P_{\mathrm{T,J}}$ and $E_{\mathrm{T,J}}$ are derived as:

$$P_{\mathrm{T,J}} = \sqrt{P_{x,J}^2 + P_{y,J}^2} \quad \text{(D.8)}$$

$$P_J = \sqrt{P_{x,J}^2 + P_{y,J}^2 + P_{z,J}^2} \quad \text{(D.9)}$$

$$E_{\mathrm{T,J}} = E_J \frac{P_{\mathrm{T,J}}}{P_J} \quad \text{(D.10)}$$

$$\text{(D.11)}$$

C. Jet Energy Corrections

Jet energy corrections are implemented via an offline routine called JTC96X [74]. It has been known since the days of CDF Run 0 (1988-89) that in order to reconstruct the true momentum of parton from the measured jet E_{T} inside a clustering cone, proper corrections need to be applied to account for detector and physics effects [73]. The main stages of jet energy correction are the (1) *relative* ('E', or 'N'), (2) *absolute* ('Y' or 'N'), (3)*underlying event* ('Y' or 'N'), and (4)*out-of-cone* ('Y' or 'N') corrections.

1. **Relative correction** accounts for the non-uniform response of different calorimeters and measures the calorimeter response in the plug and forward regions relative to the central region.

2. **Absolute correction** estimates the true parton E_{T} inside the cone based on the observed raw E_{T}, accounting for the non-linear response of the calorimeter.

3. **Underlying event** subtraction is done by estimating the energy in the clustering cone that was not involved in hard scattering.

4. **Out-of-cone** inclusion of energy of the jet lying outside the cone.

APPENDIX E

ISAJET VALIDATION

A. **Introduction**

In SUSY multilepton analyses, ISAJET Monte Carlo is used to generate the Standard Model (SM) backgrounds : (1) Z^0 production, (2) low-mass Drell-Yan (DY) process, (3) $t\bar{t}$ production, (4) diboson production, and (5) $b\bar{b}/c\bar{c}$ production.

The level of agreement between data and Monte Carlo is studied in terms of cross-sections and/or kinematical distributions. Results of the following ISAJET validations are reported: (a) normalization of ISAJET cross-sections to the CDF measurements for Z^0, low-mass Drell-Yan, and $t\bar{t}$ production; (b) normalization of ISAJET cross-sections for diboson production to next-to-leading order (NLO) prediction; (c) a comparison between $b\bar{b}/c\bar{c}$ Monte Carlo events to data in the $e\mu$ channel. Corrections to lepton identification, isolation, and trigger efficiency in Monte Carlo to those in data are applied. Monte Carlo samples are scaled to luminosity. The scaling factors are determined for Monte Carlo samples generated with parton density functions (PDFs), CTEQ2L, MRSD0$'$, and GRVLO. The parton density function, MRSD0$'$, is used by this analysis to determine the Standard Model backgrounds; the other parton density functions are presented for comparison. Although this search employs the jet cone size of 0.4, kinematic distributions using both jet cone sizes used at CDF, namely 0.4 and 0.7, are presented. The kinematics using jet cone size 0.7 are studied for comparison.

TABLE L. Additional cuts to those in Tables VII and VIII are used to select dileptons.

	Cut	Tight Cut	Loose Cut
	E_{T}	$\geq$ 11.0 GeV	$\geq$ 5.0 GeV
	p_{T}	$\geq$ 4.0 GeV/c	$\geq$ 2.8 GeV/c
CEM	FIDELE	yes	yes
	CONVERT2	yes	yes
	p_{T}	$\geq$ 11.0 GeV/c	$\geq$ 5.0 GeV/c
	Muon Type	CMUP	CMU/CMP/CMUP
CMU/CMP	$\lvert d_0 \rvert$ (b.c.)	$\leq$ 0.2 cm	$\leq$ 0.5 cm
	CMCOS	yes	yes
	CMUSWM	yes	yes
	p_{T}		$\geq$ 5.0 GeV/c
CMX	$\lvert d_0 \rvert$ (b.c.)		$\leq$ 0.5 cm
	CMCOS		yes
	CMUSWM		yes
	p_{T}		$\geq$ 10.0 GeV/c
CMIO	$\lvert d_0 \rvert$ (b.c.)		$\leq$ 0.5 cm
	CMIOFID		yes

B. **Identification Criteria for Leptons and Jets**

The identification criteria for electrons and muons are stated in Tables VII and VIII, respectively. Additional cuts are listed in Table L. Jet identification criteria can be found in Table LI. It should be noted that only central leptons are of interest.

In a selection of dilepton events, the tight lepton ($p_{\mathrm{T}} \geq 11$ GeV/c) must be classified as a tight central electron (TCE) or a tight central CMUP muon (TCM). Additional leptons with momentum above 5 GeV/c must be loose central electrons (LCE) or loose central CMU/CMP/CMX/CMIO muons (LCM, CMX, CMIO). Two leptons must be well separated ($\Delta R_{\ell_1 \ell_2} > 0.4$) but originate from the same vertex ($|z_0^{trk1} - z_0^{trk2}| \leq 10$ cm).

For studies of Drell-Yan (γ, Z^0) events, calorimeter and tracking based isolation cuts ($ISO_{0.4}^{cal} \leq 4.0$ GeV and $ISO_{0.4}^{trk} \leq 4.0$ GeV/c) are applied.

TABLE LI. Cuts used to select jets.

	Quantity	Cut
JETS	$E_{\rm T}$ (raw)	$\geq$ 10 GeV
	$E_{\rm T}$ (JTC96X 'EYDD')	$\geq$ 15 GeV
	$\mid \eta_{det} \mid$	$\leq$ 2.4
	$\Delta R(\ell, j^{0.7(0.4)})_{det}$	$\geq$ 0.7(0.4)

TABLE LII. $e\mu$ triggers for studies of $b\bar{b}/c\bar{c}$ events.

Level	Run IB [75]
1	CEM_CMU_OR_CMX*
2	CEM_5_CFT_4_7_CMU_2_7*
	CEM_5_CFT_4_7_CMX_2_7*
3	PSIB_E_CMUP*
	PSIB_E_CMX*

C. Triggers in Dilepton Datasets

In the ee and the $\mu\mu$ datasets for studies of Drell-Yan (γ,Z^0), events are required to follow inclusive lepton trigger paths (see Tables IV and V). In the $e\mu$ dataset for studies of $b\bar{b}/c\bar{c}$ events, the trigger path outlined in Table LII is required. The $e\mu$ trigger efficiencies are studied in Ref. [75].

D. $Z^0 \to \ell\ell$

The Z^0 boson events are generated by ISAJET with $5 \leq q_{\rm T} \leq 500$ GeV[62]. Distributions of (a) jet multiplicity and (b) kinematics of two leading jets for two jet cone sizes of 0.4 and 0.7 are checked by comparing to the data. The ISAJET cross-section times branching ratio ($\sigma \cdot Br(Z^0 \to \ell\ell)$) is corrected by scaling to the the CDF Run I published measurement of $\sigma \cdot Br(Z^0 \to \mu^+\mu^-) = 233 \pm 18$ pb [59]. The ISAJET cross-sections and scaling factors for three parton distribution functions (MRSD0′,

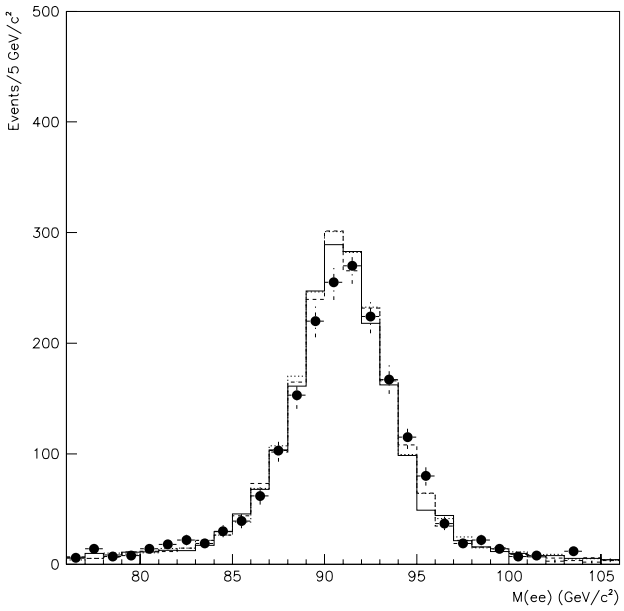

FIG. 49. The dielectron mass using MRSD0′(solid), CTEQ2L (dashed), and GRVLO (dotted) structure functions are compared to data (points).

CTEQ2L, and GRVLO) are summarized in Table LIII. The standard CDF data samples for $Z^0 \to \ell^{\pm}\ell^{\mp}$ to compare with ISAJET events with scaling factors. The $Z^0 \to \ell^+\ell^-$ data samples are selected from the Duke University $Z^0 \to e^+e^-$ and the Johns Hopkins-Harvard $Z^0 \to \mu^+\mu^-$ datasets [57, 76]. Using the scaling factors, dilepton mass distributions for $Z^0 \to e^+e^-$ and $\mu^+\mu^-$ events in Monte Carlo and data samples are compared. Figures 49 and 50 show the distributions of dilepton mass for mass window $76 \leq M(\ell\ell) \leq 106$ GeV/c^2.

The Monte Carlo agrees with the data very well. Using the scaling factors, the kinematical distributions from Monte Carlo are compared with those found from data. Tables LIV and LV display the jet multiplicity for $Z^0 \to \ell^+\ell^-$ events ($76 \leq M(\ell\ell) \leq 106$ GeV/c^2) for jet cone sizes of 0.4 and 0.7, respectively. The results are also shown in Figs. 51 and 52. A good agreement between Monte Carlo and data is seen in the analysis with cone size 0.4. The agreement is worse in the analysis with cone size 0.7. In a 2-jet bin, for example, Monte Carlo predictions with MRSD0′, CTEQ2L, and GRVLO are systematically lower than the data. Distributions of E_T and η for two

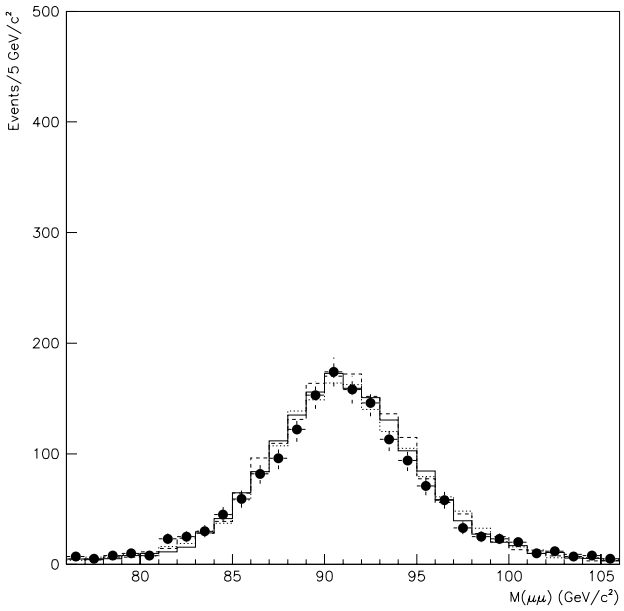

FIG. 50. The dimuon mass using MRSD0′(solid), CTEQ2L (dashed), and GRVLO (dotted) structure functions are compared to data (points).

leading jets are examined with cone sizes 0.4 and 0.7. Figures 53 and 54 demonstrate agreement of the kinematics between data and Monte Carlo using jet cone size 0.4 for $Z^0 \to ee$ and $\mu\mu$, respectively. Figures 55 and 56 display kinematics of jets with cone size 0.7 in $Z^0 \to ee$ and $\mu\mu$ events, respectively. Monte Carlo is consistent with data in the analysis with jet cone size 0.4. However, in the analysis with jet cone size 0.7, the data points are systematically higher than Monte Carlo predictions. A large discrepancy is especially found in the lowest E_T bin.

The excess of the number of events seen in data with cone size 0.7 is possibly explained by a poor modeling of the underlying event or the lack of multiple interactions in the Monte Carlo samples, because the jet clustering algorithm is likely to pick many more low E_T clusters with a larger cone size. It should be noted that ISAJET does not properly model the the p_{T}^Z. Pythia also has been known to present some problems [77]. VECBOS is also known to show disagreements at low p_{T}^Z [78]. In fact, the only Monte Carlo that best models the p_{T}^Z is RESBOS [79].

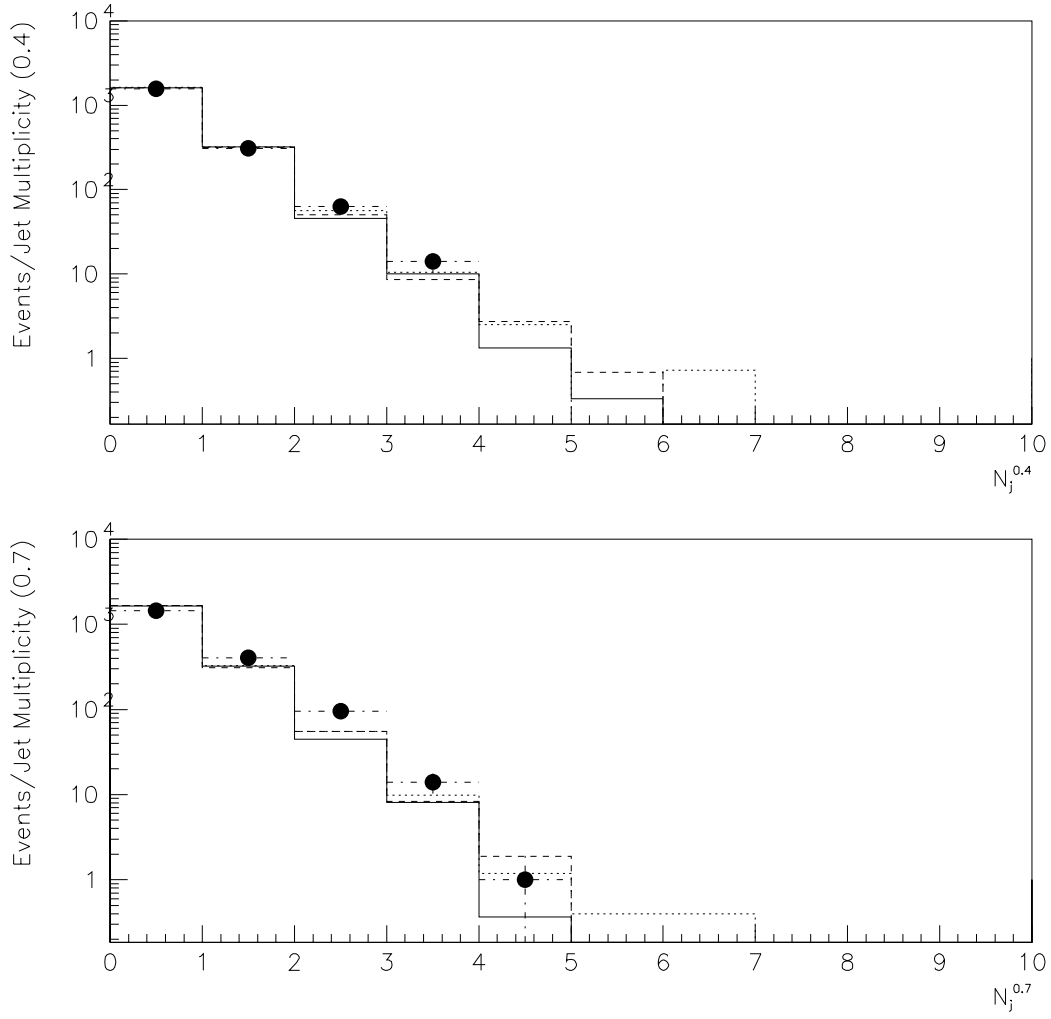

FIG. 51. The jet multiplicity spectra using $Z^0 \rightarrow ee$ applying MRSD0′(solid), CTEQ2L (dashed), and GRVLO (dotted) structure functions are compared to data (points).

TABLE LIII. ISAJET Monte Carlo cross-sections & scaling factors for $Z^0 \rightarrow \ell\ell$. The Monte Carlo events are generated with $5 \leq q_{\rm T} \leq 500$ GeV.

PDF	σ (pb)	Correction
MRSD0′	130	1.79 ± 0.14
GRVLO	109	2.14 ± 0.16
CTEQ2L	120	1.94 ± 0.15

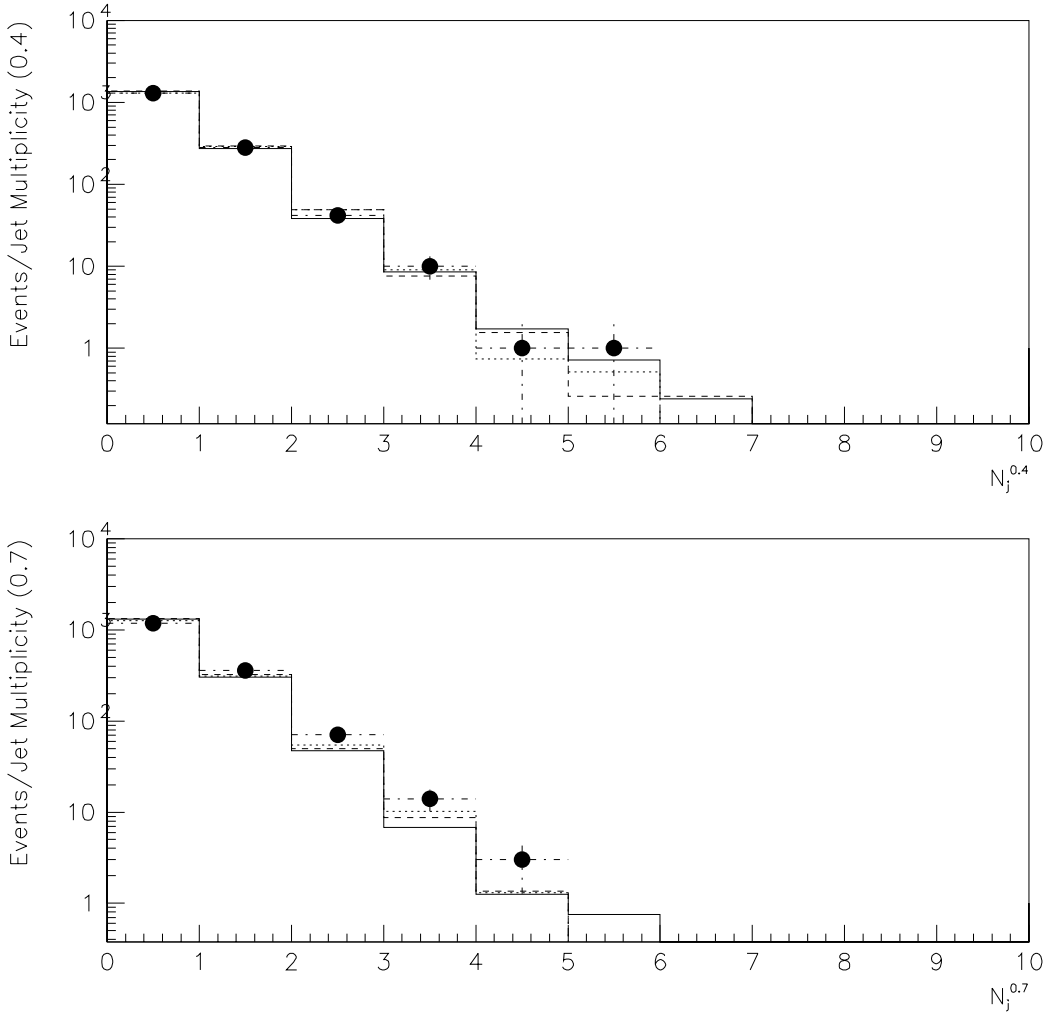

FIG. 52. The jet multiplicity spectra using $Z^0 \rightarrow \mu\mu$ applying MRSD0′(solid), CTEQ2L (dashed), and GRVLO (dotted) structure functions are compared to data (points).

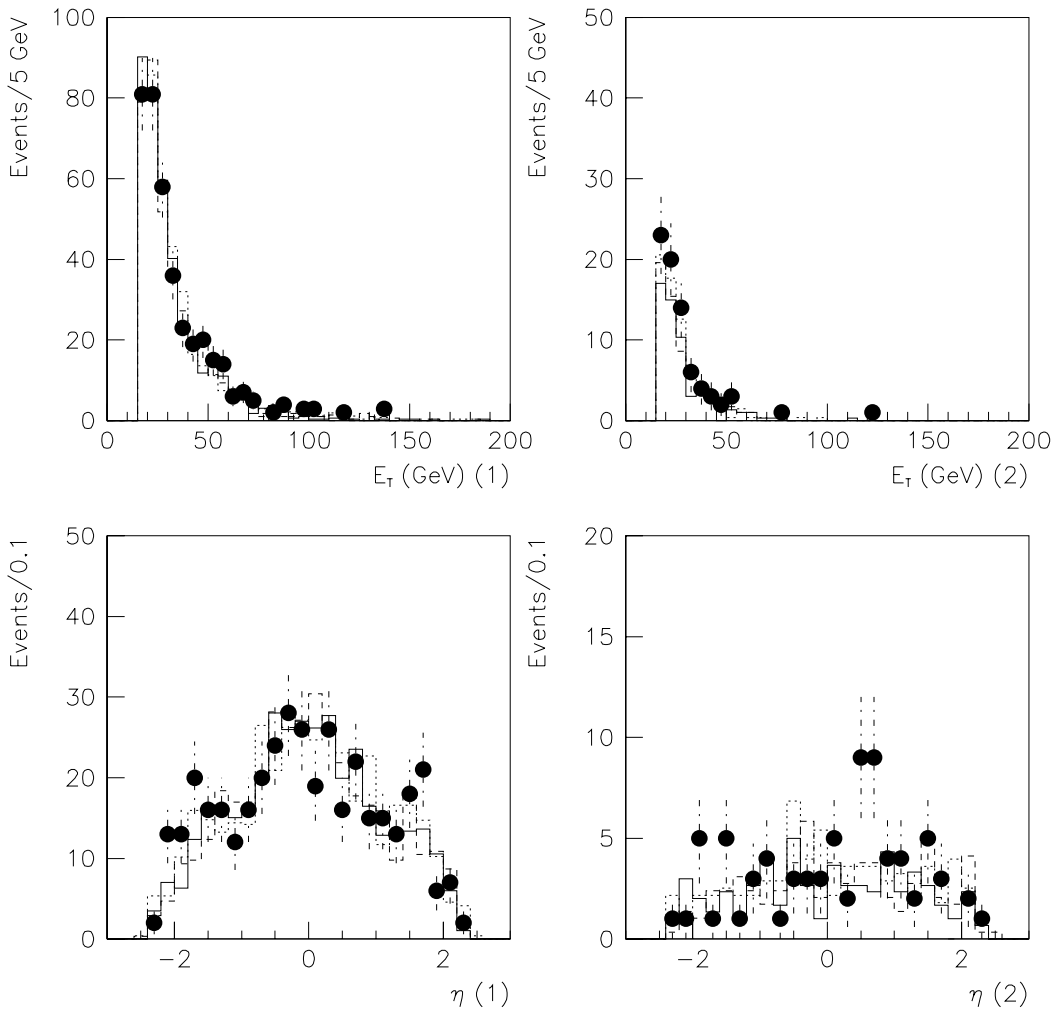

FIG. 53. The corrected jet energies and rapidities of the two leading jets with cone size 0.4 in $Z^0 \to ee$ events using MRSD0′(solid), CTEQ2L (dashed), and GRVLO (dotted) structure functions are compared to data (points). The leading jet $E_{\rm T}$ is plotted for the $Z^0 + \geq 1$ jet selection; the second leading jet $E_{\rm T}$ is plotted for the $Z^0 + \geq 2$ jet selection.

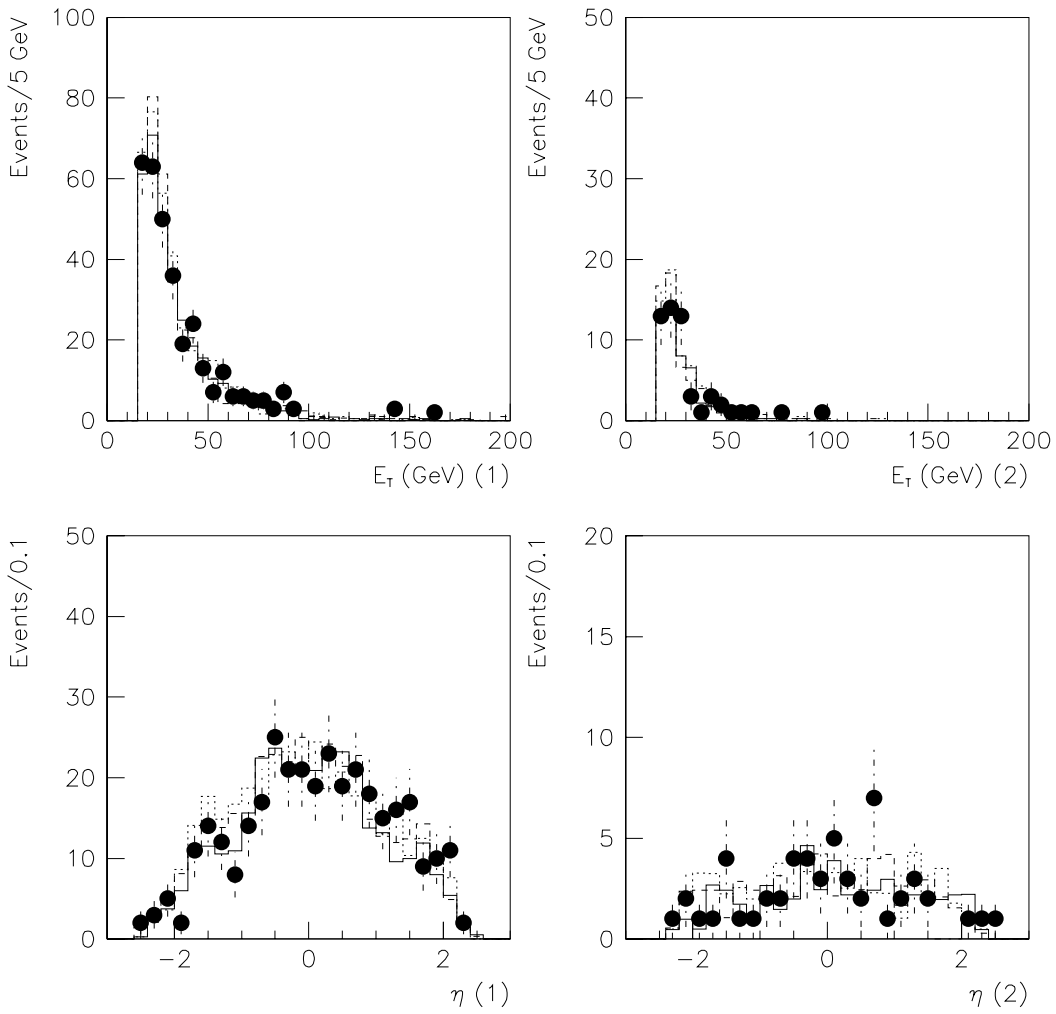

FIG. 54. The corrected jet energies and rapidities of the two leading jets with cone size 0.4 in $Z^0 \to \mu\mu$ events using MRSD0′(solid), CTEQ2L (dashed), and GRVLO (dotted) structure functions are compared to data (points). The leading jet $E_{\rm T}$ is plotted for the $Z^0 + \geq 1$ jet selection; the second leading jet $E_{\rm T}$ is plotted for the $Z^0 + \geq 2$ jet selection.

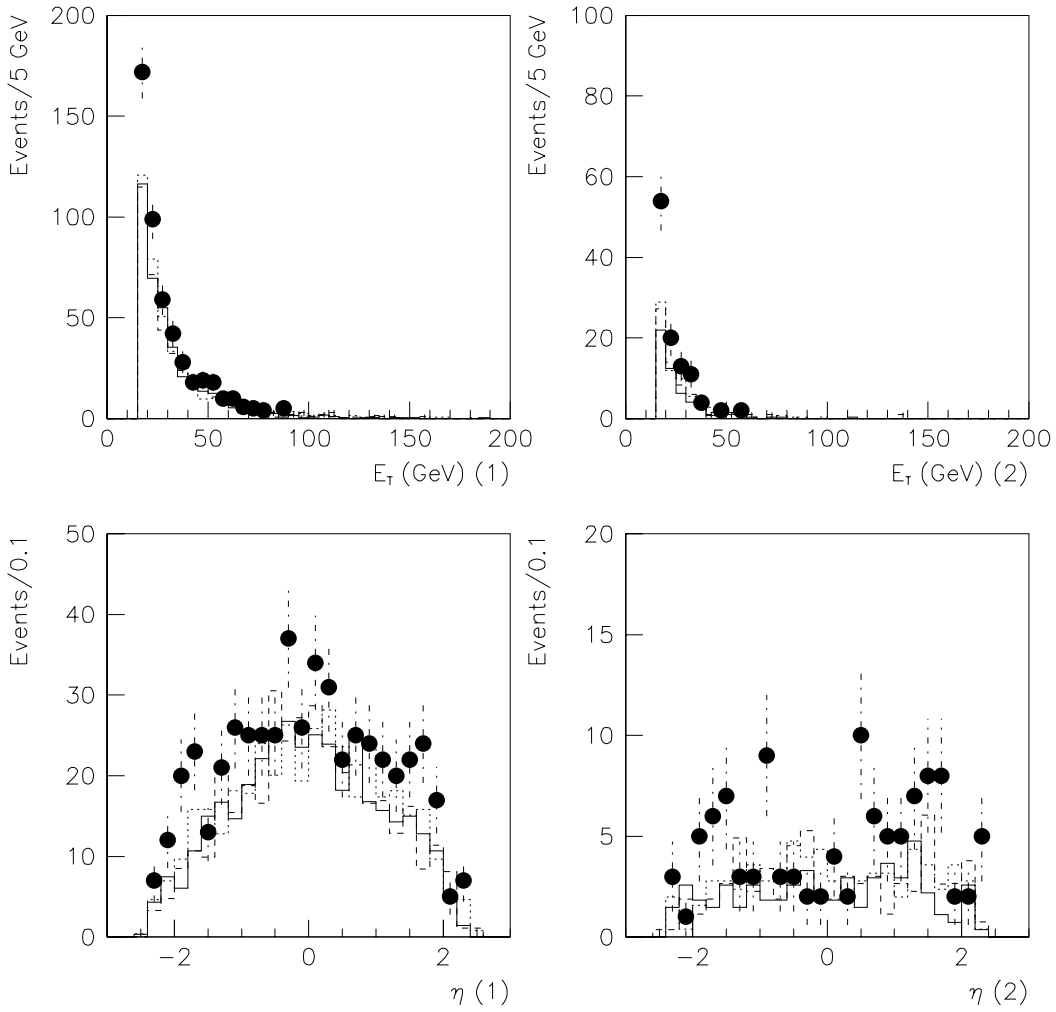

FIG. 55. The corrected jet energies and rapidities of the two leading jets with cone size 0.7 in $Z^0 \to ee$ events using MRSD0′(solid), CTEQ2L (dashed), and GRVLO (dotted) structure functions are compared to data (points). The leading jet $E_{\rm T}$ is plotted for the $Z^0 + \geq 1$ jet selection; the second leading jet $E_{\rm T}$ is plotted for the $Z^0 + \geq 2$ jet selection.

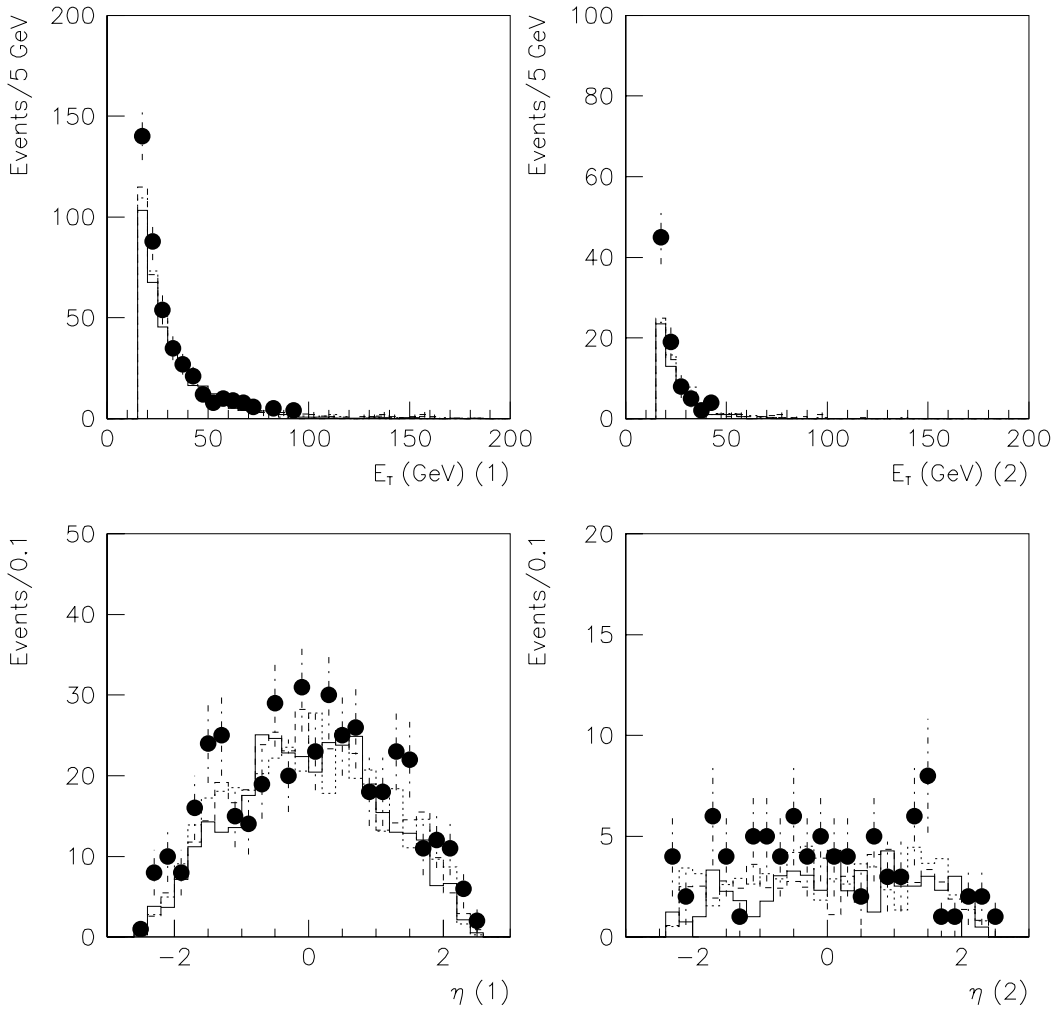

FIG. 56. The corrected jet energies and rapidities of the two leading jets with cone size 0.7 in $Z^0 \to \mu\mu$ events using MRSD0′(solid), CTEQ2L (dashed), and GRVLO (dotted) structure functions are compared to data (points). The leading jet $E_{\rm T}$ is plotted for the $Z^0 + \geq 1$ jet selection; the second leading jet $E_{\rm T}$ is plotted for the $Z^0 + \geq 2$ jet selection.

TABLE LIV. Jet multiplicity in Z^0 data and Monte Carlo using a cone size of 0.4. The Monte Carlo predictions are normalized to the Run IB luminosity.

$N_{j^{0.4}}$	$Z^0 \to ee$	MRSD0′	CTEQ2L	GRVLO
0	1568	1600	1617	1642
1	309	320	318	318
2	63	46	50	56
3	14	10	9	10
≥ 4	0	1	3	3

$N_{j^{0.4}}$	$Z^0 \to \mu\mu$	MRSD0′	CTEQ2L	GRVLO
0	1295	1354	1377	1306
1	281	274	293	291
2	42	38	49	50
3	10	9	8	9
≥ 4	1	2	2	1

TABLE LV. Jet multiplicity in Z^0 data and Monte Carlo using a cone size of 0.7. The Monte Carlo predictions are normalized to the Run IB luminosity.

$N_{j^{0.7}}$	$Z^0 \to ee$	MRSD0′	CTEQ2L	GRVLO
0	1441	1638	1658	1672
1	402	323	312	330
2	96	45	55	56
3	14	8	8	10
≥ 4	1	0	2	1

$N_{j^{0.7}}$	$Z^0 \to \mu\mu$	MRSD0′	CTEQ2L	GRVLO
0	1183	1309	1335	1269
1	359	303	326	313
2	71	47	50	55
3	14	7	9	10
≥ 4	3	1	1	1

TABLE LVI. CDF measured cross-section for low-mass Drell-Yan process including statistical and systematic uncertainties[80].

Mass bin	ee & $\mu\mu$ [pb/(GeV/c^2)]	$\times\Delta M \times \Delta y$ [pb]
11-15	16.4 ± 6.3	131.2 ± 50.4
15-20	6.3 ± 2.3	63.0 ± 23.0
20-30	2.0 ± 0.6	40.0 ± 12.0
30-40	0.78 ± 0.28	15.6 ± 5.6
40-50	0.29 ± 0.16	5.8 ± 3.2
50-60	0.16 ± 0.11	3.2 ± 2.2
11-60	5.28 ± 1.16	259 ± 57

E. **Low-Mass Drell-Yan Events**

The Drell-Yan (γ) Monte Carlo events are generated with $5 \leq q_{\rm T} \leq 500$ GeV in the same manner as in the Z^0 Monte Carlo events [62]. The CDF published measurement of the cross-section for low-mass DY process has been confirmed by a preliminary analysis using data from Run IB [80, 46]. The combined results for ee and $\mu\mu$ channels are summarized in Table LVI.

The cross-section for $11 \leq M_{\gamma,Z^0} \leq 60$ GeV/c^2 and $\mid y_{\gamma,Z^0} \mid \leq 1$ is 259 ± 57 pb. It should be noted that the measured values include contributions from both photon and Z^0 exchange diagrams, but the expected contribution from Z^0 is $\simeq 1$ pb.

The ISAJET Monte Carlo Drell-Yan samples where $\gamma^* \rightarrow \ell^+\ell^-$ are generated. Dilepton modes from ISAJET processes are selected using the routine **genpfl.cdf** in the $EXOTIC_UTILITIES/ area to filter dilepton events where at least one high $p_{\rm T}$ lepton ($p_{\rm T} \geq 8.0$ GeV/c) or two low $p_{\rm T}$ leptons ($p_{\rm T} \geq 2.8$ GeV/c). The cross-section is presented along with the fraction of dilepton filtered events as well as the scaling factors for three parton density functions in Table LVII.

TABLE LVII. ISAJET Monte Carlo cross-section and correction factors for Drell-Yan ($\gamma \to \ell^+\ell^-$).

PDF	ISAJET $\sigma(\gamma)$ (pb)	ϵ_{GENPLF}	$\sigma^{\gamma}_{effective}$ (pb)	Correction Factor
MRSD0′	796.4	0.1475 ± 0.0035	118	2.19 ± 0.48
GRVLO	981.3	0.1269 ± 0.0033	125	2.07 ± 0.46
CTEQ2L	830.1	0.1451 ± 0.0039	120	2.16 ± 0.48

TABLE LVIII. ISAJET Monte Carlo cross-sections and scaling factors for $t\bar{t}$.

PDF	σ (pb)	Correction
MRSD0′	4.361	1.74 ± 0.41
GRVLO	4.415	1.72 ± 0.41
CTEQ2L	4.515	1.68 ± 0.40

F. **Top Quark Production**

The $t\bar{t}$ Monte Carlo events are generated with $0.1 \leq q_{\rm T} \leq 500$ GeV [62]. With the same parameter, the Monte Carlo cross-sections with MRSD0′, CTEQ2L, and GRVLO are averaged to be 4.4 pb. The ISAJET cross-section is compared to the CDF measurement of 7.6 ± 1.8 pb [81]. The resultant scaling factors are listed in Table LVIII.

G. **Diboson Production**

The diboson events are generated with $0.1 \leq q_{\rm T} \leq 500$ GeV [62]. The ISAJET cross-sections are compared to the NLO calculation of $W^+W^-/W^{\pm}Z^0/Z^0Z^0$ production cross-sections for various parton distribution functions (HMRS B, HMRS E, DFLM 160, DFLM 260, and DFLM 360)[82, 83, 84]. The resultant scaling factors are summarized in Table LIX. The scaling factor for HMRS B will be used with regards to SUSY analyses, but the results with other parton density functions are shown for

TABLE LIX. ISAJET Monte Carlo cross-sections and scaling factors for diboson production.

Diboson Mode	PDF	σ_{ISAJET} (pb)	σ_{NLO} (pb)	Correction
	HMRS B	6.603	9.53	1.44
	HMRS E	6.929	9.90	1.43
W^+W^-	DFLM 160	6.335	9.64	1.52
	DFLM 260	5.968	9.17	1.54
	DFLM 360	5.543	8.73	1.57
	HMRS B	0.4552	1.33	2.92
	HMRS E	0.4975	1.42	2.85
W^+Z^0	DFLM 160	0.4349	1.29	2.97
	DFLM 260	0.4074	1.21	2.97
	DFLM 360	0.3754	1.14	3.04
Z^0Z^0	HMRS B	0.7430	1.08	1.45

comparison.

H. **Bottom and Charm Production**

The Monte Carlo dilepton events from $b\bar{b}/c\bar{c}$ production are generated with MRSD0′, GRVLO, and CTEQ2L [62]. Three different production mechanisms are considered: (1) direct production, (2) initial state gluon splitting, and (3) final state gluon splitting. A factor of 2 is used for the initial state gluon splitting Monte Carlo samples to incorporate $p\bar{p} \to b + g$ as well as $p\bar{p} \to g + b$. Unfortunately, no $B^0\bar{B}^0$ mixing is included. Therefore, the numbers of opposite sign (OS) and like sign (LS) dilepton events in ISAJET, OS_{ISAJET} and LS_{ISAJET}, have to be corrected to reflect an effect due to the mixing in a comparison with the data.

The proper number of OS and LS events with $B^0\bar{B}^0$ mixing are given in

Eq. E.1 [69]:

$$\left.\begin{aligned} N_{OS} &= ((1-\chi)^2+\chi^2)OS_{ISAJET} + 2\chi(1-\chi)LS_{ISAJET} \\ N_{LS} &= 2\chi(1-\chi)OS_{ISAJET} + ((1-\chi)^2+\chi^2)LS_{ISAJET} \end{aligned}\right\} \quad \text{(E.1)}$$

where χ is the averaged mixing parameter. With a CDF measurement of $\chi = 0.118 \pm 0.008 \pm 0.020$ [69], the following is obtained:

$$\left.\begin{aligned} N_{OS} &= (0.792 \pm 0.044)OS_{ISAJET} + (0.208 \pm 0.044)LS_{ISAJET} \\ N_{LS} &= (0.208 \pm 0.044)OS_{ISAJET} + (0.792 \pm 0.044)LS_{ISAJET} \end{aligned}\right\} \quad \text{(E.2)}$$

In order to study $b\bar{b}/c\bar{c}$ production, $e\mu$ events which should receive little contribution from any other Standard Model process are analyzed. In data, a total of 1,454 $e\mu$ (924 OS and 530 LS) events are skimmed from the Run IB SUSY dilepton sample (457,478 events). Those events satisfy the lepton identification in Table L and trigger selection in Table LII. A cut of $M_{e\mu} > 12$ GeV/c^2 is imposed as in the SUSY dilepton analysis. It should be noted that no isolation cuts are applied for this sample. Monte Carlo samples with MRSD0$'$ are analyzed in the same manner as in the above data analysis.

The number of OS and LS $e\mu$ events expected from non-$b\bar{b}/c\bar{c}$ Standard Model processes are summarized in Table LX. The sum of those contributions seems to be less than 5% of the data sample of 1454 $e\mu$ events. The number of OS and LS $e\mu$ events expected from $b\bar{b}/c\bar{c}$ production are summarized in Tables LXI (without $B^0\bar{B}^0$ mixing) and LXII (with $B^0\bar{B}^0$ mixing in Eq. E.2).

The total systematic uncertainty in the $b\bar{b}/c\bar{c}$ study include uncertainties from the following components: (1) the mixing parameter, (2) identification and trigger efficiencies, (3) luminosity, and (4) choice of the parton density functions (PDFs). The uncertainty on the number of OS and LS dileptons due to the uncertainty on the

TABLE LX. Number of OS and LS $e\mu$ events from ISAJET Z^0, γ, $t\bar{t}$, and $W^+W^-/W^\pm Z^0/Z^0Z^0$ production with MRSD0′. The numbers are normalized to the Run IB luminosity. All scaling factors discussed in previous sections are applied. Only statistical uncertainty is shown.

Physics Process	N_{OS}	N_{LS}	N_{OS+LS}
Z^0	32.0 ± 2.4	2.10 ± 0.60	34.1 ± 2.4
γ	12.0 ± 2.2	1.60 ± 0.86	13.6 ± 2.3
$t\bar{t}$	2.5 ± 0.2	0.70 ± 0.10	3.2 ± 0.2
W^+W^-	1.8 ± 0.2	0.03 ± 0.03	1.8 ± 0.2
$W^\pm Z^0$	0.1 ± 0.1	0.20 ± 0.08	0.3 ± 0.1
Z^0Z^0	0.1 ± 0.1	0.03 ± 0.03	0.1 ± 0.1
Total	48.5 ± 3.2	4.66 ± 1.06	53.1 ± 3.3

TABLE LXI. Number of OS and LS $e\mu$ events from ISAJET $b\bar{b}/c\bar{c}$ production with MRSD0′ before taking into account the $B^0\bar{B}^0$ mixing. The numbers are normalized to the Run IB luminosity. Only statistical uncertainty is shown.

Physics Process	OS_{ISAJET}	LS_{ISAJET}	$OS_{ISAJET} + LS_{ISAJET}$
direct	783 ± 21	124 ± 8	907 ± 23
initial state gluon splitting	132 ± 9	33 ± 4	165 ± 10
final state gluon splitting	212 ± 9	37 ± 3	249 ± 10
$b\bar{b}/c\bar{c}$	1127 ± 25	194 ± 9	1321 ± 26

TABLE LXII. Number of OS and LS $e\mu$ events from ISAJET $b\bar{b}/c\bar{c}$ production using MRSD0′ after taking into account $B^0\bar{B}^0$ mixing. The numbers are normalized to the Run IB luminosity. Only statistical uncertainty is shown.

Physics Process	N_{OS}	N_{LS}
direct	646 ± 43	261 ± 15
initial state gluon splitting	112 ± 12	53 ± 22
final state gluon splitting	176 ± 14	73 ± 34
$b\bar{b}/c\bar{c}$	934 ± 47	387 ± 43

averaged mixing parameter is determined by varying the averaged mixing parameter by one standard deviation. The uncertainties due to the identification, trigger, and luminosity issues associated with a Run IB $e\mu$ analysis have been studied in Ref. [75]. The systematic uncertainty due to PDFs is estimated to be 5%. The systematic uncertainties for χ is $\simeq$ 11%. Uncertainties on lepton identification and trigger efficiencies $\simeq$ 10%. The systematic uncertainty at this time for luminosity was 7%. Thus, a total systematic uncertainty of 17% is determined for the production of $b\bar{b}/c\bar{c}$ events.

The systematic uncertainty for non-$b\bar{b}/c\bar{c}$ Standard Model processes is the same as the above with the exception, of course, due to the $B^0\bar{B}^0$ mixing parameter. This yields a systematic error of 13%.

The contributions from data are tabulated and compared with the number expected from $b\bar{b}/c\bar{c}$ in Table LXIII in both OS and LS events. The large discrepancy between Monte Carlo and data seen in N_{LS} could be due to fakes since effects due to misidentified leptons have not been taken into account in this analysis. By examining the distribution of the opening angle between the leptons in Fig. 57, one sees that a discrepancy lies in the like sign sample where $\Delta\phi(e,\mu) \geq 120^{\circ}$. This observation is consistent with an electron or muon being back-to-back with a jet that has faked a lepton. The excess in N_{LS} for data above Monte Carlo is 138 events. We also expect to see an excess of 138 events in the opposite sign $e\mu$ sample, but it is dominated by real physics events. Assuming that the excess in the like sign events is due to fakes alone, one can estimate that this has a 19% effect on the acceptance. Therefore, the normalization is said to be unity within 26%.

Lastly, distributions of the opening angle between e and μ, dilepton mass, jet multiplicity, and $\not\!\!E_{\rm T}$ for data and Monte Carlo samples are shown in Figs. 57, 58, 59, and 60. The same disagreement using a jet cone size of 0.7 is observed for $b\bar{b}/c\bar{c}$ as

TABLE LXIII. Summary of number of OS and LS $e\mu$ events from various SM processes with MRSD0′. The uncertainty in $N_{OS,LS}$ for Monte Carlo events includes statistical and systematic errors.

Physics Process	N_{OS}	N_{LS}
$b\bar{b}/c\bar{c}$ (see Table LXII)	934 ± 162	387 ± 69
Sum of All		
Non-$b\bar{b}/c\bar{c}$ (see Table LX)	48.5 ± 6.8	4.7 ± 1.2
Backgrounds		
All physics processes	982.5 ± 162	391.7 ± 69
Data	924 ± 30	530 ± 23

seen in the Z^0 analysis.

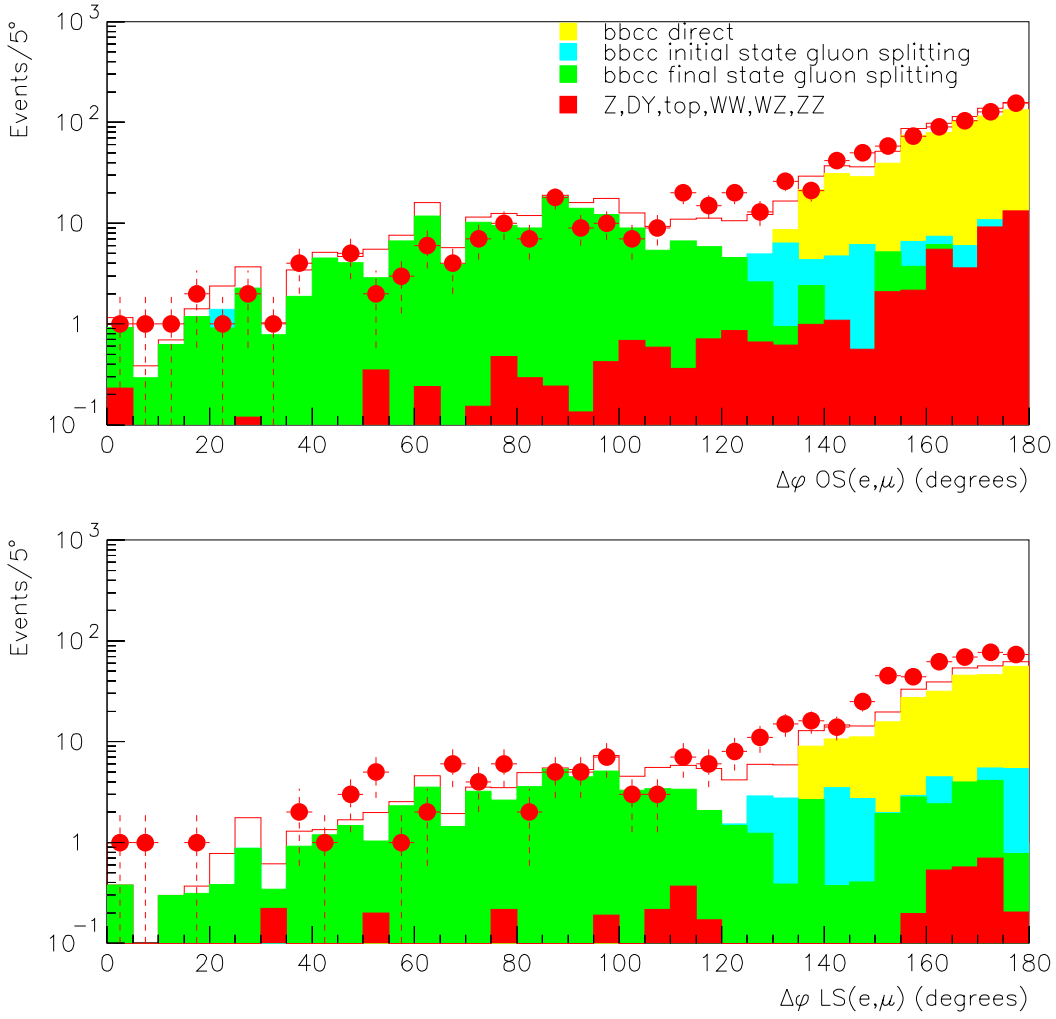

FIG. 57. The opening angle (in degrees) between the electron and muon for opposite and like sign. Here, contributions to the opening angle distribution due to direct production, initial state gluon splitting, and final state gluon splitting are shown. The unshaded histogram represents the sum of all standard model processes using ISAJET+QFL′ MRSD0′ Monte Carlo; the points represent data. Note there is a dilepton mass cut, $M(e\mu) \geq 12$ GeV/c^2, applied to the data and Monte Carlo.

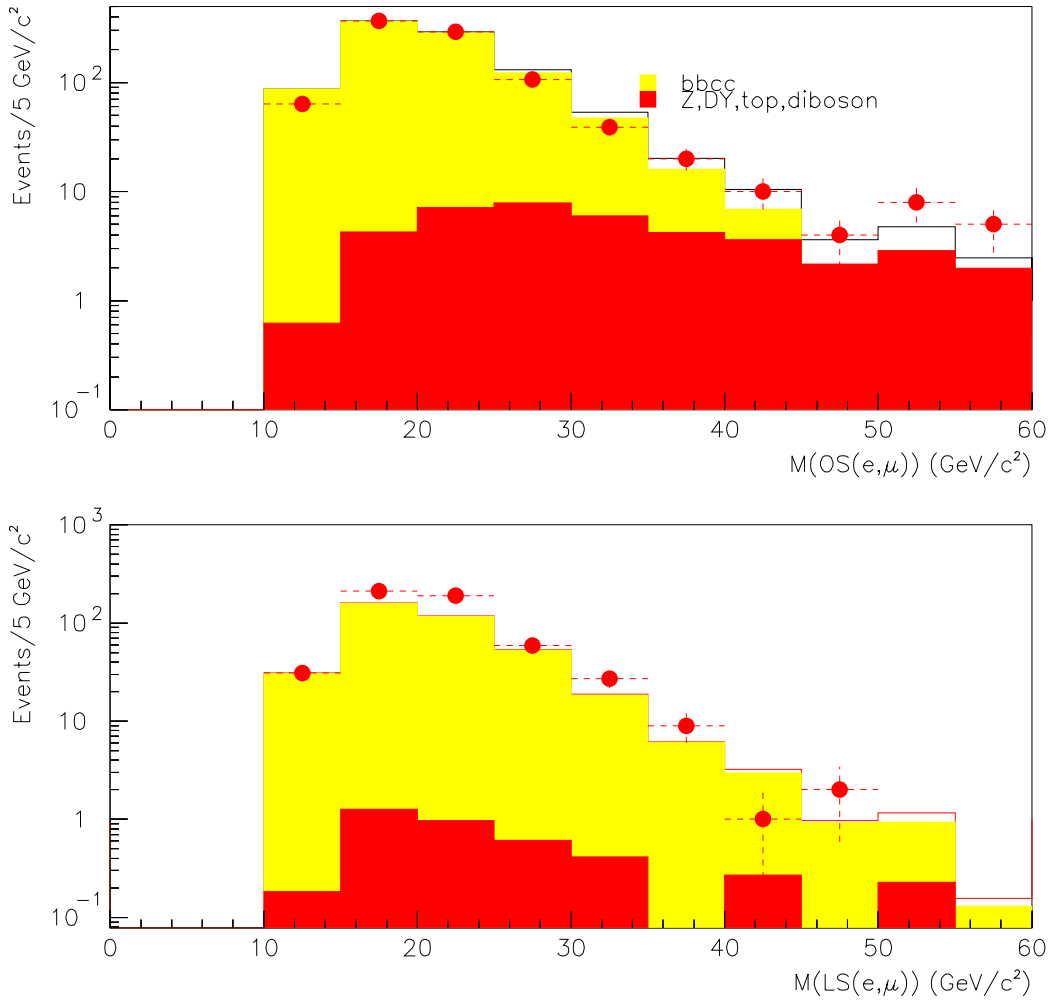

FIG. 58. The dilepton mass of the electron and muon for opposite and like sign. The unshaded histogram represents the sum of all Standard Model processes using ISAJET+QFL′ MRSD0′ Monte Carlo; the points represent data.

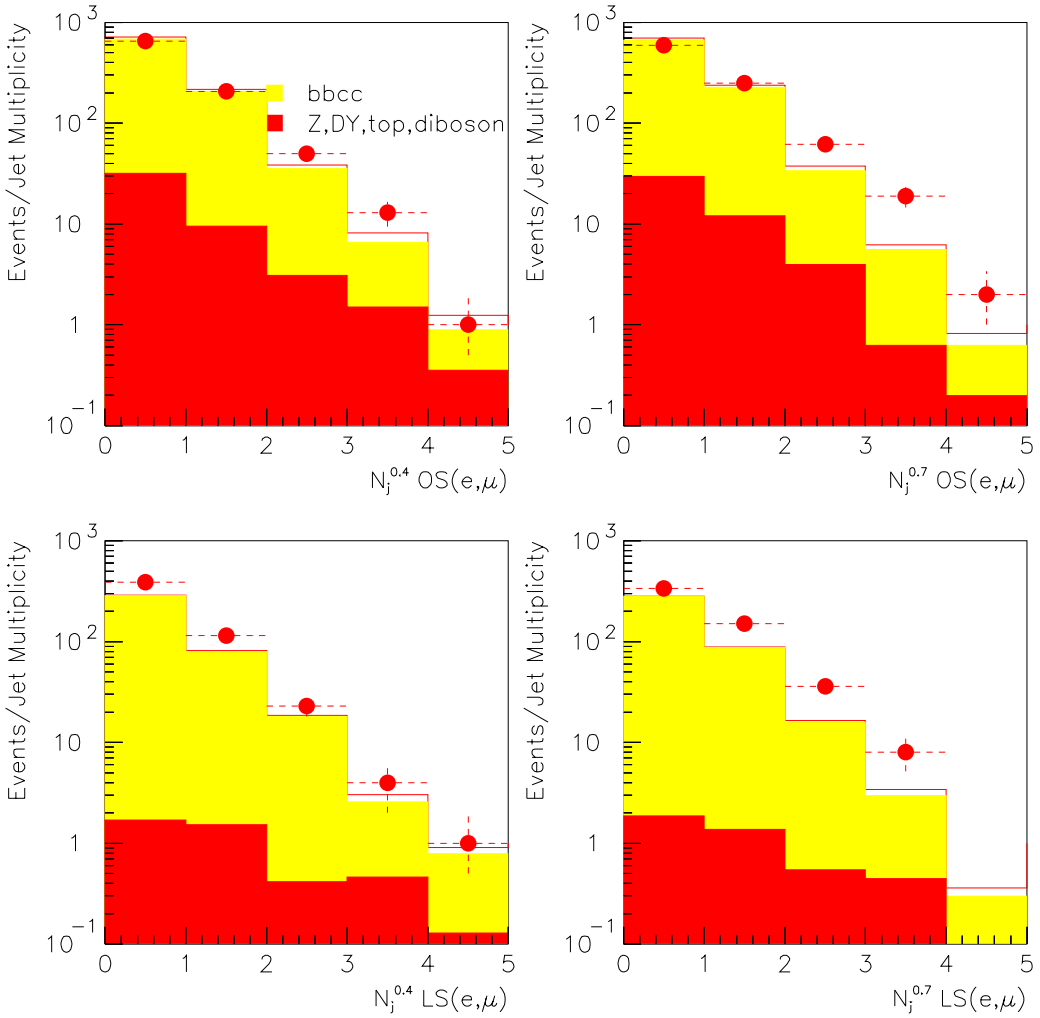

FIG. 59. The jet multiplicity in the electron and muon samples for opposite and like sign and also for both cone sizes, 0.4 and 0.7. The unshaded histogram represents the sum of all Standard Model processes using ISAJET+QFL′ MRSD0′ Monte Carlo; the points represent data.

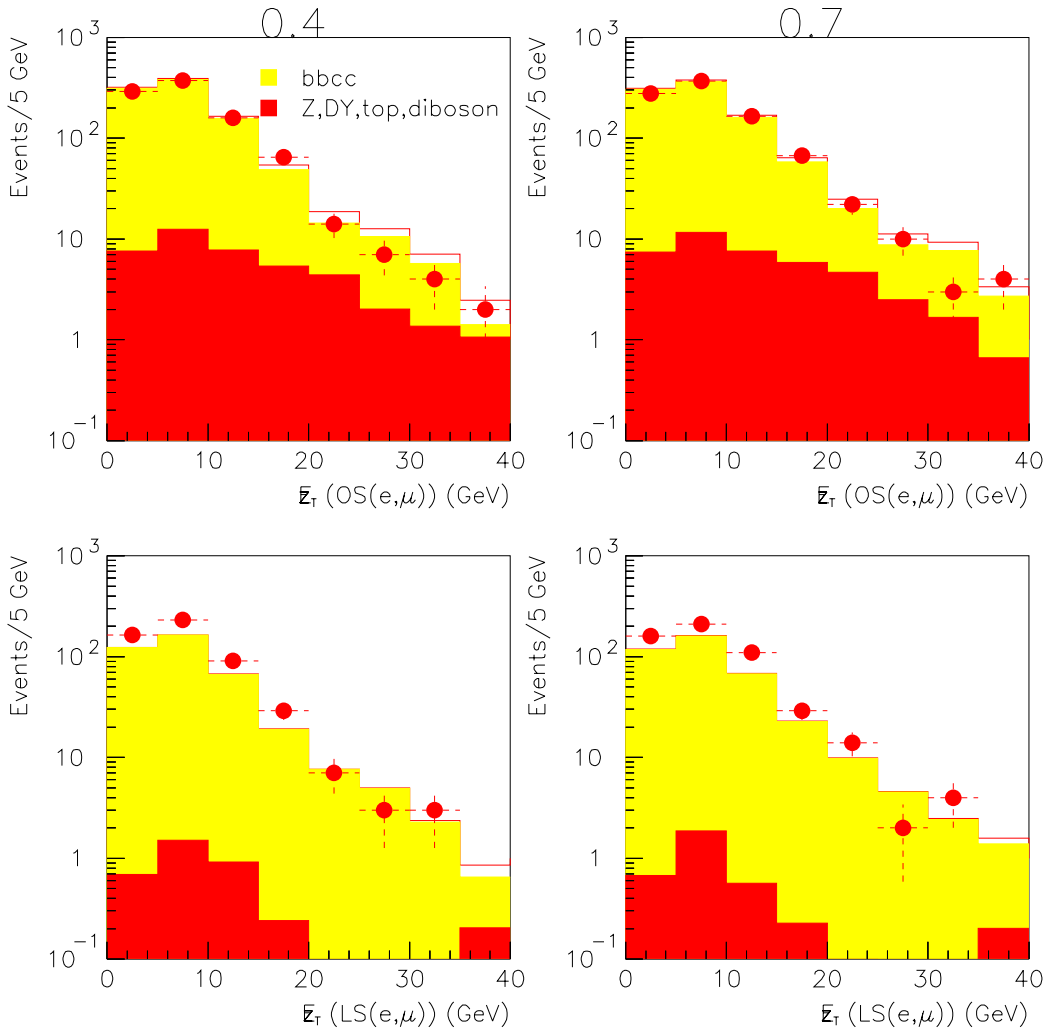

FIG. 60. The $\not\!\!E_{\rm T}$ in the electron and muon samples for opposite and like sign and also for both jet cone sizes, 0.4 and 0.7. The unshaded histogram represents the sum of all Standard Model processes using ISAJET+QFL′ MRSD0′ Monte Carlo; the points represent data.

APPENDIX F

LIMIT CALCULATION

The frequentist method is used by CDF in order to determine upper limits on Poisson processes in the presence of uncertainties (both statistical and systematic) simultaneously in signal and background combining the approaches in Ref. [85]. The probability of observing the number of events seen, n_0, depends on μ, the mean number of events expected using Poisson statistics :

$$P(n_0;\mu) \;=\; \tfrac{\mu^{n_0}\, e^{-\mu}}{n_0!}. \tag{F.1}$$

In particle searches, the value of μ must be determined. The upper limit N on the number of expected events as that value of μ for which there is some probability ϵ to observe n_0 or fewer events. The confidence level (CL) of the upper limit is then $1-\epsilon$. One then calculates ϵ by summing over all probabilities :

$$\epsilon \;=\; \textstyle\sum_{n=0}^{n_0} P(n;\mu) \tag{F.2}$$

After varying μ until ϵ corresponds to the desired confidence level, the value of μ is then equal to the upper limit, N.

After determining the background μ_B to within (statistical plus systematic) Gaussian uncertainty of σ_B, and the overall acceptance for signal A within uncertainty σ_A. The relative uncertainty on μ_S is σ_A/A. The Poisson upper limit N on μ_S as the value of μ_S for which there would be more than n_0 events and have $n_B \leq n_0$. The value N is determined from ϵ from the following equation :

$$\epsilon \;=\; \frac{\sum_{n=0}^{n_0}\int_0^\infty\int_0^\infty \frac{1}{\sqrt{2\pi\sigma_N^2}} P(n;\mu'_B+\mu'_S)\, e^{-\frac{(\mu_B-\mu'_B)^2}{2\sigma_B^2}}\, e^{-\frac{(N-\mu'_S)^2}{2\sigma_N^2}}\, d\mu'_B\, d\mu'_S}{\sum_{n=0}^{n_0}\int_0^\infty P(n;\mu_B)\, e^{-\frac{(\mu_B-\mu'_B)^2}{2\sigma_B^2}}\, d\mu'_B} \tag{F.3}$$

where $\sigma_N = N\sigma_A/A$ assuming that the true values of μ_S and μ_B are distributed in Gaussians about some means with the widths being the uncertainties.

The Exotic Group at CDF uses a routine called **poilim.f** to evaluate Eq. F.3 and determine the confidence level and thereby calculating N[86]. Hence, one can calculate the limit at the 95% C.L.

VITA

James Paul Done [redacted] entered Roosevelt University on a four year scholarship in September 1985. He pursued Mathematics as a major and Physics as a minor. He had been awarded a Science and Engineering Research Semester (SERS) grant by the United States Department of Energy (U.S. DOE) to complete a senior thesis at Argonne National Laboratory (Argonne, Illinois) from January 1988 until September 1988. He received his B. S. in Mathematics from Roosevelt University in September 1988. He began his studies at the University of California, Davis on a Mellon Fellowship where he devoted his time to the study of computational physics. He finished his M. S. in Engineering-Applied Science in September 1990. He then thought that he should turn his attention towards complex computational problems and chose to go to Texas A&M University to investigate the field of High Energy Physics and its pursuit of the understanding of the Creation of the Universe. He can be reached by mail at Fermi National Accelerator Laboratory, CDF MS 318 P.O. Box 500 Batavia, IL 60510-0500.